Charles University in Prague
Faculty of Mathematics and Physics

MASTER THESIS

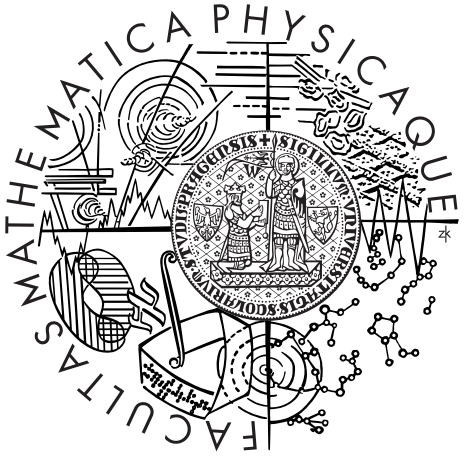

Leoš Pohl

Heat diffusion equation and thermophysical modelling of asteroids

Astronomical Institute of Charles University

Supervisor of the master thesis: Mgr. Josef Ďurech, Ph.D.
Study programme: Physics
Specialization: Theoretical physics

Prague 2014

Acknowledgements

I would like to express my sincere gratitude to my supervisor Mgr. Josef Ďurech, Ph.D. for his friendly approach, for the time he spent discussing the topics and for valuable insights.

I declare that I carried out this master thesis independently, and only with the cited sources, literature and other professional sources.

I understand that my work relates to the rights and obligations under the Act No. 121/2000 Coll., the Copyright Act, as amended, in particular the fact that the Charles University in Prague has the right to conclude a license agreement on the use of this work as a school work pursuant to Section 60 paragraph 1 of the Copyright Act.

In ..... date ..... signature of the author

Název práce: Rovnice vedení tepla a termofyzikální modelování planetek

Autor: Leoš Pohl

Katedra: Astronomický ústav UK

Vedoucí diplomové práce: Mgr. Josef Ďurech, Ph.D., Astronomický ústav UK

Abstrakt: Inverze světelných křivek asteroidů je standardní metodou jak jejich určit tvary, rotační periody a orientace rotačních os. Tuto metodu je možné rozšířit zahrnutím dat z infračervené oblasti, tak aby bylo možné určit velikost, albedo, tepelnou setrvačnost a hrubost povrchu asteroidu. K modelování infračerveného toku je třeba vyřešit rovnici vedení tepla (RVT). Zabýváme přesností numerického řešení RVT potřebnou pro řešení tohoto rozšířeného inverzního problému. V práci ukážeme, že současná implementace numerického řešení RVT vede k podstatným chybám v infračerveném toku. Uvádíme doporučení jak upravit řešení RVT, aby se tyto chyby zmenšily. Diskutujeme stabilitu a jednoznačnost řešení provedeného touto rozšířenou metodou a přesnost a stabilitu určení fyzikálních parametrů. Na základě řešení rozšířeného problému vygenerujeme tvary vybraných asteroidů a určíme jejich fyzikální parametry.

Klíčová slova: asteroidy, planetky, rovnice vedení tepla, inverze světelných křivek

Title: Heat diffusion equation and thermophysical modelling of asteroids

Author: Leoš Pohl

Department: Astronomical Institute of Charles University

Supervisor: Mgr. Josef Ďurech, Ph.D., Astronomical Institute of Charles University

Abstract: Light curve inversion is a standard method to determine shapes, rotation periods and spin axis orientations of asteroids. This method can be extended to determine the size, albedo, thermal inertia and surface roughness parameters of an asteroid by including observations in thermal infrared. A solution of the Heat Conduction Equation (HCE) is necessary to model infrared flux from the asteroid. We analyse the accuracy requirements of the extended method for numerical solution of the HCE. We show that current implementation leads to errors in flux that are substantial. We recommend changes in the current implementation of the HCE solving approach to address the accuracy issues. We discuss uniqueness and stability of the solutions produced by the extended method as well as the accuracy of the determined parameters and their stability. Shapes of asteroids are produced and their physical attributes are determined based on light curve and infrared data.

Keywords: asteroids, small bodies of the Solar System, Heat Conduction Equation, Light curve inversion

Contents

Preface

Asteroids along with other minor bodies (Kuiper Belt Objects, comets and planetary satellites) of our Solar System are the leftover material from the planet formation process. Many of them have undergone few processes since compared e.g. to the material that makes up the Earth. Therefore, they provide valuable clues to the early history of the Solar System. From this point of view, we are especially interested in the bodies that were created by accretion of dust particles and grains of material and that did not undergo melting nor any other process involved in planet formation. Consequently, understanding the processes that led to the creation of asteroids unravel important information about the evolution of the Solar System.

Furthermore, asteroids are also the most probable source of water on the Earth (Morbidelli et al., 2000) and during the whole history of the Solar System they have constantly shaped the surface of the planets as well as modified the Earth's biosphere by impacts. Due to these roles in the evolution of the Solar System, asteroids have become important objects to study. However, despite numerous discoveries of asteroids in the Solar System so far, the knowledge about their physical properties is incomplete at best.

Physical properties of some asteroids can be inferred from measurements of meteorites[1]. But, this presents only a fraction of information we would like to know. Thus, we need methods based on observational data to evaluate the physical parameters. Density is one of the most basic properties that we are interested in. However, measuring even such a basic quantity proves quite difficult. If we found a large asteroid with a satellite, the density would be easy to measure (like in the case of a dwarf planet 2002 UX25 in the Kuiper belt, see Fig. 1).

Unfortunately, asteroids are mostly observed as dots without any further details about their shape. These "dots" leave us only little information that we can measure — the quantity of light reflected from the surface of the asteroid (i.e. the *apparent magnitude*[2] of the asteroid) and its variation in time; the time variation of electromagnetic flux in the *infrared range*, i.e. how much infrared flux comes from the asteroid at different wavelengths at various time instants; and the position of the asteroid. Additionally, thanks to *space missions*, we also have some first-hand data from the asteroids. These data provide essential test of models that aim to determine physical properties of asteroids from the available measurements.

[1]Meteorites are the remnants of asteroids that survive entry through the Earth's atmosphere and impact the surface. Most meteorites come from the asteroids that have not undergone melting and planetary differentiation, we call them *chondrites*. Unfortunately, these chondrites provide limited information. During atmospheric entry, most of the material is evaporated; also they are but a fraction of their parent body. That been said, chondrites constitute of round grains that formed from melted drops that accreted to the surface of the asteroid. We call these round grains *chondrules*; they are believed to be among the oldest materials in our Solar System.

[2]For a detailed treatment of various radiometric and photometric quantities, see Brož, Šolc 2012.

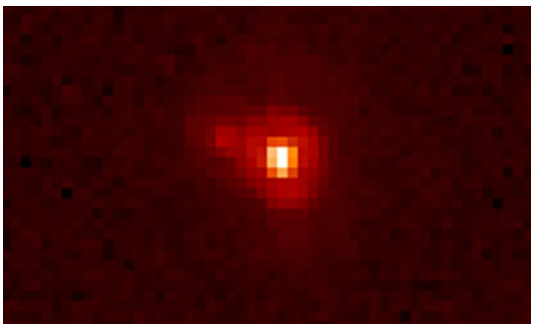

Source: Mike Brown/HST

Figure 1: 2002 UX25 and its satellite as seen by the Hubble Space Telescope.

Space missions to asteroids

The first images were of asteroids 951 Gaspra and 243 Ida and came from the Galileo spacecraft (1991 and 1993).

The NEAR Shoemaker space probe followed shortly. It photographed the asteroid 253 Mathilde during a 1200 km flyby (its about 500 images covered approximately 60% of the asteroid's surface (APL, 1997)) and then headed towards 433 Eros. In 2001, after orbiting 433 Eros for a year, the operation control decided to execute descent and the spacecraft successfully touched down. Both Galileo and NEAR Shoemaker spacecraft come were launched by the The National Aeronautics and Space Administration (NASA).

The first samples of asteroid material were provided by the Hayabusa spacecraft (launched by Japan Aerospace Exploration Agency (JAXA)) which landed on asteroid 25143 Itokawa in 2005 to collect samples of asteroid material and returned them to the Earth in 2010.

The Rosetta spacecraft launched by the European Space Agency (ESA) provided valuable data on the 2867 Šteins asteroid during its 800 km flyby in 2008 and on the asteroid 21 Lutetia two years later, passing Lutetia within approximately 3000 km.

The NASA's Dawn space probe is currently on its way to 1 Ceres, the largest object in the main asteroid belt, after spending over a year in the orbit around 4 Vesta.

Although these missions provided data only about a handful of asteroids, the data are essential to further our knowledge of asteroids; they also provide a good test for our numerical models based on observations. On the other hand, ground-based studies are of significant importance for the planning of space missions and choosing their potential target. In Fig. 2 we present a series of images of asteroids provided by the aforementioned spacecrafts in order to illustrate various shapes and surface characteristics of asteroids.

Observations

In this work we are concerned with a technique that enables us to create physical models of asteroids based on observation data. These data come from two main sources — telescope observations in visible light and measurements of infrared flux from the asteroid.

In the first chapter we provide a brief introduction to this modeling technique along with its numerical implementation. We then follow with discussion of numerical solution of the Heat Conduction Equation which is necessary for our approach to the physical modeling and evaluate the current approach to its solution along with its implications on the results of the modeling technique.

(a) 951 Gaspra by Galileo

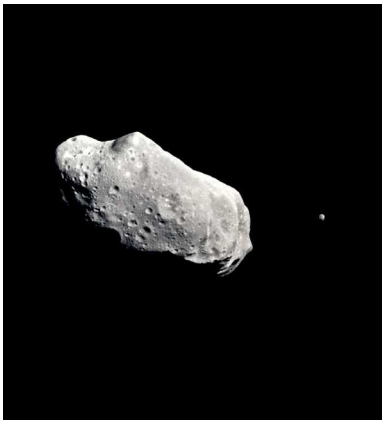

(b) 243 Ida and its moon by Galileo

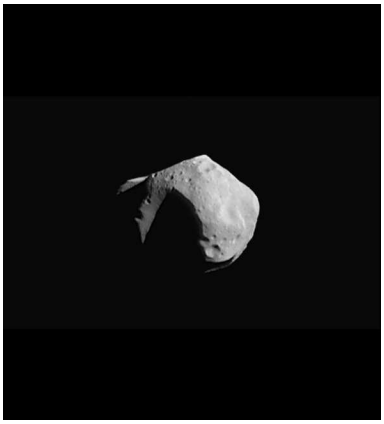

(c) 253 Mathilde by NEAR

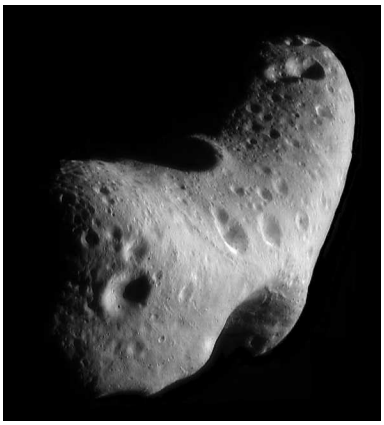

(d) 433 Eros by NEAR

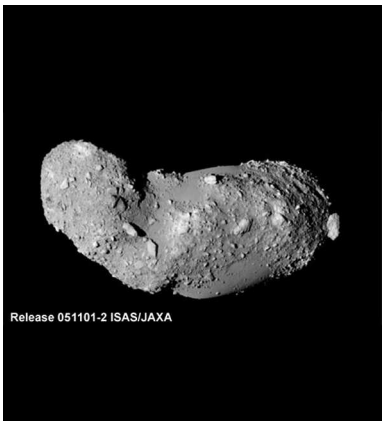

(e) 25143 Itokawa by Hayabusa

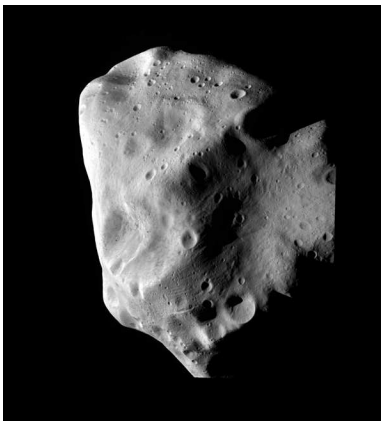

(f) 21 Lutetia by Rosetta

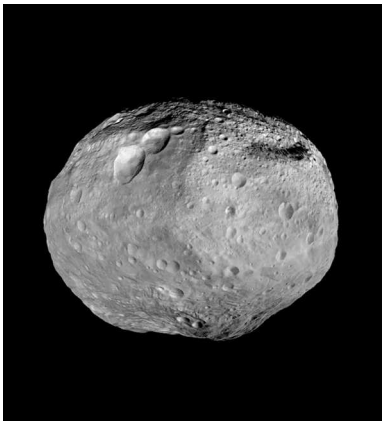

(g) 4 Vesta by Dawn

Source: NASA: (a)-(d) and (g); JAXA: (e), ESA: (f).

Figure 2: Images of asteroids from spacecraft missions.

In the third and fourth chapters, we analyze the properties of the modeling technique, specifically the uniqueness and stability of its results and create models of selected asteroids based on real observation data.

Chapter 1

Introduction

1.1 The apparent magnitude

By far the most important source of information about asteroids is the light reflected from their surface and detected by ground and space based telescopes. As the asteroid rotates, it scatters the light from the Sun incident on its surface. The "amount of light" that is scattered depends on the shape of the asteroid, its surface properties and irregularities, the observer's position, the asteroid's rotation phase etc. These determine how much light is scattered into various directions at various time instants as a function of incident light and its direction. Therefore, if we are viewing the asteroid from the Earth, we can see a dimming and brightening point. This is illustrated in Fig. 1.1 which suggests how shape and surface irregularities can determine the amount of light reflected by the asteroid. A plot that depicts varying amount of light in the form of apparent magnitude from a given asteroid (or any celestial body in general) in time is called a *light curve*. We present a light curve of asteroid 306 Unitas in Fig. 1.2.

We can formalize the above discussion by introducing a function f which calculates flux of photons Φ_i (see the following paragraph for the relation between the apparent magnitude and flux) from the asteroid registered by our measuring apparatus during time instant $t_i + \Delta t$:

$$\Phi_i = f(\vec{\Sigma}, \vec{\Pi}, \vec{\Xi}, \vec{\Upsilon}, t_i),$$

where $\vec{\Sigma}$ contains all parameters related to asteroid's spin-orbital configuration (e.g. orientation of asteroid's axis with respect to the ecliptic plane, rotational period etc.), $\vec{\Pi}$ contains all parameters necessary to fully describe the relative positions of the asteroid, the sun and the observer, $\vec{\Xi}$ contains all parameters that describe the asteroid's shape and size, $\vec{\Upsilon}$ contains all parameters necessary to completely describe reflection of light

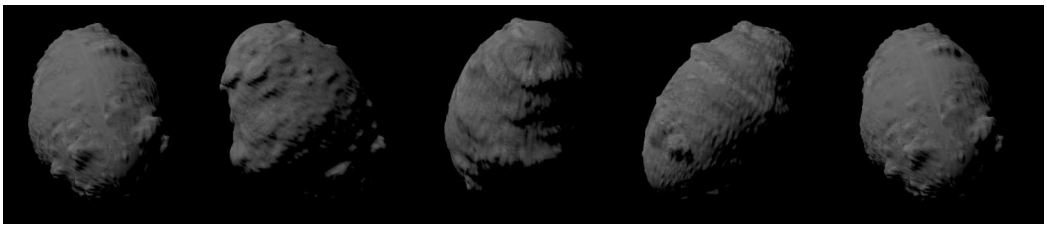

Source: Author.

Figure 1.1: Illustration of dimming and lightening of an asteroid due to its shape and rotation phase angle.

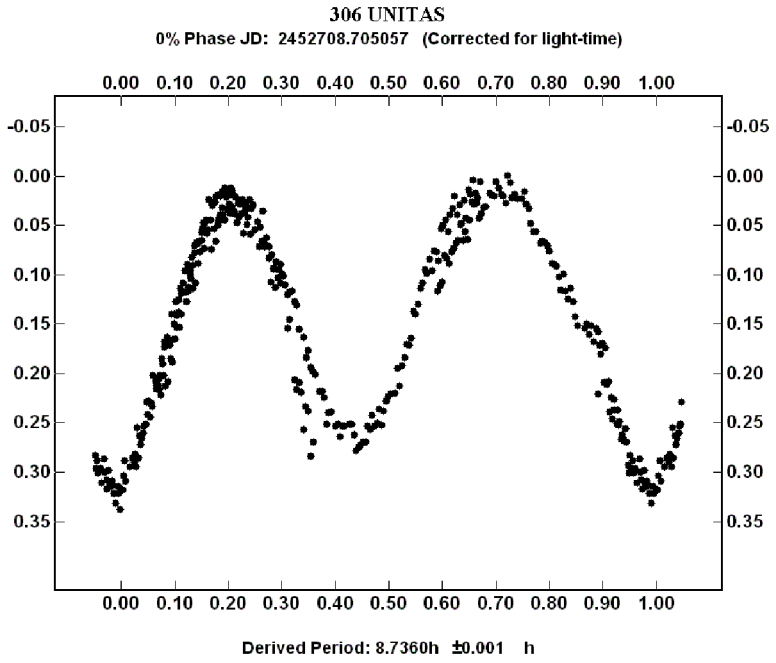

Source: Antelope Hills Observatory.

Figure 1.2: Light curve for asteroid 306 Unitas.

from the asteroid's surface and t_i is the time when the measurement of Φ_i took place. Calculating the flux Φ is relatively easy once we know the function f and all the necessary parameters. This is called a *direct problem*.

However, Φ is a quantity that we can measure directly. We are usually more interested in finding the parameters $\vec{\Sigma}$, $\vec{\Pi}$, $\vec{\Xi}$, $\vec{\Upsilon}$. Some of those parameters, like relative positions of of the observer, the Sun and the asteroid ($\vec{\Pi}$), are known to us; others, like the asteroid's shape and size ($\vec{\Xi}$), are unknown. In general, the problem of determining the set of parameters $\vec{\Sigma}$, $\vec{\Xi}$, $\vec{\Upsilon}$ of the function f, provided we know the values Φ_i in various time instants t_i is called an *inverse problem*. We say that these unknown parameters form a *parameter space*.

Apparent magnitude, flux, other quantities... We take a short detour to systematize the various quantities that we have already used. We can imagine the light scattered from a surface as a large number of photons flying in all directions. As each photon carries energy, the measured quantities will be based on energy. If we put a CCD detector in the path of photons, we can measure flux, i.e. $\mathrm{J} \cdot \mathrm{m}^{-2} \cdot \mathrm{s}^{-1}$. However, in radiometry, different quantities are used.

The most basic quantity is called *radiance* denoted I with units $\mathrm{W} \cdot \mathrm{m}^{-2} \cdot \mathrm{sr}^{-1}$. Radiance is a measure of energy which is emitted by a unit surface area during a unit time interval and falls within a unit solid angle in a specified direction.

Another quantity that is used in radiometry is *irradiance* denoted Φ with units $\mathrm{W} \cdot \mathrm{m}^{-2}$. Irradiance is a measure of energy emitted from a unit surface area into all directions. It is therefore an integral over solid angle (in our case hemisphere as the light is only scattered into half space) of the radiance.

Both these quantities are defined with respect to the source of the energy — we think of them *energy that has left an emitter*; unlike the term *flux* which we usually understand as energy that has reached a detector.

With these two quantities defined, we can now formalize our definition of apparent magnitude. Apparent magnitude of an object m is a function that scales irradiance from the object relative to irradiance from a reference object. So the relation between the above quantities can be depicted:

$$I \to \Phi \leftrightarrow m\,.$$

In measurements, we always measure a flux Φ, i.e. the energy that has reached the detector and we usually report the measurements in magnitudes m.

All of the above quantities have been defined as integral, i.e. over all wavelengths. It is possible to define those quantities also as a function of wavelength (or frequency). We then call these quantities spectral radiance and spectral irradiance. The spectral radiance is governed by the Planck law, see Eq. (1.2) later in the text.

The inverse problem The standard numerical approach to solve the inverse problem is the Least Squares Method (LSM). If we want to find the solution to the inverse problem for N measurements, we have to find such a set of parameters $\vec{\Sigma}$, $\vec{\Xi}$, $\vec{\Upsilon}$, so that the quantity:

$$\chi^2 = \sum_{i=1}^{N} \left[\frac{\Phi_i - f(\vec{\Sigma}\,, \vec{\Pi}\,, \vec{\Xi}\,, \vec{\Upsilon}, t_i)}{\sigma_i} \right]^2 , \tag{1.1}$$

is minimized for known parameters $\vec{\Pi}$ (the relative positions of the asteroid, Sun and observer). The quantities σ_i in the denominator are measurement errors of the quantity Φ_i. Although it is conceivable that we find a solution to this problem, the question remains whether such a solution is unique and thus whether we have found the proper parameters of the asteroid.

It can be shown (Kaasalainen et al., 1992) that under several assumptions (especially if we know the orbital configuration and relative positions (i.e. $\vec{\Sigma}$ and $\vec{\Phi}$) and if light curves cover sufficiently wide range of observing geometries), the inverse problem has a *unique solution* for *convex* shapes. For *non-convex* shapes, the solution can be found in principle but the mathematical assurance of uniqueness is lost and we are faced with plethora of solutions that correspond to the observed data. We also loose stability of the solution, i.e. a small perturbation in observed data will result in very different asteroid models. Despite the non-convex shape limitation, the *light curve inversion* has become a standard method to derive convex shapes of asteroids.

Scattering model Until now we have talked about the observables Φ and m, we mentioned the meaning of parameters $\vec{\Sigma}$, $\vec{\Pi}$, $\vec{\Xi}$, $\vec{\Upsilon}$. However, we omitted to mention how we obtain the function f, which is needed for both, the direct and the inverse problems. It certainly represents a model of flux from the asteroid. Consequently, this function models the scattering of light incident on the asteroid's surface. The scattering from a small surface element is usually described by radiance of the scattered light I:

$$I(\vec{\gamma_{\text{in}}}, \vec{\gamma_{\text{out}}} \,|\, g) = g(\vec{\gamma_{\text{in}}}, \vec{\gamma_{\text{out}}}) \cdot \Phi_{\text{in}}(\vec{\gamma_{\text{in}}})\,,$$

where g is a function that describes the actual scattering and Φ_{in} is the incident flux on the asteroid's surface and $\vec{\gamma_{\text{in}}}$ and $\vec{\gamma_{\text{out}}}$ determine the direction to the sun and to the observer respectively. The simplest scattering function is a constant:

$$g \equiv g_{\text{L}} = \text{constant}\,.$$

This is the Lambert scattering. Other scattering laws are e.g. Lommel-Seeliger or Hapke model. For detailed treatment we refer to Brož and Šolc (2013). Even though the exact law that would describe scattering properties of asteroids is unknown (Kaasalainen et al., 2001), the aforementioned Hapke model provides a very good approximation.

1.2 The spectrum of light

Another quantity that we can measure is the spectrum of light from the asteroid. We are most interested in the infrared spectrum as it bears information about the surface temperature. In black body approximation we can describe the thermal radiation from an asteroid with Planck's law:

$$F(\lambda, T) = \frac{2hc^2}{\lambda^5} \frac{1}{\mathrm{e}^{\frac{hc}{\lambda k_\mathrm{B} T}} - 1}\,, \tag{1.2}$$

where F denotes spectral radiance, with units $\mathrm{W \cdot m^{-2} \cdot sr^{-1} \cdot m^{-1}}$, which is the same quantity as radiance defined above but only the light at wavelength λ is considered; h is the Planck constant, c the speed of light, k_B is the Boltzmann constant and T is the surface temperature.

A lot of catalogues report the flux in the flux unit (also Jansky unit) Jy which is equivalent to $10^{-26}\,\mathrm{W \cdot m^{-2} \cdot Hz^{-1}}$. And because $F(\lambda, T)\,\mathrm{d}\lambda$ is the irradiance at wavelengths between λ and $\lambda + \mathrm{d}\lambda$ and $-F(\nu, t)\,\mathrm{d}\nu$ is irradiance at frequencies between ν and $\nu - \mathrm{d}\nu$, it follows that $F(\lambda, T)\,\mathrm{d}\lambda = -F(\nu, T)\,\mathrm{d}\nu$. But, $\lambda = \frac{c}{\nu}$ and therefore $\mathrm{d}\lambda = -\frac{\lambda^2}{c}\,\mathrm{d}\nu$ which gives:

$$\begin{aligned}
F(\nu, T)\big|_\mathrm{Jy} &= 10^{26} \times F(\nu, T)\big|_{\frac{\mathrm{W}}{\mathrm{m^2 \cdot Hz}}}\,, \\
F(\lambda, T)\big|_\mathrm{Jy} &= 10^{26} \times \frac{\lambda^2}{c} F(\lambda, t)\big|_{\frac{\mathrm{W}}{\mathrm{m^2 \cdot sr \cdot m}}}\,, \\
&= 10^{26} \times \frac{\lambda|_{\mu\mathrm{m}}{}^2 \times 10^{12}}{c} F(\lambda, t)\big|_{\frac{\mathrm{W}}{\mu\mathrm{m^3 \cdot sr}}} \times 10^{-18}\,, \\
&= 10^{20} \times \frac{1}{c} \left[\lambda^2 \cdot F(\lambda, t)\right]\Big|_{\frac{\mathrm{W}}{\mu\mathrm{m \cdot sr}}}\,.
\end{aligned} \tag{1.3}$$

The extension of the inversion method The standard light curve inversion method assumes that we know orbital geometry, scattering parameters (i.e. the scattering law and its parameters) and surface properties (i.e. parameters that characterize its roughness, its reflectivity — albedo. In turn we can determine a convex shape of the asteroid and its spin configuration, i.e. the rotational period and the orientation of its spin axis (Kaasalainen et al., 2001). Because all of these parameters are optimized together, a very interesting question can be raised: whether it would be possible to extend the standard inversion method by supplementing the light curve data with infrared observations and also by including further physical parameters (e.g. *thermal parameters*) in the *parameter space*.

A new numerical technique has been implemented with the above motivation; we call this new technique that solves the extended inversion problem *TPM* which is a abbreviation for *thermo-physical modelling*.

1.3 TPM implementation of the inverse method

The solution technique of the standard light curve inversion problem is to minimize the quantity χ^2 defined in Eq. (1.1). We modify this quantity in the extended inversion

problem in the following way:

$$\chi^2 = \sum_{i=1}^{N_{\mathrm{LC}}} \left[\frac{\Phi_i^{\mathrm{LC}} - f(\vec{\Sigma}, \vec{\Pi}, \vec{\Xi}, \vec{\Upsilon}, t_i)}{\sigma_i^{\mathrm{LC}}} \right]^2 + w^{\mathrm{IR}} \sum_{i=1}^{N_{\mathrm{IR}}} \left[\frac{\Phi_i^{\mathrm{IR}} - \tilde{F}(\vec{\Sigma}, \vec{\Pi}, \vec{\Xi}, \vec{\Upsilon}, t_i)}{\sigma_i^{\mathrm{IR}}} \right]^2 . \quad (1.4)$$

The measurements and their respective errors are described by Φ_i and σ_i with appropriate superscripts — LC for light curve and IR for the infrared measurements.

The parameters $\vec{\Sigma}$, $\vec{\Pi}$, $\vec{\Xi}$, $\vec{\Upsilon}$ describe the orbital configuration, relative positions of the Sun, the Earth and the asteroid, shape and size of the asteroid and scattering from the surface respectively. The parameters in the parameter space of the model are listed in Tab. 1.1.

The function f models the visible light flux and the function $\tilde{F}$ the models infrared flux — i.e. the Planck law integrated over the surface of the asteroid and multiplied by emissivity η.

The infrared contribution to the total χ^2 is controlled by the infrared weight parameter w^{IR}.

Table 1.1: Optimized parameters of the TPM solver.

parameter name	description
areas of facets	
λ	Ecliptic longitude of the asteroid's spin axis.
β	Ecliptic latitude of the asteroid's spin axis.
period	Initial rotational period of the asteroid.
thermal inertia	Thermal inertia is defined as $\Gamma = \sqrt{\rho c \alpha}$, where ρ is the bulk mass density of the material, c is the material's heat capacity and α is the heat conductivity of the material.
infrared emissivity	Constant η that specifies the reflectivity of the asteroid's surface in the infrared spectral range.
crater aperture	Parameters define roughness of the surface, see
crater coverage	Lagerros (1998).
ω, h, S_0, g, θ	Hapke parameters that determine the surface reflectivity with respect to direction.

1.3.1 The TPM solver process

The TPM code uses χ^2 minimization and parameter optimization technique based on Levenberg-Marquardt method — see Press et al. (1992), Chap. 15.5. This subsection gives a very brief overview of this process.

Initialization The initial shape guess is a triaxial ellipsoid that is created from a sphere of *initial size* (see Tab. (1.1)). This ellipsoid is triangulated into surface facets, each facet has a normal vector that is kept constant during the whole computation and also an area which is optimized.

Levenberg-Marquardt loop The Levenberg-Marquardt (L-M) method first evaluates the flux f and does the first sum in Eq. (1.4). Second, the surface temperature is determined (see chapter 2). Next, the infrared flux from each facet is calculated from the

Planck's law Eq. (1.3). To make the model more realistic, we then introduce surface roughness by a simple algorithm (Lagerros, 1998). The total IR flux at the observer's location is computed (i.e. the function $\tilde{F}$ in the Eq. (1.4) is evaluated) and the second sum in Eq. (1.4) is calculated. Finally, derivatives of the χ^2 function with respect to the optimized parameters are calculated and values of the parameters are improved. This completes one L-M iteration.

Final result The process ends after a fixed number of iterations of the L-M method. The program writes out the final optimized values of parameters and creates a shape file at the end. This shape file contains the number of facets, their respective areas and normals. The reconstruction of a polyhedron from its facets and normals is called the Minkowski problem. For a detail on its treatment we refer to Lamberg and Kaasalainen (2001).

Chapter 2

Heat Conduction Equation in TPM

Infrared flux (IR) from an asteroid detected by radiometry is caused by thermal emission of photons from the surface of the asteroid. This IR flux is governed by the Planck law Eq. (1.2) which is a function of observed wavelength λ and temperature on the asteroid's surface T. Thus we need to be able to determine the surface temperature of the asteroid; the surface temperature can only be determined by solving Heat Conduction Equation (HCE). Even though there are analytical solutions of the HCE — specifically solution on a 3D sphere (Vokrouhlicky, 1998a,b) or 1D steady state solution (Bertotti et al., 2003) — they are not suitable for our problem as they introduce many simplifications. The numerical solution of the HCE is therefore necessary.

The first section of this chapter describes the implementation of HCE solver in TPM. We then present several aspects of the numerical solution that affect its accuracy as well as its computational efficiency. We then show how the error in the surface temperature propagates into error of the infrared (IR) flux from a single facet and subsequently into the error of the total flux from the asteroid. We conclude the chapter by suggesting several improvements to the current version of the TPM code that would increase accuracy and keep the efficiency reasonable.

2.1 Implementation of Heat Conduction Equation Solver in TPM

HCE — derivation Let's define an arbitrary closed three dimensional region $\mathcal{O}$. We can identify this region with an asteroid. We would like to examine the space-time distribution of temperature inside the region. In order to do that we have to determine energy equilibrium (considering only heat energy) of the region $\mathcal{O}$. The following processes can take place during a time period between t_1 and t_2:

1. Heat can be generated by a heat source inside $\mathcal{O}$. This can be, e.g., radioactive decay inside the asteroid.

2. Heat can flow through the boundary of $\mathcal{O}$.

3. Heat can be transformed to internal energy (causing the temperature to rise).

The heat generated by the heat source inside $\mathcal{O}$ during the period $t_2 - t_1$ can be obtained by:

$$\int_{t_1}^{t_2} \int_{\mathcal{O}} \rho(t, \vec{x}) f(t, \vec{x}) \, \mathrm{d}\vec{x} \, \mathrm{d}t \,,$$

where $\rho(t, \vec{x})$ is the bulk material density and $f(t, \vec{x})$ is the internal heat source density. The flow of heat through the boundary obeys the *Fourier's law*. We shall assume the Fourier's law in the following form:

$$\vec{q}(t, \vec{x}) = -\alpha(t, \vec{x}) \nabla T(t, \vec{x}) \,,$$

where $\alpha(t, \vec{x})$ is the heat conductivity of the material, $\vec{q}(t, \vec{x})$ is the local heat flux, $T(t, \vec{x})$ is the local temperature and $\nabla T(t, \vec{x})$ its gradient and $\alpha(t, \vec{x})$ is the conductivity of the material. Therefore the total flux through the region's boundary $\partial\mathcal{O}$ during the period $t_2 - t_1$ can be obtained by:

$$\int_{t_1}^{t_2} \int_{\partial\mathcal{O}} -\alpha(t, \vec{x}) \, \nabla T(t, \vec{x}) \cdot \vec{n} \, \mathrm{d}S \, \mathrm{d}t \,,$$

$\vec{n}$ being the surface normal.

Finally the change of internal energy of $\mathcal{O}$ can be expressed as:

$$\int_{\mathcal{O}} \Big[\rho(t_2, \vec{x}) c(t_2, \vec{x}) T(t_2, \vec{x}) \Big] \, \mathrm{d}x - \int_{\mathcal{O}} \Big[\rho(t_1, \vec{x}) c(t_1, \vec{x}) T(t_1, \vec{x}) \Big] \, \mathrm{d}x \,,$$

where $c(t, \vec{x})$ is the specific heat capacity of the material. It is important to note that we did not have to integrate the time variable as internal energy is a state function independent of the path the system took from one state to another. So putting it all together, we have energy conservation in integral form:

$$\begin{aligned} \int_{t_1}^{t_2} \int_{\mathcal{O}} \rho(\tau, \vec{x}) f(\tau, \vec{x}) \, \mathrm{d}\vec{x} \, \mathrm{d}\tau = & \int_{\mathcal{O}} \Big[\rho(t_1, \vec{x}x) c(t_2, \vec{x}) T(t_2, \vec{x}) \Big] \, \mathrm{d}\vec{x} \\ & - \int_{\mathcal{O}} \Big[\rho(t_1, \vec{x}) c(t_1, \vec{x}) T(t_1, \vec{x}) \Big] \, \mathrm{d}\vec{x} \\ & - \int_{t_1}^{t_2} \int_{\partial\mathcal{O}} \alpha(t, \vec{x}) \nabla T(t, \vec{x}) \cdot \vec{n} \, \mathrm{d}S \, \mathrm{d}t \,. \end{aligned}$$

Let's apply Gauss-Ostrogradsky theorem to the last integral:

$$\int_{\partial\mathcal{O}} \Big[\alpha(t, \vec{x}) \nabla T(t, \vec{x}) \Big] \cdot \vec{n} \, \mathrm{d}S = \int_{\mathcal{O}} \mathrm{div} \cdot \Big[\alpha(t, \vec{x}) \nabla T(t, \vec{x}) \Big] \, \mathrm{d}V \,.$$

If we assume that all the functions are smooth enough, we can multiply the integral form of energy conservation by $\frac{1}{t_2 - t_1}$ and by $\frac{1}{|\mathcal{O}|}$, we can then do $\lim t_2 \to t_1$ and $\lim |\mathcal{O}| \to 0^+$, $|\mathcal{O}|$ being a measure of the region $\mathcal{O}$. This way we obtain the conservation law in a differential form:

$$\rho(t, \vec{x}) f(t, \vec{x}) = \frac{\partial}{\partial t} \Big[\rho(t, \vec{x}) c(t, \vec{x}) T(t, \vec{x}) \Big] - \mathrm{div} \Big[\alpha(t, \vec{x}) \nabla T(t, \vec{x}) \Big] \,, \tag{2.1}$$

This differential energy conservation is called the Heat Conduction Equation in its general form.

HCE in asteroids In the case of an asteroid we assume that there are no heat sources inside the body, i.e. $f(t, \vec{x}) \equiv 0$. The first simplification is that we *neglect inhomogeneities and anisotropy* of the asteroid material. Which leads to HCE in the form:

$$0 \quad = \quad \frac{\partial}{\partial t} T(t, \vec{x}) - \frac{\alpha}{\rho c} \Delta T(t, \vec{x}) \,. \tag{2.2}$$

We also need to supply *boundary conditions* and *one initial condition*.

We use Dirichlet boundary condition on the surface. To determine the surface boundary condition we can use the same reasoning which we used in derivation of the HCE. However, on the surface we will not consider change in internal energy. Thus, our energy budget includes:

1. The heat flux from the Sun incident onto the surface element $\mathrm{d}S$ as our energy source. If the incident rays are perpendicular to the surface element $\mathrm{d}S$, it can be determined as $\varepsilon_{\mathrm{S}}(t)(1 - A)\,\mathrm{d}S$, where $\varepsilon_{\mathrm{S}}(t)$ is time-dependent energy flux from the Sun and A is albedo of the asteroid.

2. Part of this energy is radiated back into space due to non-zero temperature. This can be determined from the Stefan-Boltzmann law $P = \eta\sigma \mathrm{d}S\, T^4$, where σ is Stefan-Boltzmann constant, $\mathrm{d}S$ the area from which the radiation is emitted and η is emissivity.

3. Part of the energy flows into the asteroid which can be determined from the Fourier's law as $\alpha \nabla T \cdot \vec{n}\,\mathrm{d}S$.

We finally get a conservation law on the surface of the asteroid which determines the surface Dirichlet boundary condition:

$$\varepsilon_{\mathrm{S}}(t)(1 - A) \quad = \quad \eta\sigma T^4(t, \vec{x})\Big|_{\text{surface}} + \alpha \nabla T(t, \vec{x})\Big|_{\text{surface}} \cdot \vec{n} \,, \tag{2.3}$$

The internal boundary condition can either be Dirichlet or Neumann. If the Neumann internal boundary condition is used it takes the form of zero gradient:

$$\nabla T(t, \vec{x})|_{\text{in}} = 0 \,. \tag{2.4}$$

If the Dirichlet internal boundary condition is used it takes the following form:

$$T(t, \vec{x})|_{\text{in}} = T_{\text{in}} \,. \tag{2.5}$$

where T_{in} is a constant temperature. Finally, the initial condition is cast in the form:

$$T(0, \vec{x}) = T_0 \,. \tag{2.6}$$

HCE — TPM specifics

Choice of dimension and choice of numerical method TPM implements *one dimensional* (1D) *finite difference method* (FDM) numerical solver. The question is, whether solving HCE in 1D is of any physical significance for asteroids. The answer is yes. However, it is necessary to make certain assumptions. We need to be able to approximate the surface of the asteroid with planar surface elements such as illustrated in Fig. 2.2. It is then possible to solve the HCE in a thin slab extending from the surface

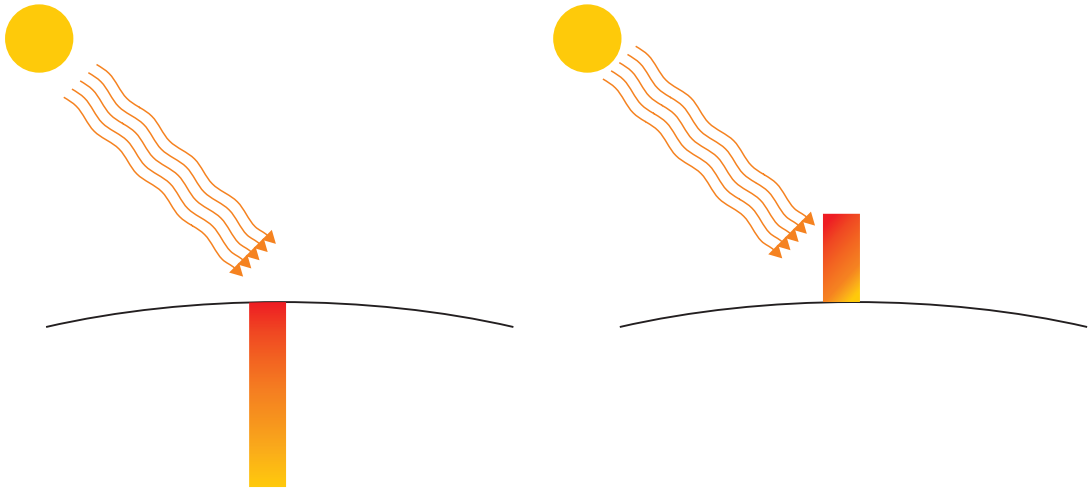

(a) Case of negligible lateral heat conduction.

(b) Case of lateral heat conduction that cannot be neglected

Figure 2.1: Illustration of negligible and non-negligible lateral heat transfer.

to the center. In any case, the TPM code triangulates the surface of an asteroid so that this assumption is fulfilled automatically.

Calculating the surface temperatures for a system of such slabs that cover the whole surface of the asteroid will yield an approximation of the surface temperature distribution. How "good" this approximation is depends mostly on the magnitude of heat transfer in the transverse direction compared to the *radial transfer*.

If we assume that: the asteroid is sufficiently large, so that temperature changes caused by varying insolation do not penetrate into its center; and the surface of the asteroid is discretized in sufficiently large facets, we can make following observations.

First, because the surface boundary condition is the source of heat for the asteroid, the temperature gradient inside the asteroid in the radial direction is bigger than the gradient in the transversal direction— the lateral boundaries are both on similar temperature as none of these boundaries is exposed to an energy source similar to the incident radiation (in the radial direction one boundary receives the heat flux from the Sun). This is illustrated in Fig. 2.1a.

In addition, the assumption of material homogeneity and isotropy results in equal heat diffusion in both transverse directions. We can therefore conclude that the *lateral heat transfer is negligible*.

Still, the lateral heat conduction cannot be neglected in general situations, we illustrate such case in Fig. 2.1b; in this case the lateral boundary "experiences" similar conditions as the surface boundary in Fig 2.1a. This case is especially important for the Yarkovsky–O'Keefe–Radzievskii–Paddack (YORP) effect.

Last, in three dimensions (3D) the choice of numerical methods is somewhat determined by their implementation complexity. Specifically, implementing FDM is very complicated on a non-cubic surface, boundary conditions have to be addressed and the resulting size of the problem would make the TPM code very slow. Also, implementing, e.g., finite elements would prove very challenging for implementation. Given the fact that we do not require high accuracy of the solution[1], we conclude that 1D approximation is not only physically relevant but also sufficient. The equations (2.2), (2.3), (2.5), (2.4) and (2.6) in 1D take the form:

[1]This fact is due to the second sum in Eq. (1.4) — we only need to achieve accuracy that is comparable to the observation data.

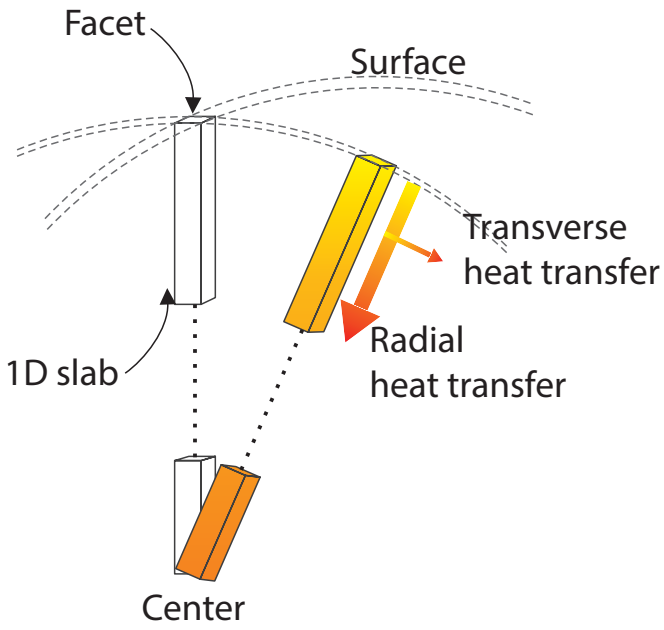

Figure 2.2: 1D approximation of an asteroid by thin slabs

$$0 = \frac{\partial}{\partial t}T(t,x) - \frac{\alpha}{\rho c}\frac{\partial^2}{\partial x^2}T(t,x)\,, \tag{2.7}$$

$$\varepsilon_{\mathrm{S}}(t)(1-A) = \eta\sigma T^4(t,x)\Big|_{\mathrm{surface}} + \alpha\frac{\partial}{\partial x}T(t,x)\Big|_{\mathrm{surface}}\,, \tag{2.8}$$

$$T(t,x)\Big|_{\mathrm{inside}} = T_{\mathrm{in}}\,, \tag{2.9}$$

$$\frac{\partial}{\partial x}T(t,x)\Big|_{\mathrm{inside}} = 0\,, \tag{2.10}$$

$$T(0,x) = T_0\,. \tag{2.11}$$

Boundary and initial conditions The TPM implementation uses Dirichlet surface boundary condition that is obtained from Eq. (2.8) and Neumann internal boundary condition obtained from Eq. (2.10). The initial condition implemented in TPM uses fixed temperature in Eq. (2.11), typically $T_0 = 100\,\mathrm{K}$.

Dimensionless HCE The TPM code implements a different form of HCE which employs a dimensionless space variable. The equations (2.7), (2.8), (2.10) and (2.11) can be recast (see App. A) into the following form[2]:

$$\frac{\partial}{\partial t}T_i(t,\chi) = \omega\frac{\partial^2}{\partial\chi^2}T_i(t,\chi)\,, \tag{2.12}$$

$$\sqrt{\omega}\Gamma\,\frac{\partial}{\partial\chi}T_i(t,\chi)\Big|_{\chi=0} = \eta\sigma T_i^4(t,\chi)\Big|_{\chi=0} - \varepsilon_{\mathrm{S}i}(t)(1-A)\,, \tag{2.13}$$

$$\frac{\partial}{\partial\chi}T_i(t,\chi)\Big|_{\chi=L} = 0\,, \tag{2.14}$$

$$T_i(0,\chi) = T_0\,, \tag{2.15}$$

[2]We only recast the boundary conditions relevant in TPM

where χ is a dimensionless space variable defined as $\chi = \frac{x}{l_s}$, Γ is thermal inertia defined as $\Gamma = \sqrt{\alpha\rho c}$, and we choose that $\chi = 0$ is the surface point and $\chi = L$ is the deepest point of the asteroid. We have also introduced the index i which suggests that the set of equations above have to be solved for each facet i. It is usual to consider ω angular rotation frequency and l_s to consider associated *skin depth*. This identification is a result of a simplified steady-state one dimensional analytical solution (see Bertotti et al. 2003). This solution defines l_s as depth at which variations from a certain *equilibrium temperature* T_{eq} are suppressed by a factor e^{-1}, i.e. at this depth the variations of temperature from T_{eq} are about a third of the variations on the surface.

Finite Difference Method in TPM The original TPM code employed Euler explicit method. However, this method is only conditionally stable and the original implementation did not guarantee stability of the solution. We have reworked the solver and implemented the Crank-Nicholson (C-N) implicit scheme. Unlike other Finite Difference Methods (FDM) for Partial Differential Equations (PDE), Crank-Nicholson has errors of the order $\mathcal{O}(\Delta t^2) + \mathcal{O}(\Delta x^2)$ as $(\Delta t \to 0\,, \Delta x \to 0)$. This property of C-N method makes it possible for a less dense grid in time domain[3] while a similar discretization error is preserved. The TPM code uses equidistant grid in space domain (the grid spacing Δx is equal to a fixed multiple of the *skin depth*) and non-equidistant grid in time domain. The system (2.12–2.15) transformed into finite differences with Neumann boundary condition and C-N scheme results in the following matrix (for simplicity, we omit the facet index i introduced above, however, we have to keep in mind that the matrix problem has to be solved for each facet):

$$\begin{pmatrix} 2+2b & -2b & 0 & 0 & 0 & \dots & 0 \\ -b & 2+2b & -b & 0 & 0 & \dots & 0 \\ 0 & -b & 2+2b & -b & 0 & \dots & 0 \\ \vdots & & \ddots & \ddots & \ddots & & \vdots \\ 0 & \dots & 0 & 0 & -br & 2+2b & -b \\ 0 & \dots & 0 & 0 & 0 & -b & 2+2b \end{pmatrix} \times \begin{pmatrix} u_0^n \\ u_1^n \\ u_2^n \\ \vdots \\ u_{J-1}^n \end{pmatrix} =$$
$$= \begin{pmatrix} (2-2b)u_0^{n-1} + 2bu_1^n \\ bu_0^{n-1} + (2-2b)u_1^{n-1} + bu_2^{n-1} \\ bu_1^{n-1} + (2-2b)u_2^{n-1} + bu_3^{n-1} \\ \vdots \\ bu_{J-2}^{n-1} + (2-2b)u_{J-1}^{n-1} + bu_J^{n-1} + bu_J^n \end{pmatrix} \tag{2.16}$$

We also switched to the following *notation for discretized temperature*: u_j^n denotes temperature at space grid point j and time grid point n; $b \equiv \omega\frac{\Delta t}{\Delta\chi^2}$; J is the grid point on the asteroid surface. Note that as a result of the Neumann BC, the matrix is no longer symmetric (see App. B).

Discretization of the surface boundary condition There is one more equation in the set — the surface boundary condition Eq. (2.13):

$$\eta\sigma(u_J^n)^4 + \frac{\Gamma\sqrt{\omega}}{\Delta\chi}u_J^n - \varepsilon_S(n)(1-A) - \frac{\Gamma\sqrt{\omega}}{\Delta\chi}u_{J-1}^n \;=\; 0\,. \tag{2.17}$$

[3]The Euler method has discretization errors of the order $\mathcal{O}(\Delta t) + \mathcal{O}(\Delta x^2)$ as $(\Delta t \to 0\,, \Delta x \to 0)$.

This equation is interrelated with the matrix system via the last term u^n_{J-1} and transforms the otherwise linear set into a *nonlinear one*. To avoid this complication we simply substitute u^n_{J-1} by u^{n-1}_{J-1}, i.e. we use the temperature from the previous time grid point which leads to:

$$\eta\sigma(u^n_J)^4 + \frac{\Gamma\sqrt{\omega}}{\Delta\chi}u^n_J - \varepsilon_{\mathrm{S}}(n)(1-A) - \frac{\Gamma\sqrt{\omega}}{\Delta\chi}u^{n-1}_{J-1} \;=\; 0\,. \tag{2.18}$$

This equation has can be solved independently of the matrix problem above. We implemented the Laguerre's method (Press et al., 1992) to find roots of the polynomial above. Once the surface temperature u^n_J is known, the tridiagonal system can be solved e.g. by the *tridag* algorithm from (Press et al., 1992); but because the matrix is diagonally dominant, it is advantageous to make use of that feature and use a LAPACK routine *?dtsvb* from Intel MKL library. According to our measurements, the LAPACK routine was about 30% faster than the *tridag* algorithm.

2.2 Analysis of accuracy of the TPM heat conduction equation solver

This section presents factors that contribute to the total error in the numerical solution of the Heat Conduction Equation (HCE). We describe only the errors that are significant with respect to the implementation of the HCE solver in the TPM code. In order to estimate the most significant errors, we have conducted a large number of numerical tests to determine:

1. how accurate the implemented solution of the HCE is,
2. how the error in various parameters propagates into the integrated infrared (IR) flux from the asteroid,
3. whether the algorithm can be made more effective with respect to the required accuracy.

This section is mostly concerned with the first item. Second and third items are discussed in next sections.

Introduction We have identified the following aspects of the numerical solution of the HCE that, if not addressed, contribute most profoundly to the total error in the surface temperature of an asteroid:

1. temperature relaxation,
2. initial temperature (initial condition of the partial differential equation),
3. integration depth,
4. surface boundary condition,
5. grid density.

We discuss these aspects in the following subsections; we also present numerical results of the conducted tests.

2.2.1 Temperature relaxation

We start this subsection by defining the term relaxed temperature.

Relaxed temperature We consider the temperature within an asteroid relaxed when it follows a *periodic*, *stationary* evolution. It is important to note that the periodicity refers to the insolation incident on a given surface element of the asteroid which is not necessarily the same as either the orbital or rotational period. The period of this evolution depends on rotational and orbital periods and on the asteroid's spin axis orientation with respect to the orbital plane. The requirement for stationary evolution refers to the fact that the temperature at any given instant of a period is the same for other periods (provided that all other parameters stay the same between the periods).

Diurnal and seasonal components of temperature evolution We illustrate two limit orbital configurations in Fig. 2.3. The temperature profile in the asteroid displayed in Fig. 2.3a is governed by rotational period. On the other hand, the temperature profile in the asteroid in Fig. 2.3b is governed by orbital period. In case of an asteroid orbiting and rotating in an arbitrary geometry, two main components contribute to the temperature profile in the asteroid.

1. The *diurnal component* of temperature profile that is due to the asteroid's spin motion and relates to the period of rotation.

2. The *seasonal component* of temperature profile that is due to the asteroid's orbital motion and relates to the period of orbit.

The weight of each component depends on the orbital configuration.

Implication of diurnal and seasonal components for temperature relaxation The nature of finite difference methods implies that in order to achieve a relaxed, stationary state, several insolation periods have to be iterated. If we consider the diurnal and seasonal components above, it is evident that at least several orbital periods have to be iterated. This poses a serious challenge in the numerical calculation as the rotational periods are usually of the order of hours while the orbital periods are of the order of years; consequently, to be able to describe the diurnal component, we need sufficiently dense time grid (usually of the order of seconds) and to be able to achieve the relaxed, stationary state, we need to run the solver for several orbital periods (usually several years).

Numerical results We have conducted numerical tests to determine number of orbital periods necessary to reach a relaxed state.

Testing methodology We introduced 5 orbital configurations displayed in Fig. (2.4) and two distinct asteroid materials — basalt and regolith (see Tab. 2.1). We solved the HCE with 1D FDM solver using Crank-Nicholson method with the following Initial Conditions (IC) and Boundary Conditions (BC):

1. IC: Temperature within each slab is determined by $T_{\mathrm{eq}} = \sqrt[4]{\langle \varepsilon_{\mathrm{S}} \rangle \frac{1-\mathrm{A}}{\epsilon\sigma}}$, where $\langle \varepsilon_{\mathrm{S}} \rangle$ is the average incident insolation during one orbit. We call T_{eq} an *equilibrium temperature*.

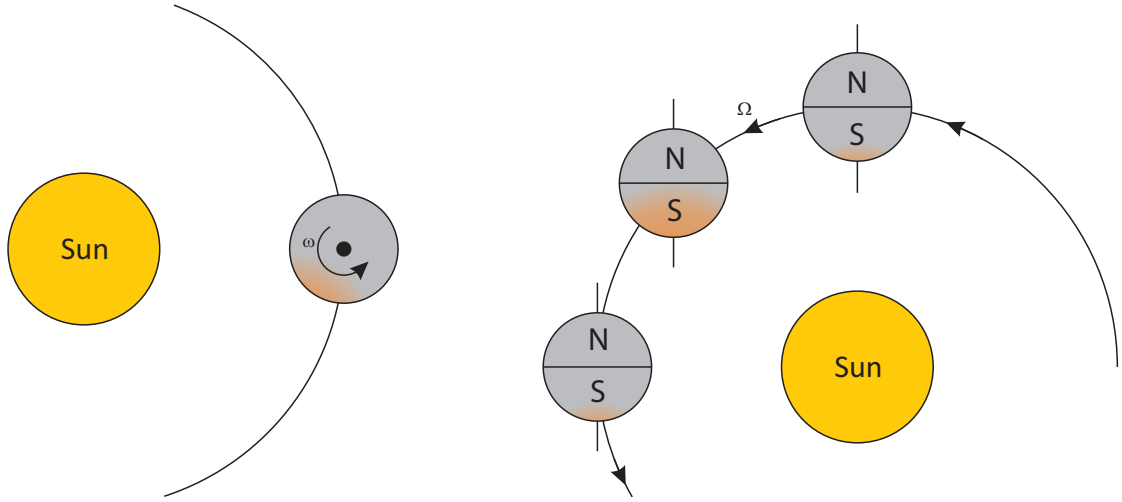

(a) Diurnal component (b) Seasonal component

Figure 2.3: The effect on temperature profile in an asteroid due to diurnal and seasonal components.

BC: Dirichlet BC inside the asteroid $T \equiv T_{\text{eq}}$, Dirichlet BC on the surface determined by energy conservation (see Eq. (2.13)).
We designate this IC-BC combination MDir.

2. IC: same as above.
   BC: Neumann BC inside the asteroid (see Eq. (2.14)), Dirichlet BC on the surface determined by energy conservation (see Eq. (2.13)).
   We designate this IC-BC combination as MNeu

3. IC: Temperature within all 1D slabs is set to $T = 100\,\text{K}$.[4]
   BC: same as in (2.).
   We designate this IC-BC combination MNeu100

Further configuration parameters were: external source luminosity of $3.839 \times 10^{26}\,\text{W}$, distance from the sun of 2.5 AU, emissivity of the asteroid relative to a black body of $\eta = 0.9$, albedo of the asteroid of $A = 0.1$, space grid size for basalt material $x_{\text{max}}^{\text{B1}} = 30\,\text{m}$ and for regolith material $x_{\text{max}}^{\text{R1}} = 3\,\text{m}$, space step size of FDM $\Delta x = 0.005\,\text{m}$, time step size FDM $\Delta t = 1\,\text{s}$, orbital period of one year and rotational period of 10 hours. Further, we saved the temperature profile in the 1D slab every 10 000 s and let the solver run for three orbital periods.

Table 2.1: Heat conductivity (α), specific heat capacity (c) and material density (ρ) used as material parameters in testing. We also provide the respective thermal inertias $\Gamma = \sqrt{\alpha \rho c}$.

material	$\rho\,[\text{kg} \cdot \text{m}^{-3}]$	$c\,[\text{J} \cdot \text{K}^{-1} \cdot \text{kg}^{-1}]$	$\alpha\,[\text{W} \cdot \text{K}^{-1} \cdot \text{m}^{-1}]$	$\Gamma\,[\text{J} \cdot \text{m}^{-2} \cdot \text{K}^{-1} \cdot \text{s}^{-1/2}]$
basalt (B1)	2500	680	2.5	2062
regolith (R1)	1500	680	0.03	174.9

[4] This is the method that is employed in the current version of the TPM code.

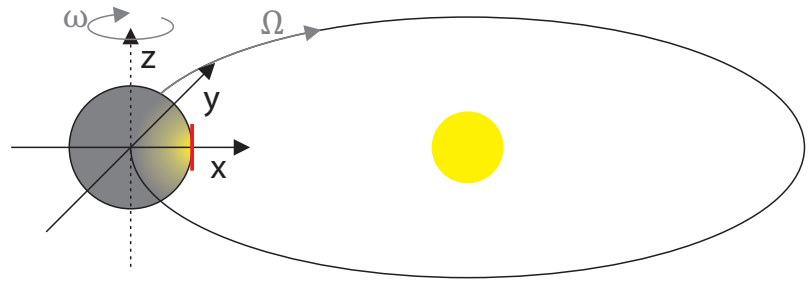

(a) Orbital configuration n1-s1

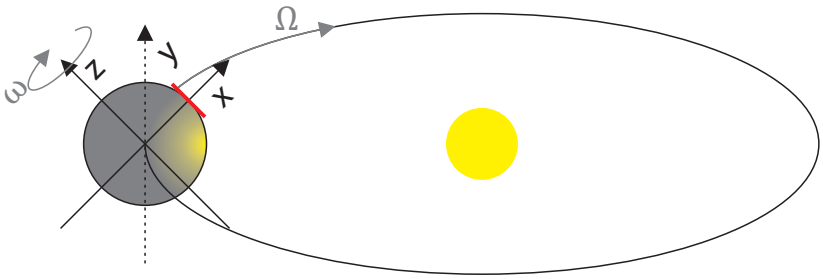

(b) Orbital configuration n1-s2

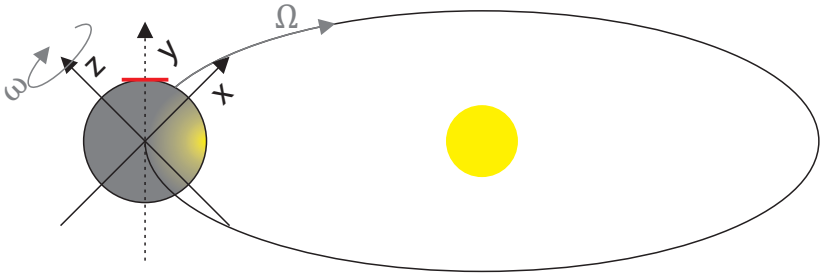

(c) Orbital configuration n2-s2

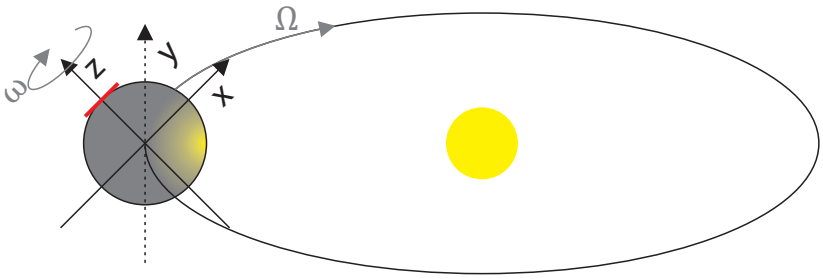

(d) Orbital configuration n3-s2

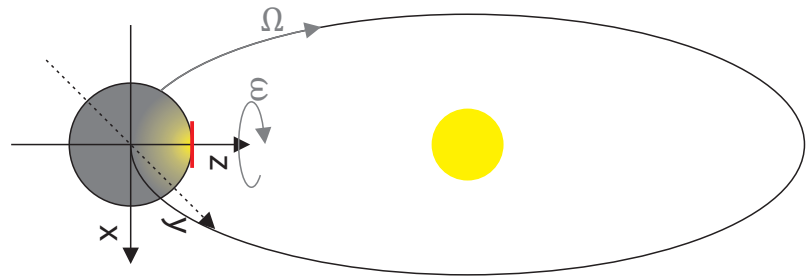

(e) Orbital configuration n3-s3

Figure 2.4: Orbital configurations used in relaxation testing. The red line denotes surface element which was used for the test. The configuration is specified by a surface normal of the asteroid (nx) and by angle between the orbital plane normal and z axis of the asteroid (sx) along with the assumption that the sun always lies in x-z plane at the beginning ($t = 0$). The orbit is circular; the illustrations suggest perspective view.

Test results We present the surface temperature relaxation of the methods with IC-BC MDir and MNeu100 in Fig. 2.4 and Fig. 2.4; we do not show results for IC-BC MNeu as they are almost identical to the results of MDir. The presented graphs clearly demonstrate that relaxation[5] is strongly bound to the orbital configuration and is determined by the period of insolation rather than by the orbital or rotational period.

We can also infer dependence of relaxation on thermal parameters of the asteroid. We can see that in the case of regolith material, the solution reaches relaxed state faster. This is because regolith has lower thermal inertia (see Tab. 2.1) and thermal inertia is a good measure of the lag between the incident insolation on the surface the its effect inside the asteroid. And the larger this lag, the longer it takes for the system to relax.

We can also note a surprising dependence on the type of BC inside the asteroid; we will develop this point further in this chapter.

Conclusion Unrelaxed solution can generate errors of the order of tens of Kelvins (note that we use absolute values on purpose, these will be useful in the next section; the temperature on the surface ranges from $\sim 80\,\mathrm{K}$ to $\sim 220\,\mathrm{K}$) regardless of how dense we make the space and time grids of the FDM[6]. Therefore, proper temperature relaxation is essential for an accurate solution. On the other hand, iterating over several orbital periods with a sufficiently precise time resolution to cover diurnal temperature evolution is very time consuming. Fortunately, from the performed tests we can conclude that the solution with IC-BC MDir and MNeu can be considered sufficiently relaxed after one orbital period[7] (even though in several orbital configurations the solution can be considered relaxed much earlier, we consider one orbital period as the safe time necessary for the relaxation of temperature). But, this cannot be said about the solution with IC-BC MNeu100. Even after three periods, the temperature between the same instants in third and second periods differs by several Kelvins.

2.2.2 Initial temperature

Because of the current implementation of HCE solver in TPM code as described in section 2.1, we were interested how fast the temperature relaxes in the case of initial condition with arbitrary temperature. We expected that the numerical solution will take longer to relax if the initial temperature is set far away from the *equilibrium temperature*.

Initial condition At the beginning of our calculation, we have no information about temperature distribution within a 1D slab. However, we can assume that regardless of the initial condition, the solution should converge to "correct" temperature profile. This assumption is valid because of the periodic nature of our problem. The question is actually two-fold. We should first examine whether the assumption about convergence is correct. Next, we should determine how fast the solution converges. However, in this section we only determine the latter because once we see that the convergence is slow, we take no interest in such solution whether it converges or not.

[5] By relaxation we mean the time necessary for the solution to attain periodic, stationary evolution.

[6] Note (see the paragraph on Testing Methodology above) that we have used a very dense grid in both time and space domains.

[7] Whether we can consider the solution relaxed depends on the accuracy of the solution that we seek. Therefore, we make this conclusion with the foreknowledge of the necessary precision which is discussed later in this chapter.

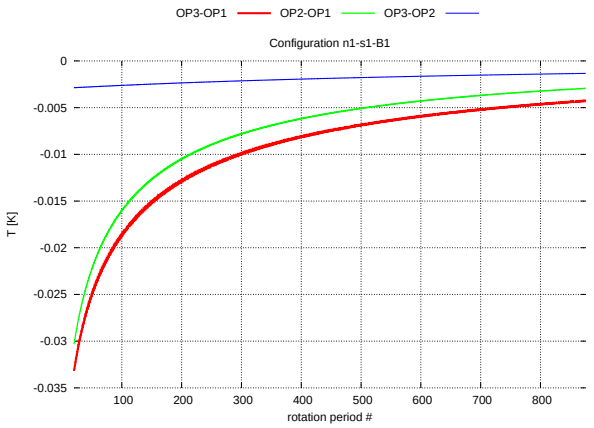

(a) Relaxation test for configuration n1-s1-B1-MDir

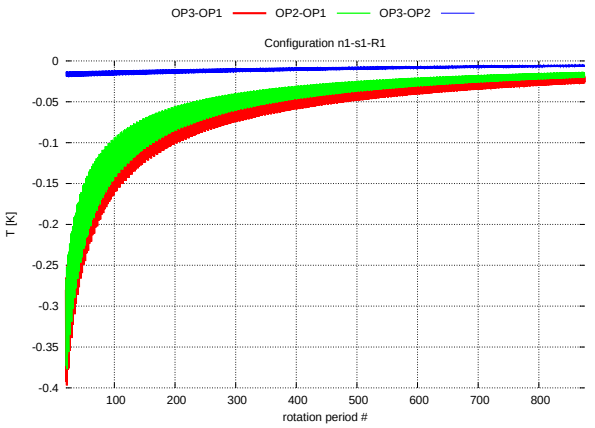

(b) Relaxation test for configuration n1-s1-R1-MDir

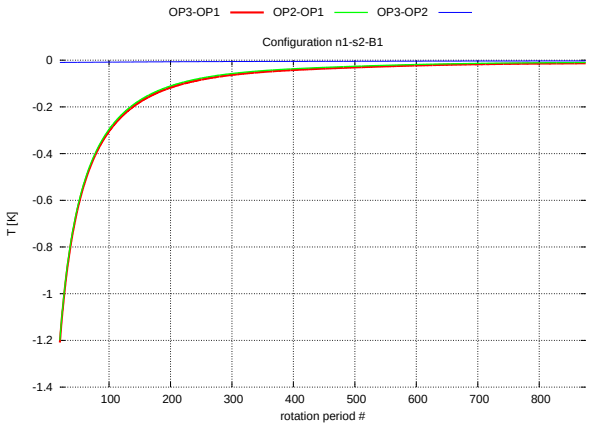

(c) Relaxation test for configuration n1-s2-B1-MDir

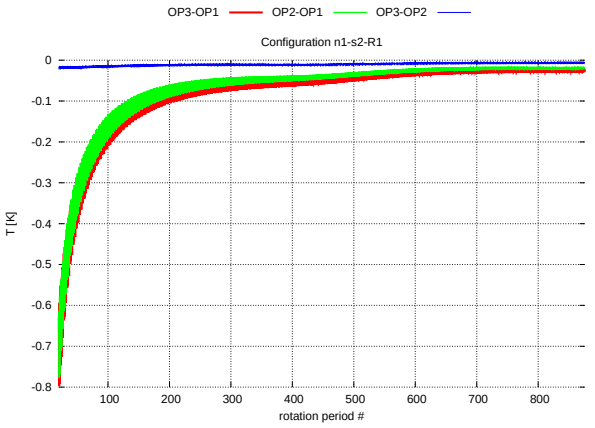

(d) Relaxation test for configuration n1-s2-R1-MDir

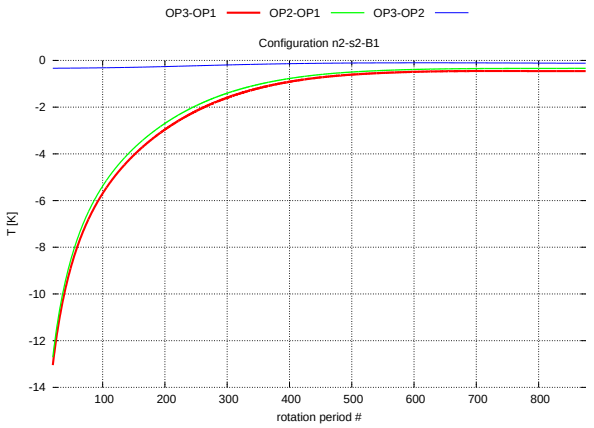

(e) Relaxation test for configuration n2-s2-B1-MDir

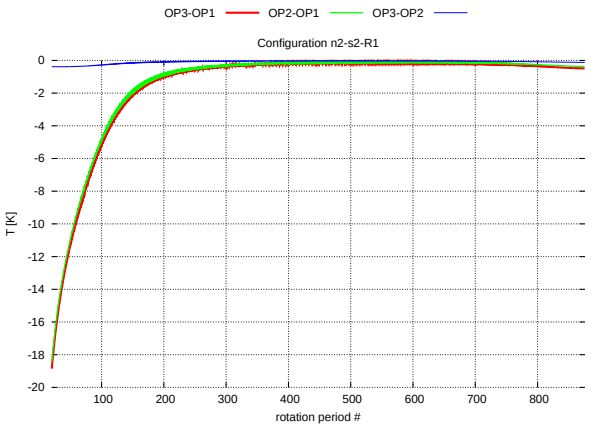

(f) Relaxation test for configuration n2-s2-R1-MDir

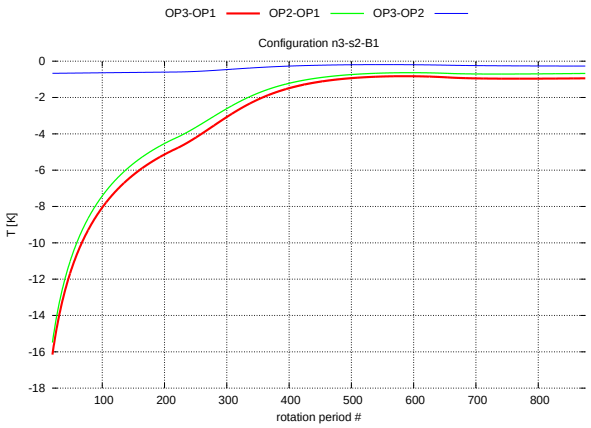

(g) Relaxation test for configuration n3-s2-B1-MDir

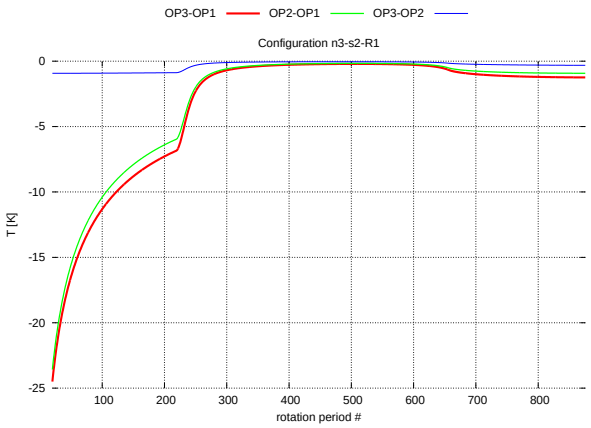

(h) Relaxation test for configuration n3-s2-R1-MDir

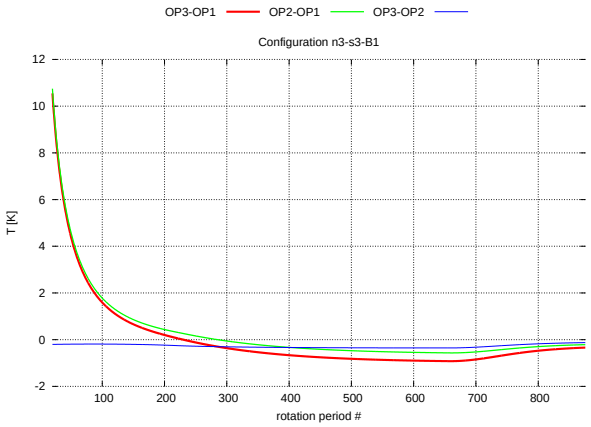

(i) Relaxation test for configuration n3-s3-B1-MDir

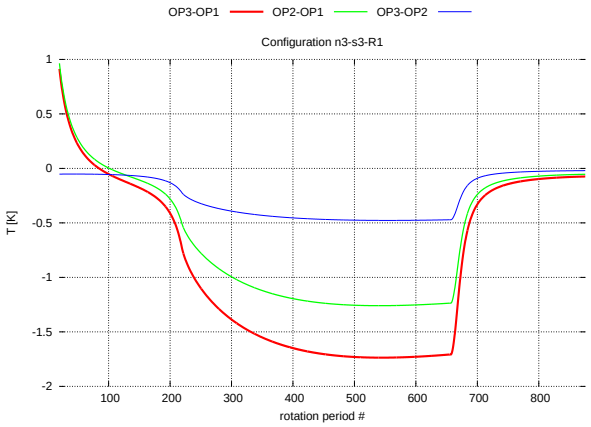

(j) Relaxation test for configuration n3-s3-R1-MDir

Figure 2.4: Test of temperature relaxation between orbital periods. Each panel shows temperature difference between the same time instants in different orbital periods (OPx) in different configurations. For the meaning of nx-sy see Fig. 2.4, B1 and R1 see Tab. 2.1, Mx see discussion about IC and BC above. The plots start at the 20^{th} rotational period.

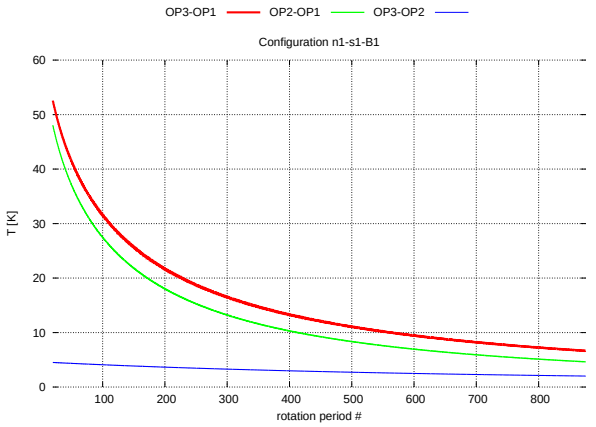

(a) Relaxation test for configuration n1-s1-B1-MNeu100

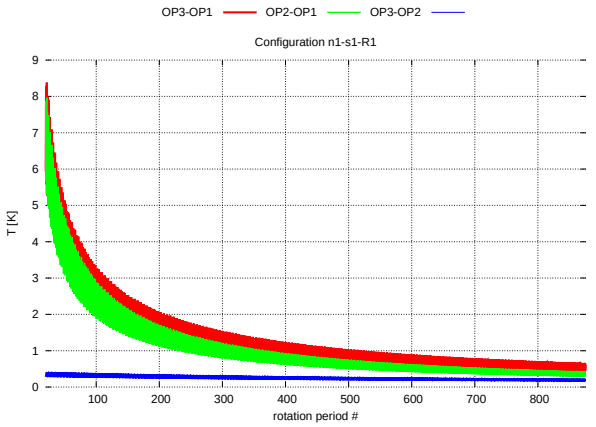

(b) Relaxation test for configuration n1-s1-R1-MNeu100

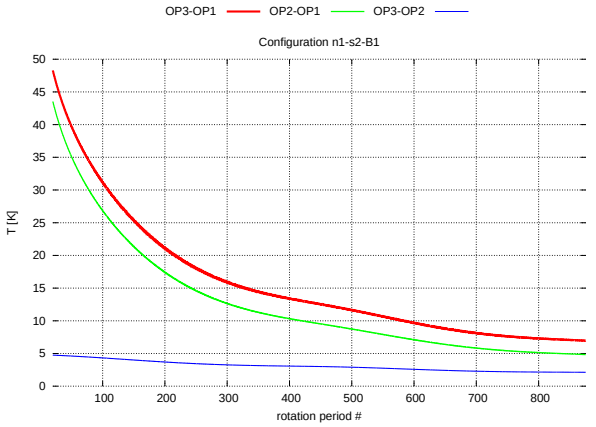

(c) Relaxation test for configuration n1-s2-B1-MNeu100

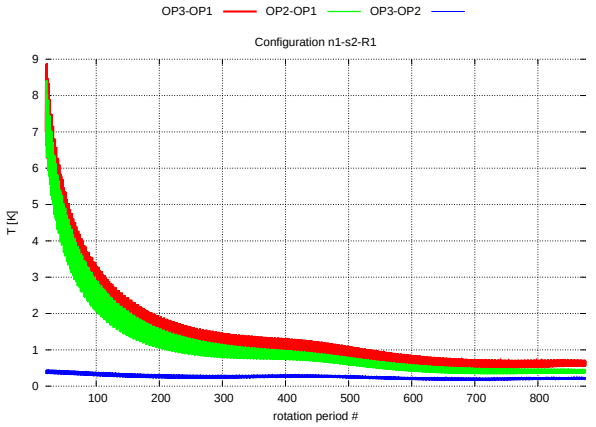

(d) Relaxation test for configuration n1-s2-R1-MNeu100

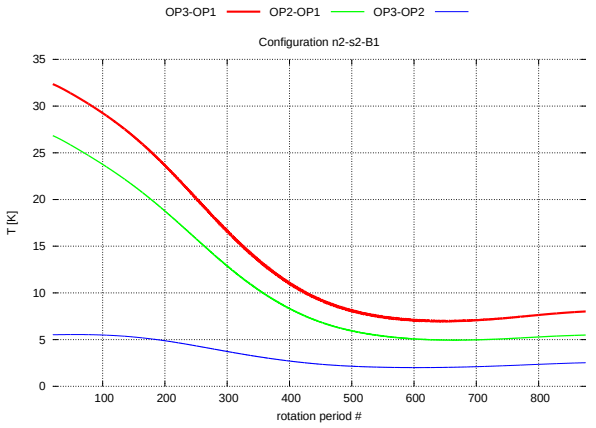

(e) Relaxation test for configuration n2-s2-B1-MNeu100

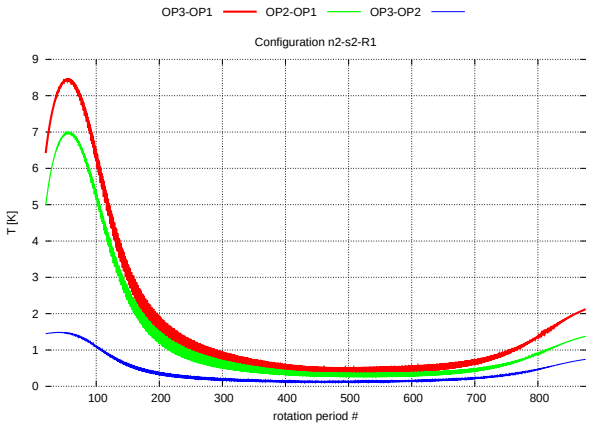

(f) Relaxation test for configuration n2-s2-R1-MNeu100

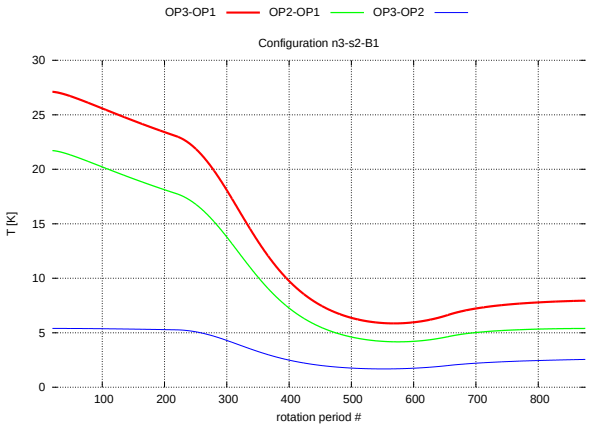

(g) Relaxation test for configuration n3-s2-B1-MNeu100

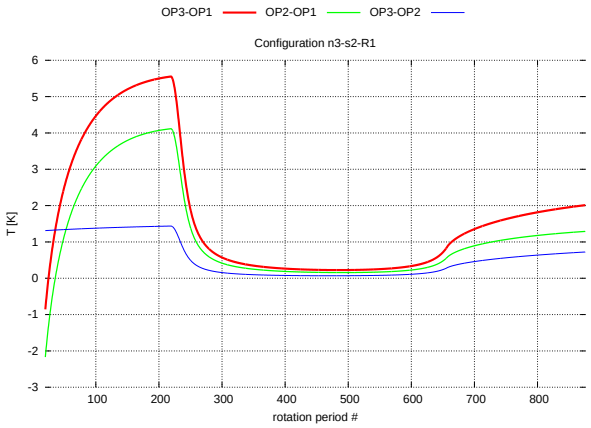

(h) Relaxation test for configuration n3-s2-R1-MNeu100

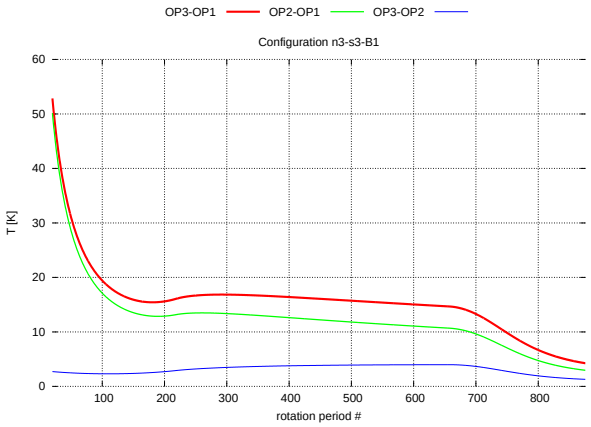

(i) Relaxation test for configuration n3-s3-B1-MNeu100

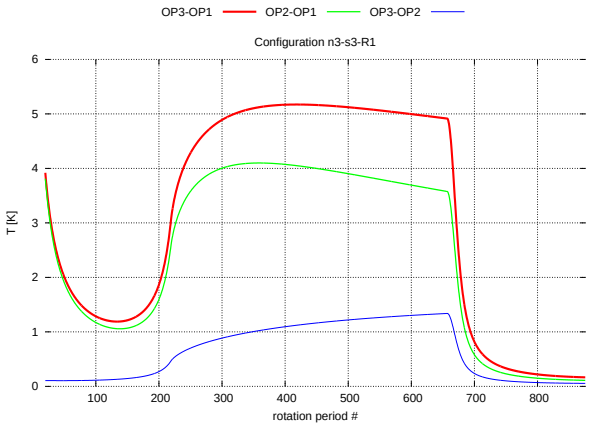

(j) Relaxation test for configuration n3-s3-R1-MNeu100

Figure 2.4: Test of temperature relaxation between orbital periods. Each panel shows temperature difference between the same time instants in different orbital periods (OPx) in different configurations. For the meaning of nx-sy see Fig. 2.4, B1 and R1 see Tab. 2.1, Mx see discussion about IC and BC above. The plots start at the 20$^{\text{th}}$ rotational period.

Selection of initial condition We can either set the initial condition to an arbitrary temperature within the asteroid or we can try to determine a certain *equilibrium temperature*.[8]

The concept of equilibrium temperature comes from the idea that an asteroid starts periodic motion with temperature $T = 0\,\mathrm{K}$[9]. As it receives energy from the sun, the heat flows through the asteroid. This process continues until a certain point is reached when the heat only flows through the center without raising temperature there. This temperature can be obtained from the average insolation the asteroid receives:

$$T_{\mathrm{eq}} = \sqrt[4]{\langle \varepsilon_{\mathrm{S}} \rangle \frac{1 - \mathrm{A}}{\eta \sigma}}\,, \tag{2.19}$$

where $\langle \varepsilon_{\mathrm{S}} \rangle$ is the average insolation incident on a facet during one orbital period.

Numerical results

Testing methodology Testing methodology is almost identical to the one described in section 2.2.1. In order to analyze the effect of TPM implemented initial condition, we compared the surface temperature determined by the HCE solver with IC-BC MNeu100 (see 2.2.1) with a reference solution. As the reference solution we chose the surface temperature determined in the third orbital period using IC-BC MDir and MNeu. All parameters of the tests were identical to those described in section 2.2.1.

The selection of the most exact temperature raises an important question, whether it is more correct to use Dirichlet or Neumann boundary condition inside the asteroid.

According to our observations, the Dirichlet condition gains better results, especially in the case of insufficient integration depth. However, it requires knowledge of the "correct" internal temperature. The advantage of the Neumann condition primarily lies in the fact that we do not need to know a proper internal temperature. See discussion in section 2.4.2 on how to choose a good internal temperature.

Test results The panels in Fig. 2.4 show the comparison. We do not plot the comparison of MNeu against MNeu100 as the results are almost identical to MDir against MNeu. These panels show that in certain configurations (e.g. n3-s2-B1) temperature determined with MNeu100 is several Kelvins (even over ten Kelvins) different from the solution which we consider to be relaxed even in the third orbital period of MNeu100. We can conclude that convergence with improperly set initial condition is very slow.

We can also see that the effect of arbitrary IC is especially profound for basaltic materials while for regolith the effect is somewhat mitigated.

2.2.3 Integration depth

Maximum depth

Asteroid size assumption At the beginning of section 2.1 we were discussing the choice of dimension for our solver. We also mentioned that if we can approximate the surface of the asteroid with planar surface elements, the one dimensional approximation can be used. Another assumption that is necessary for our approach to HCE to work is

[8] We can definitely choose initial condition as a function of space variable, however, this would either result in a situation similar to arbitrary temperature or equilibrium temperature.

[9] This temperature can be actually arbitrary.

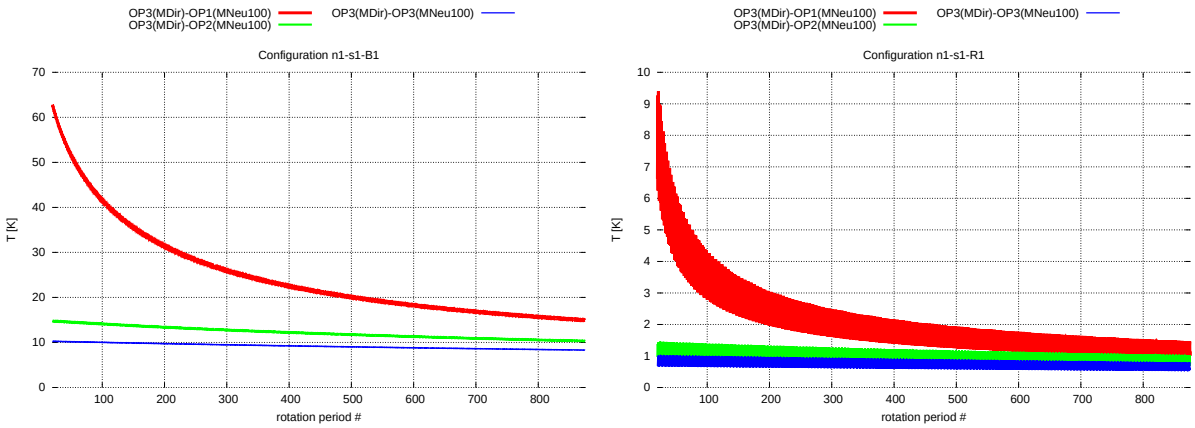

(a) Initial condition test for configuration n1-s1-B1

(b) Initial condition test for configuration n1-s1-R1

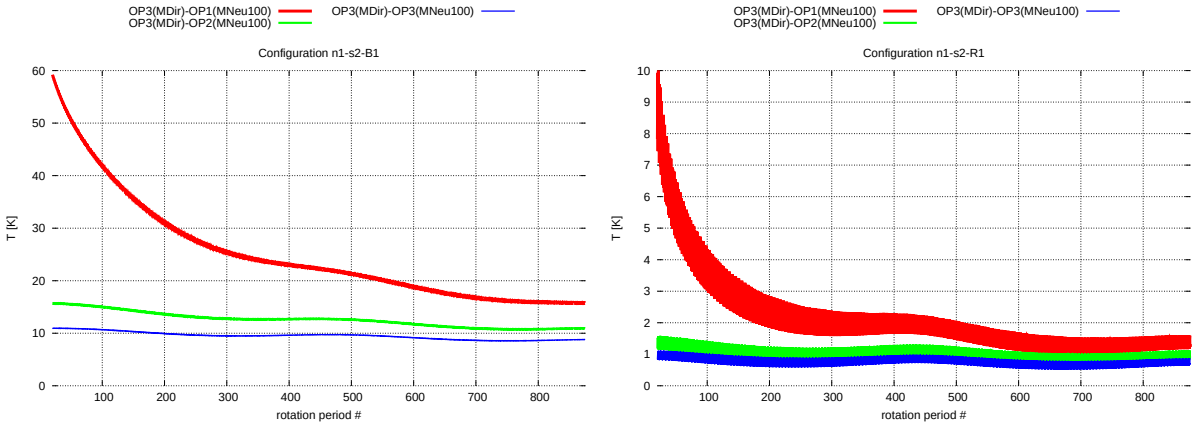

(c) Initial condition test for configuration n1-s2-B1

(d) Initial condition test for configuration n1-s2-R1

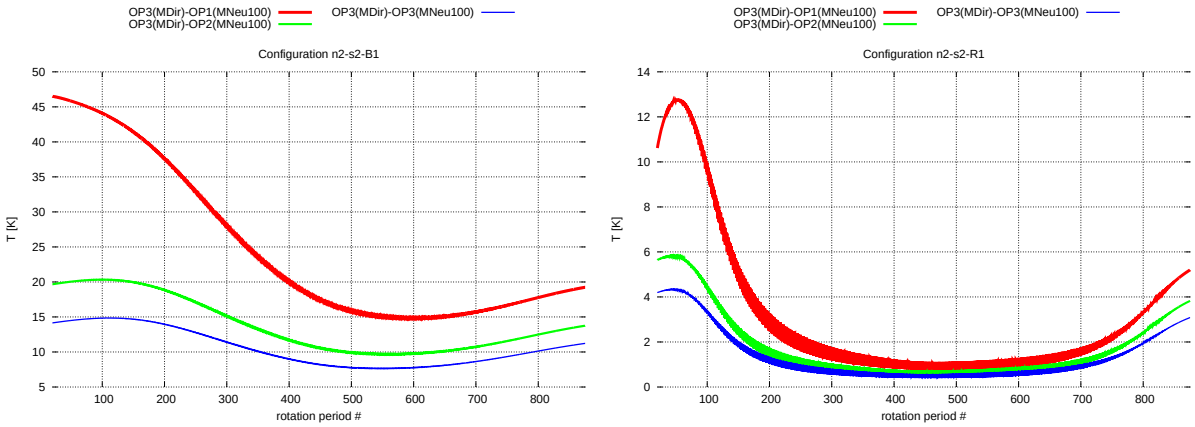

(e) Initial condition test for configuration n2-s2-B1

(f) Initial condition test for configuration n2-s2-R1

Figure 2.5: Test of relaxation with initial condition set to 100 K. Each panel shows temperature difference between a reference surface temperature and temperature determined with the method MNeu100. For the meaning of nx-sy see Fig. 2.4, B1 and R1 see Tab. 2.1, Mx see discussion about IC and BC above. The plots start at the 20$^{\text{th}}$ rotational period.

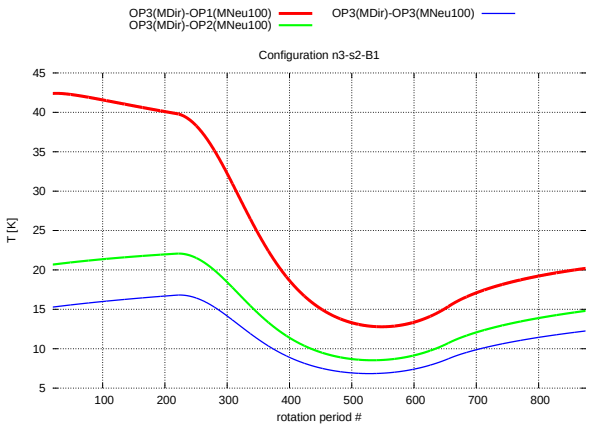

(g) Initial condition test for configuration n3-s2-B1

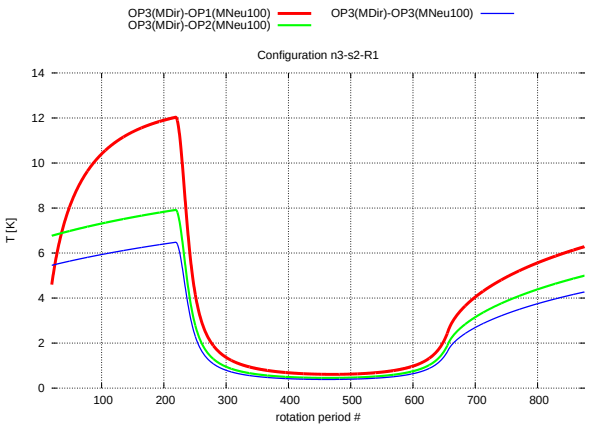

(h) Initial condition test for configuration n3-s2-R1

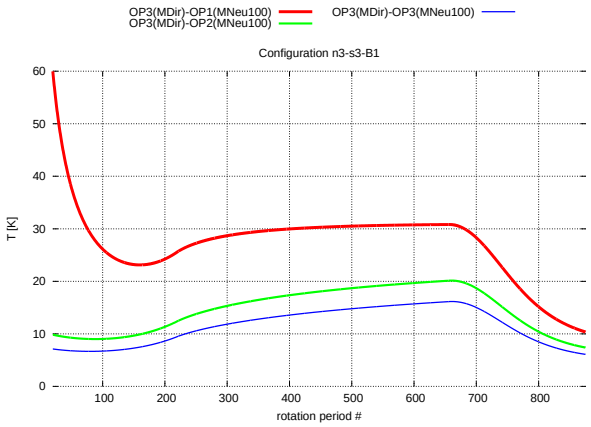

(i) Initial condition test for configuration n3-s3-B1

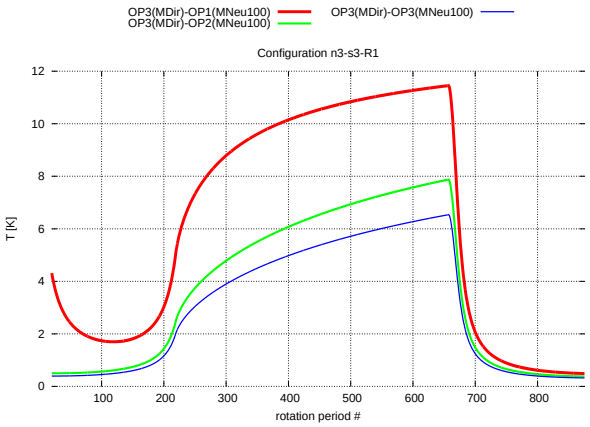

(j) Initial condition test for configuration n3-s3-R1

Figure 2.4: Test of relaxation with initial condition set to 100 K. Each panel shows temperature difference between a reference surface temperature and temperature determined with the method MNeu100. For the meaning of nx-sy see Fig. 2.4, B1 and R1 see Tab. 2.1, Mx see discussion about IC and BC above. The plots start at the 20$^{\text{th}}$ rotational period.

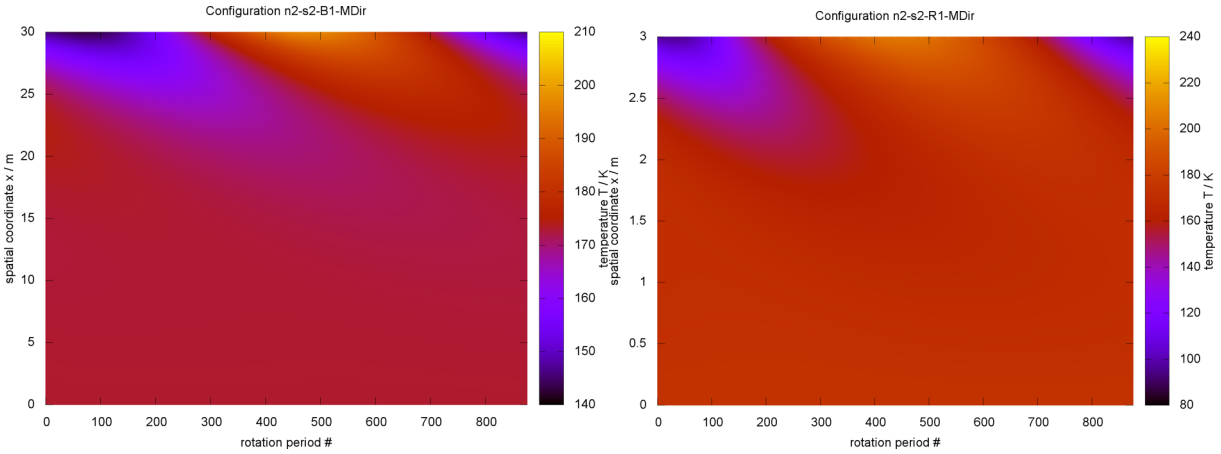

(a) Penetration depth for configuration n2-s2-B1 (b) Penetration depth for configuration n2-s2-R1

Figure 2.5: Sample temperature profiles to illustrate penetration depth.

that we need a sufficiently large asteroid. This is quite essential for our formulation of the problem. In particular, we have chosen either Dirichlet or Neumann boundary condition (BC) in the form of Eq. (2.9) and (2.10). These conditions tacitly assume that the depth of the asteroid is big enough that the temperature there is either constant or there is no heat flow through the center of the asteroid. This is not necessarily true for small asteroids. Hence, for these asteroids our solution of HCE will not work.

On the other hand, if we chose the maximum depth of a km or more as in a "real" large asteroid, in accordance with our size assumption, we would face a rather large matrix problem in Eq. (2.16) which would be extremely demanding on computational resources. Fortunately, the temperature does not penetrate more than several metres or tens of meters below the surface for regolith and basaltic materials.

Choosing the right maximum depth The maximum depth that is necessary can be easily determined from the temperature profile inside an asteroid. We illustrate such profiles in Fig. 2.5. The panels suggest that for basalt and regolith with properties from Tab. 2.1 the penetration depths in orbital configurations n2-s2 are about $\sim 20\,\mathrm{m}$ and $\sim 1.5\,\mathrm{m}$ respectively. The depth depends not only on the asteroid material but also on the orbital configuration (e.g. for the configuration n1-s1 the penetration depth for basalt is only about $\sim 1.5\,\mathrm{m}$).

Skin depth However, we would like to be able to approximate the maximum depth without having to produce a series of temperature profiles such as in Fig. 2.5. A concept of *skind depth* can be used. This concept arises in 1D steady state simplified analytical solution to HCE in an asteroid that rotates about its axis (without orbital motion) in orbital configuration n1-s1 (see Fig. 2.4). The temperature profile in the asteroid can then be written as:

$$T(t,x) \;=\; T_{\mathrm{eq}} + f(t,x)\,,$$

where T_{eq} is a constant temperature and $f(t,x)$ determines how much the temperature $T(t,x)$ differs from the constant temperature. The spatial dependence of the function $f(t,x)$ can be written (see App. C:

$$f(t,x) \;\sim\; \mathrm{e}^{-\sqrt{\frac{\omega\rho c}{2\alpha}}x}\,,$$

where ω is the angular frequency of the rotational motion. We can now see that the term $\sqrt{\frac{\omega\rho c}{2\alpha}}$ is just an inverse of such a depth where the changes from the constant temperature T_{eq} are suppressed by a factor of e^{-1}. This depth is called the *skin depth* d.

$$d \stackrel{\mathrm{def}}{=} \sqrt{\frac{2\alpha}{\omega\rho c}}\,, \tag{2.20}$$

We illustrate the values of skin depth for materials used in our test in Tab. 2.2. Because of the geometry n1-s1, we also can use the formula (2.20) to calculate the skin depth for the seasonal component of temperature (i.e. in a situation when the asteroid orbits but does not rotate) by simply using the orbital period instead of the rotational one. If we compare the characteristic penetration depth from Fig. 2.5 with data in Tab. 2.2 for basalt the characteristic penetration depth is about 6 times bigger than the skin depth based on orbital period and for regolith the characteristic depth is about three times bigger than the skin depth based on orbital period.

Table 2.2: The skin depth d for basalt and regolith materials with two periods — 10 hrs and 1 y. Because of the nature of configuration n1-s1, the period can either be considered rotational or orbital. For the basalt and regolith parameters see Tab. 2.1.

Material	Period	skin depth [m]
Basalt	10 h	0.1298
Regolith	10 h	0.01836
Basalt	1 y	3.842
Regolith	1 y	0.5434

Numerical results

Testing methodology We used the same 5 orbital configurations as in the section 2.2.1 — see Fig. 2.4; conducted the tests with the basalt and regolith materials from Tab. 2.1 with initial and boundary conditions MDir and MNeu (see their description in section 2.2.1); calculated temperature profiles in basalt for three maximum depths 1.5 m, 3 m and 30 m and in regolith 0.5 m, 1 m and 3 m and used data from the third period (when the system is relaxed). The depths $x_{\max} = 30\,\mathrm{m}$ and $x_{\max} = 3\,\mathrm{m}$ in basalt and regolith respectively were used as a reference because in further testing we determined that temperature does not penetrate beyond this depth. The remaining parameters of were the same as described in testing methodology in section 2.2.1.

Test results We present the results of the tests in Fig. 2.5. We immediately conclude that incorrect integration depth has profound effect on the accuracy of the surface temperature specially in basalt material of the order of tens of Kelvins. This error is mitigated to some degree in regolith materials.

We also conclude that Dirichlet internal BC gives more precise results. We explain that by the fact that if we integrate very deep (e.g. 30 m in the case of basalt), both boundary conditions give very similar temperatures inside the asteroid. If we then use the Dirichlet boundary condition with a less deep integration we basically scale the problem onto a smaller range. This scaling gives better results than Neumann's condition.

Last, we note periodic behaviour. The surface temperature calculated with different maximum integration depth reaches maximum at different instants; the deeper we integrate, the later the maximum occurs. This results in the periodic behaviour[10] that is apparent in the panels 2.6a – 2.6e.

2.2.4 Surface boundary condition

In this subsection we briefly discuss the boundary condition on the surface — Eq. (2.13). In section 2.1 we simplified this equation in finite differences (Eq. 2.17):

$$\eta\sigma(u_J^n)^4 + \frac{I\sqrt{\omega}}{\Delta\chi}u_J^n - \varepsilon_{\mathrm{S}}(n)(1-A) - \frac{\Gamma\sqrt{\omega}}{\Delta\chi}u_{J-1}^n \;=\; 0\,,$$

by replacing the term u_{J-1}^n with u_{J-1}^{n-1} resulting in:

$$\eta\sigma(u_J^n)^4 + \frac{I\sqrt{\omega}}{\Delta\chi}u_J^n - \varepsilon_{\mathrm{S}}(n)(1-A) - \frac{\Gamma\sqrt{\omega}}{\Delta\chi}u_{J-1}^{n-1} \;=\; 0\,.$$

We thus gained a set of linear equations. On the other hand, we introduced an error into the solution.

There is another method how to convert the non-linear set into a linear one. We could determine the u_{J-1}^n by one step of the Euler explicit method. In both cases, we could then use an iterative technique:

1. We solve the linear system (2.16). This results in a new value for u_{J-1}^n.
2. We plug this value into Eq. (2.17) instead of u_{J-1}^n and go back to step 1.
3. We repeat until the temperature on the surface u_J^n is sufficiently accurate (does not change substantially during iterations). We will use this temperature to solve the system (2.16).

The error significance We have shown in Pohl (2011) that this error is of the order of 10^{-2} K. Because the tests were performed only for a rotating asteroid in orbital configuration n1-s1 (see Fig. 2.4), we conducted a few tests to confirm the results for an arbitrary configuration. We did not observe any significant deviation from the mentioned order of error. And although this error increases as the time grid gets less dense, it remains small enough so that it can be neglected for the accuracy needs of TPM.

2.2.5 Grid spacing

Grid density In this subsection we are concerned with the effects of grid density on the error in temperature. The discretization errors of our numerical solver behave as $\mathcal{O}(\Delta t^2) + \mathcal{O}(\Delta x^2)$ as $(\Delta t \to 0, \Delta x \to 0)$ as we use the Crank-Nicholson FDM scheme.

Time grid Time grid density directly relates to the speed of our algorithm. If we add ten times more time grid points, we can expect the algorithm to be ten times slower. The accuracy of the solver depends on the time grid density which essentially translates to how finely we rotate the asteroid. As we are interested in both diurnal and seasonal temperature components, we should determine the grid density from the rotational period (and time step size Δt); diurnal component is a more detailed phenomenon. We are especially curious whether other parameters can either augment or reduce the error of a certain grid density.

[10] Difference of two identical periodic functions with a phase shift results in a periodic function.

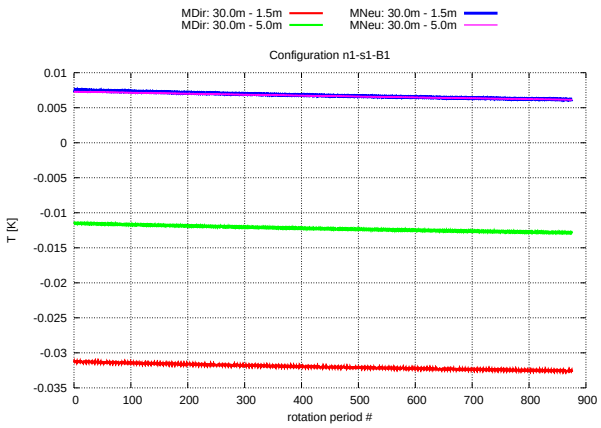

(a) Depth test for configuration n1-s1-B1

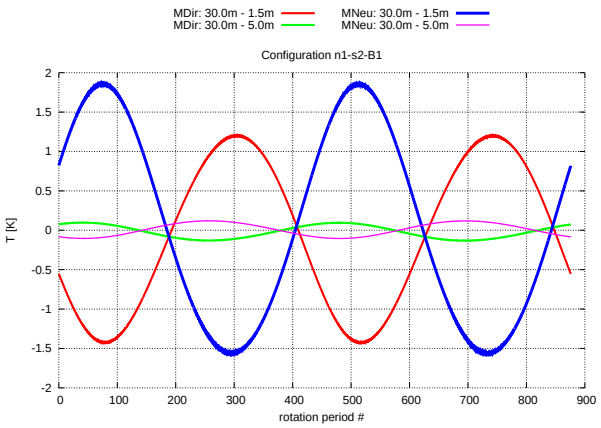

(b) Depth test for configuration n1-s2-B1

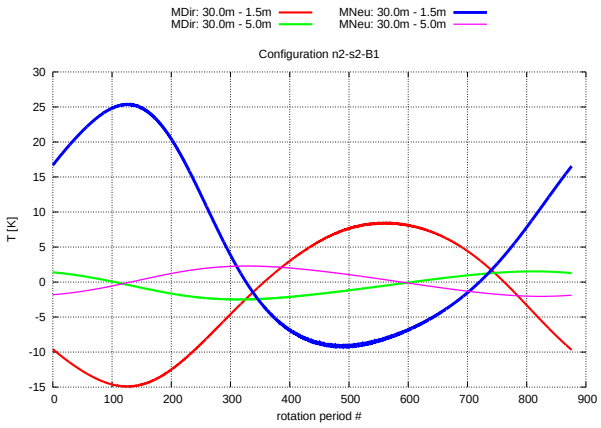

(c) Depth test for configuration n2-s2-B1

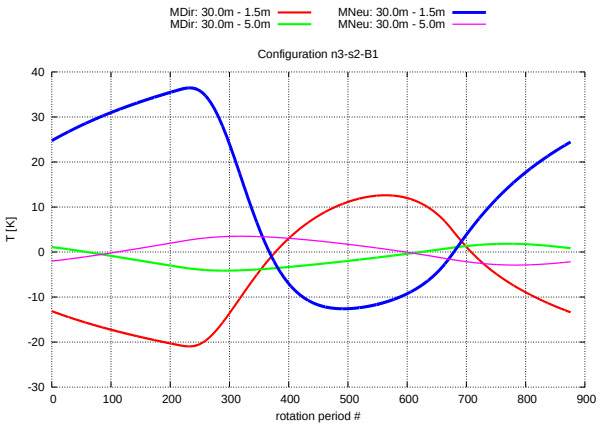

(d) Depth test for configuration n3-s2-B1

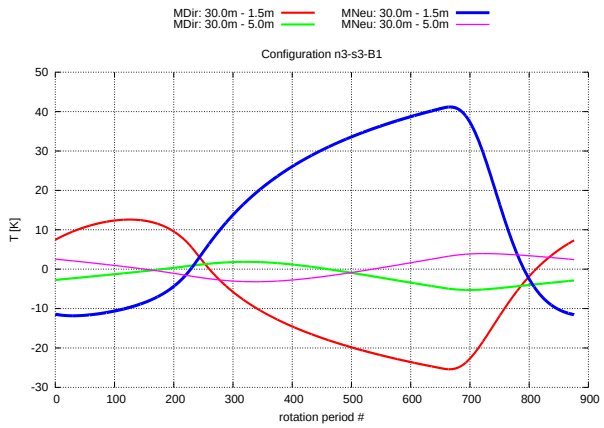

(e) Depth test for configuration n3-s3-B1

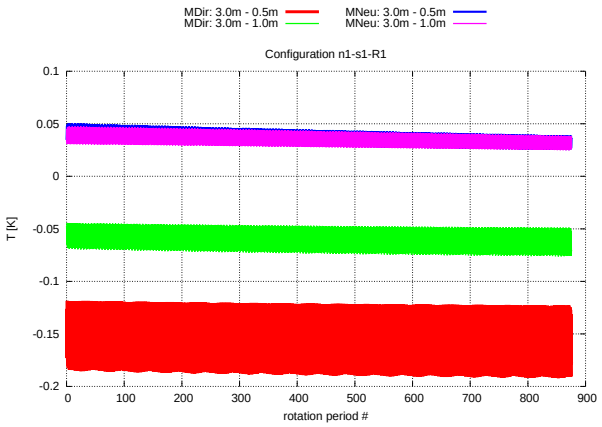

(f) Depth test for configuration n1-s1-R1

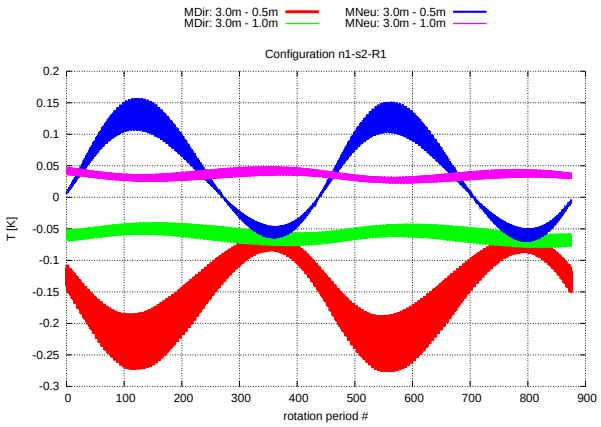

(g) Depth test for configuration n1-s2-R1

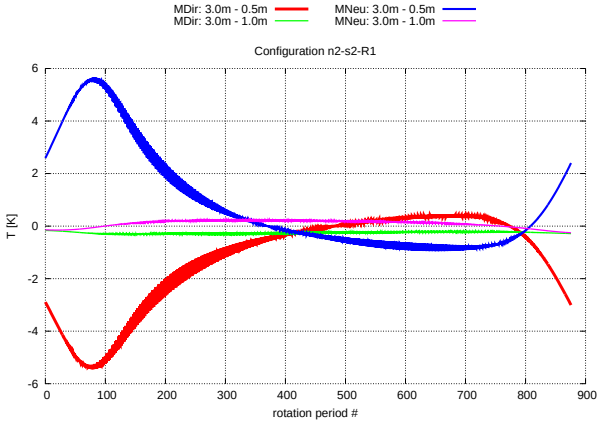

(h) Depth test for configuration n2-s2-R1

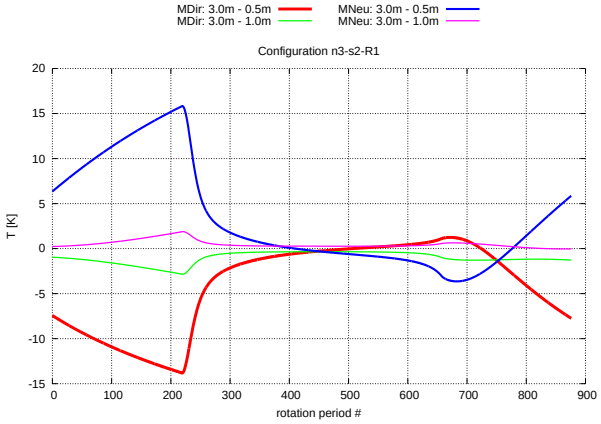

(i) Depth test for configuration n3-s2-R1

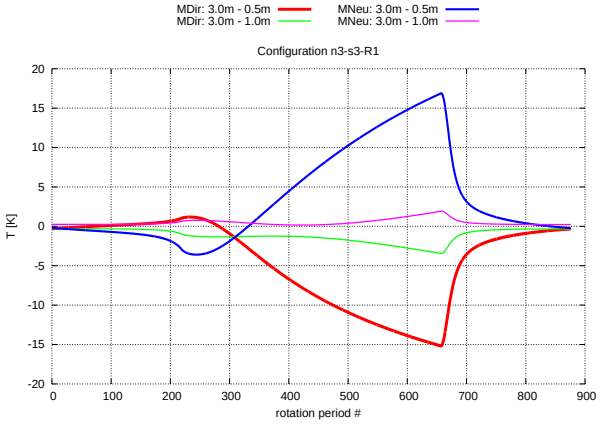

(j) Depth test for configuration n3-s3-R1

Figure 2.5: Test of temperature penetration depth. From several runs of the HCE solver, we concluded that for the given material and orbital configurations, the depths of calculation $x_{\max} = 30\,\mathrm{m}$ and $x_{\max} = 30\,\mathrm{m}$ are sufficient for basalt and regolith respectively, i.e. there is no significant temperature penetration deeper inside the asteroid. Therefore, we use the results with $x_{\max} = 30\,\mathrm{m}$ and $x_{\max} = 30\,\mathrm{m}$ as the reference (the most accurate temperature). We show the difference between this "accurate" surface temperature and the cases when $x_{\max} = 1.5\,\mathrm{m}$ and $x_{\max} = 5\,\mathrm{m}$. For the meaning of nx-sy see Fig. 2.4, B1 see Tab. 2.1, Mx and Rx see discussion about IC and BC above.

Space grid As far as space grid is concerned, the grid spacings of basalt and regolith cannot be compared directly . We could only compare the results for such spacings that produce equal number of grid points. Naturally, the number of grid points is tied to the integration depth (i.e. by choosing integration depth larger than necessary, we dilute the grid and vice versa) and thus a comparison based on the number of space grid point is not very useful.

The best measure for space grid comparison would be based on equal ratios of space step size to the characteristic penetration depth. However, the characteristic penetration depth is a tricky concept. Nevertheless, the only measure that is suitable and also available is to compare results that have the same fraction of grid spacing Δx to the skin depth l_{S}, defined in section 2.2.3. Unlike in the case of the integration depth, we should use the *skin depth determined from the rotational period*.

We should also note that unlike the time grid density, space grid density is not directly proportional to the speed of our algorithm; at least not in the sense that if we add ten times more space grid points, our algorithm will be ten times slower. The grid density is directly related to the size of the matrix Eq. (2.16) and the speed of solving the matrix is depends on the algorithm. E.g., the "famous" *tridag* procedure from Press et al. (1992) can only be characterized that its speed scales inversely as $\mathcal{O}(N)$. The Intel's MKL implementation of LAPACK procedure *?dtsvb* is of the same order, however, it is about 30% faster compared to the *tridag* algorithm.

Numerical results

Testing methodology We use the same orbital configurations as defined in section 2.2.1 — see Fig. 2.4. We conducted the tests for both basalt and regolith materials as defined in Tab 2.1. For initial and boundary condition we only used the type MDir, i.e. Dirichlet boundary conditions on both boundaries and initial condition determined from equilibrium temperature — see section 2.2.1. The grid spacings used in the tests are defined in Tab. 2.3. The data were obtained from the third orbital period and the maximum integration depths were 3 m and 30 m for basalt and regolith respectively. The reference grid spacing in comparisons was $\Delta t = 1\,\mathrm{s}$, $\Delta x = 0.004\,\mathrm{m}$ for basalt and $\Delta t = 1\,\mathrm{s}$, $\Delta x = 0.0006\,\mathrm{m}$ for regolith. The remaining parameters are identical to those defined in section 2.2.1.

Test results We present the results of the tests in Fig. 2.5. We note that the differences in temperatures were highly oscillating due to shifted peaks in temperatures. Therefore, we present the results in the form of envelope of the temperature differences. This envelope was produced by moving maxima. We present only selected results from all the tests with grids specified in Tab. 2.3 in order to illustrate space and time grid effects separately.

The most prominent feature of most of the results is that *less dense time grids* produce *larger errors in regolith materials*. When the time step is increased by an order of magnitude, the error in regolith is almost 8 times the error in basalt. This is true for all orbital configurations but n3-s2 and n3-s3 (see Fig. 2.4). We explain this effect by the lower thermal inertia of the regolith; lower thermal inertia implies faster material response to the insolation, and, during longer time interval we loose more significant temperature changes compared to basalt. However, this is mitigated if we consider surface element with very slow variation of insolation (i.e. with substantial seasonal effect and small diurnal effect) — this is the case of configurations n3-s2 and n3-s3.

Table 2.3: The grid spacing combinations used in testing. The columns $\Delta\chi_{\mathrm{rot}}$ and $\Delta\chi_{\mathrm{orb}}$ contain calculated ratio in per cent of the space grid spacing to the "rotational" and "orbital" skin depths for the respective *rotational* and *orbital* periods, i.e. $\frac{\Delta x}{l_{\mathrm{S,rot}}}$ and $\frac{\Delta x}{l_{\mathrm{S,orb}}}$. For the values of skin depth, consult Tab. 2.2.

Material	Δt [s]	Δx [m]	$\Delta\chi_{\mathrm{rot}}$ [%]	$\Delta\chi_{\mathrm{orb}}$ [%]	Material	Δt [s]	Δx [m]	$\Delta\chi_{\mathrm{rot}}$ [%]	$\Delta\chi_{\mathrm{orb}}$ [%]
Basalt	1	0.004	3.1	0.1	Regolith	1	0.0006	3.3	0.11
—	—	—	—	—	Regolith	1	0.001	5.4	0.18
Basalt	1	0.005	3.9	0.1	Regolith	1	0.005	27	0.92
Basalt	1	0.01	7.7	0.3	Regolith	1	0.01	54	1.8
Basalt	1	0.1	77	2.6	Regolith	1	0.1	550	18
Basalt	10	0.004	3.1	0.1	Regolith	10	0.0006	3.3	0.11
Basalt	10	0.01	7.7	0.3	Regolith	10	0.01	54	1.8
Basalt	10	0.1	77	2.6	Regolith	10	0.1	550	18
Basalt	100	0.004	3.1	0.1	Regolith	100	0.006	3.3	0.11
Basalt	100	0.01	7.7	0.3	Regolith	100	0.01	54	1.8
Basalt	100	0.1	77	2.6	Regolith	100	0.1	550	18

After a careful comparison of the results, we also determine that in the case of space grid, the regolith materials have larger errors. This can be seen if we compare data for Basalt and Regolith based on similar $\Delta\chi_{\mathrm{rot}}$ from Tab. 2.3. The reference grids $\Delta x_{\mathrm{basalt}}$ and $\Delta x_{\mathrm{regolith}}$ have a very similar grid spacing fraction of skin depth (about 3%). We can see that for basalt $\Delta x = 0.005$ equals about 4% of skin depth, smaller fraction than for regolith's $\Delta x = 0.001$ and basalt's $\Delta x = 0.01$ has larger fraction than regolith; we conclude that the spacing $\Delta x = 0.005$ for basalt should produce smaller errors than $\Delta x = 0.001$ for regolith and $\Delta x = 0.01$ for basalt should produce larger errors. However after careful examination of the data, we can see that in both cases basaltic material results in smaller errors. Although the difference of the errors is not as prominent as in the case of the time grids, we should be aware of this behaviour.

We can also see that the errors become more pronounced as the insolation increases — this is evident from the configurations n3-s2 and n3-s3, where the peaks coincide with larger insolation due to orbital motion.

We have also noticed that if we scale down the time grid size by an order of magnitude, the speed of the algorithm grows by order of magnitude. On the other hand, if we scale down the space grid size by an order of magnitude, the calculation speed also increases almost exactly by an order of magnitude. We have also noticed that the routine *?dtsvb* from Intel's MKL library is almost 30% faster than *tridag* from Press et al. (1992) (*?dtsvb* uses the fact that the matrix in Eq. (2.16) is diagonally dominant).

2.3 Propagation of the surface temperature errors into the total flux

The TPM inversion process minimizes the χ^2 as described in section 1.3:

$$\chi^2 = \sum_{i=1}^{N_{\mathrm{LC}}} \left[\frac{\Phi_i^{\mathrm{LC}} - f(\vec{\Sigma}, \vec{\Pi}, \vec{\Xi}, \vec{\Upsilon}, t_i)}{\sigma_i^{\mathrm{LC}}} \right]^2 + w^{\mathrm{IR}} \sum_{i=1}^{N_{\mathrm{IR}}} \left[\frac{\Phi_i^{\mathrm{IR}} - \tilde{F}(\vec{\Sigma}, \vec{\Pi}, \vec{\Xi}, \vec{\Upsilon}, t_i)}{\sigma_i^{\mathrm{IR}}} \right]^2 . \quad (1.4 \text{ rev})$$

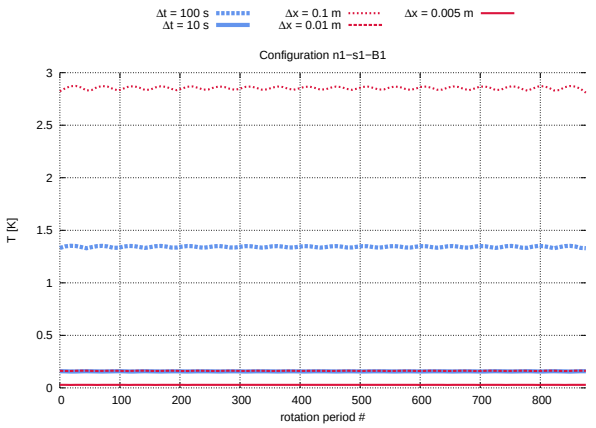

(a) Grid density test for configuration n1-s1-B1

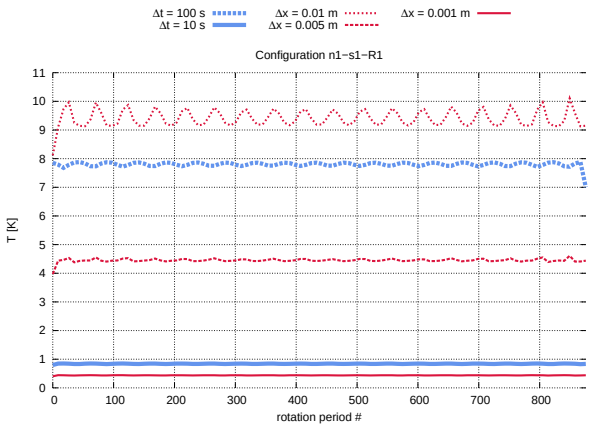

(b) Grid density test for configuration n1-s1-R1

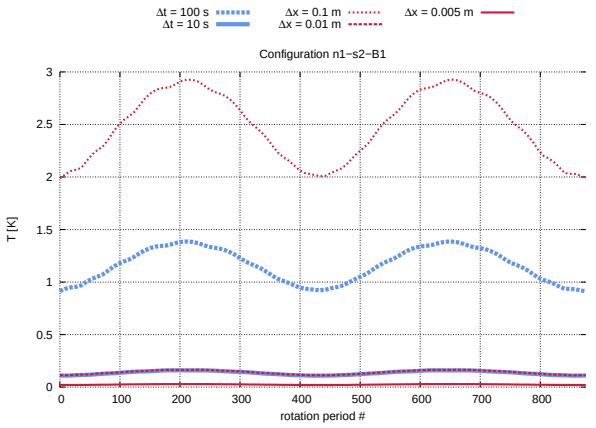

(c) Grid density test for configuration n1-s2-B1

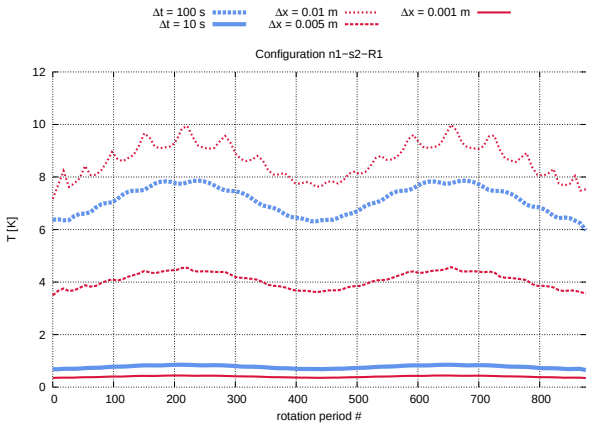

(d) Grid density test for configuration n1-s2-R1

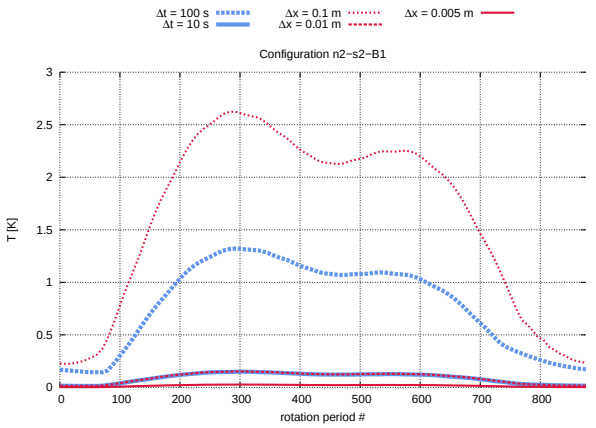

(e) Grid density test for configuration n2-s2-B1

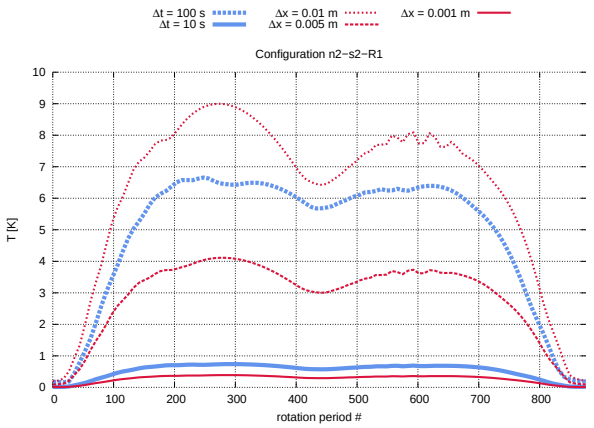

(f) Grid density test for configuration n2-s2-R1

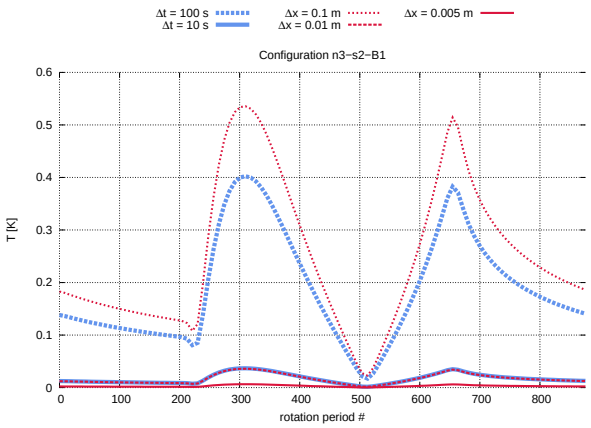

(g) Grid density test for configuration n3-s2-B1

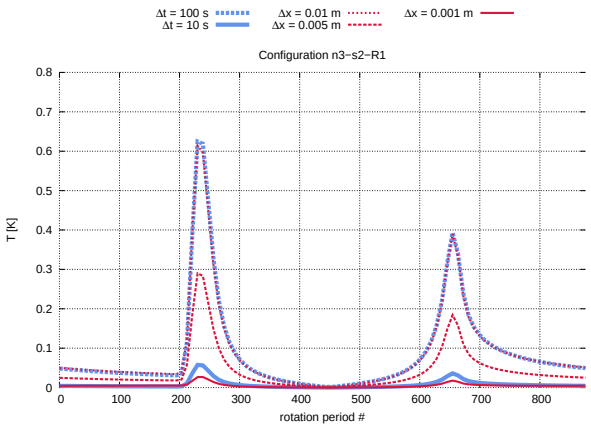

(h) Grid density test for configuration n3-s2-R1

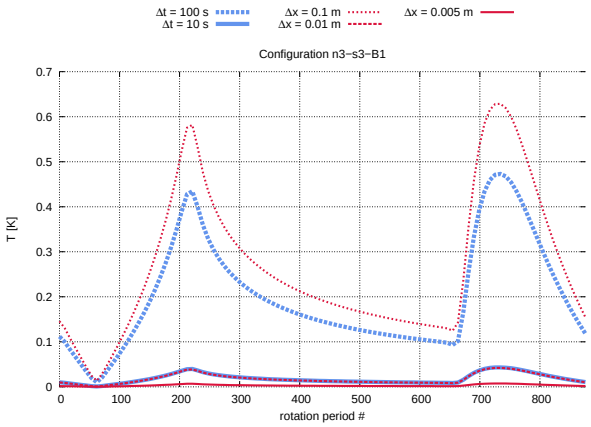

(i) Grid density test for configuration n3-s3-B1

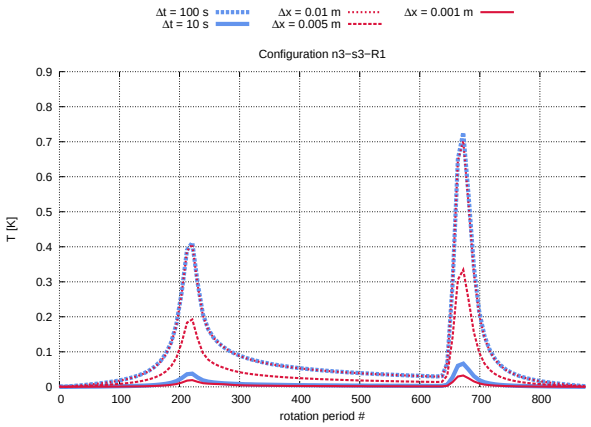

(j) Grid density test for configuration n3-s3-R1

Figure 2.5: Test of grid density. Each panel shows the difference between reference surface temperature and surface temperatures determined with grid less dense grids. The legend informs how is the grid different (i.e. $\Delta x = 0.01\,\mathrm{m}$ in the legend means that the space grid has changed from the reference value to 0.01 m and the time grid remained the same). Because the temperature differences are extremely oscillating, we present their moving maxima 5 steps ahead and 5 steps behind.

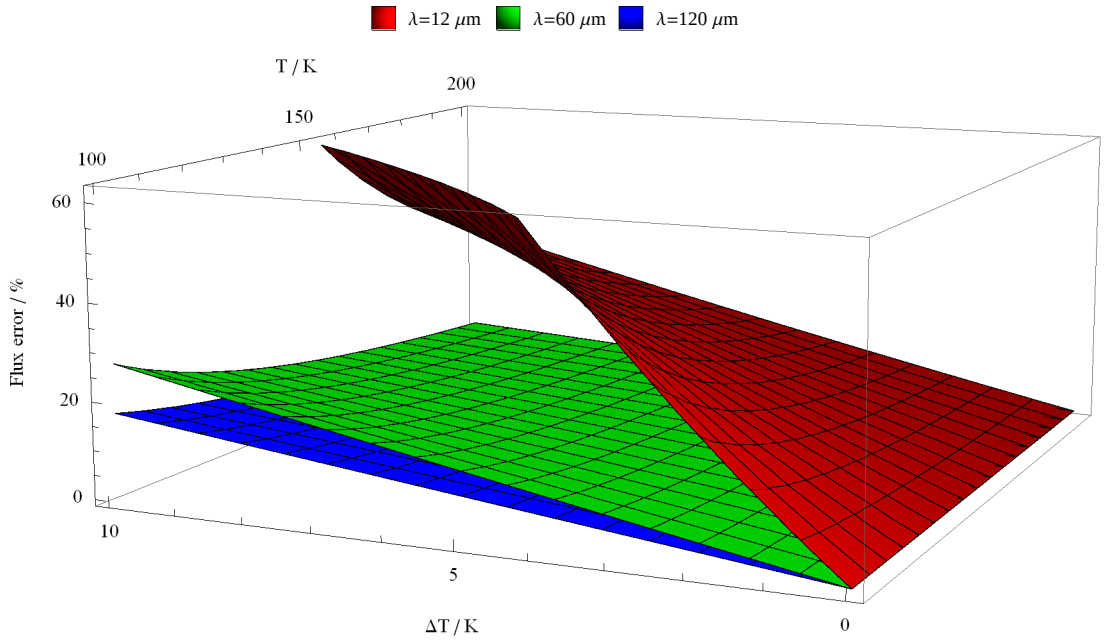

Figure 2.6: Single facet flux error determined from the Planck's law.

The errors of the modelled flux ($y^{\mathrm{IR}}(\vec{x_{ij}}|\,\vec{a})$) should *not* be larger than those ($\sigma_{ij}^{\mathrm{IR}}$) of the observed flux ($y_{ij}^{\mathrm{LC}}$). Therefore, it is necessary to be able to predict how the errors in the surface temperature spread into the modelled (total) flux. However, because the total flux is an integrate value which depends not only on the surface temperature but also on the orbital configuration (including observer's position), surface roughness and the surface scattering model, it is impossible to find an analytical expression (even if approximate) for the total flux error. We are thus left with numerical testing.

This section presents several tests performed to determine the spread of the surface temperature error. In the first subsection, we present a simple model of temperature error propagation into the flux error from a single facet. We follow with the tests that determine how the surface temperature error influences the total flux error.

2.3.1 Single facet flux error

We can determine the flux error from a single facet using the Planck's formula (1.3):

$$\begin{aligned} F(\lambda,T)\big|_{\mathrm{Jy}} &= 10^{20}\times\frac{1}{c}\lambda^2\cdot\frac{2hc^2}{\lambda^5}\frac{1}{\mathrm{e}^{\frac{hc}{\lambda k_{\mathrm{B}}T}}-1}\bigg|_{\frac{\mathrm{W}}{\mu\mathrm{m}\cdot\mathrm{sr}}}, \\ &= 10^{20}\times\frac{2hc}{\lambda^3}\frac{1}{\mathrm{e}^{\frac{hc}{\lambda k_{\mathrm{B}}T}}-1}\bigg|_{\frac{\mathrm{W}}{\mu\mathrm{m}\cdot\mathrm{sr}}}. \end{aligned} \qquad \text{(1.3 rev)}$$

Fig. 2.6 presents the flux error in per cents as a function of the temperature T at which we determine the flux, the error of the of the surface temperature ΔT and the observed wavelength of the flux.

We can see that the error has a very strong dependence on the observed wavelength. Also, for smaller temperatures the flux error is higher given the same wavelength and temperature error.

Although the error for single facet cannot give us the necessary temperature accuracy, it can illustrate the order of magnitude relation between the temperature and flux errors. We also present selected data from Fig. 2.6 in Tab. 2.4.

Table 2.4: Flux error from a single facet as a function of wavelength λ, surface temperature T, surface temperature error ΔT displayed in per cents.

λ [μm]	ΔT [K]	T [K]	flux Error [%]	λ [μm]	ΔT [K]	T [K]	flux Error [%]	λ [μm]	ΔT [K]	T [K]	flux Error [%]
12	1	100	12.6	60	1	100	2.65	120	1	100	1.72
12	1	150	5.44	60	1	150	1.34	120	1	150	0.97
12	1	200	3.04	60	1	200	0.86	120	1	200	0.66
12	5	100	77.0	60	5	100	13.5	120	5	100	8.63
12	5	150	29.4	60	5	150	6.72	120	5	150	4.85
12	5	200	15.8	60	5	200	4.30	120	5	200	3.33
12	10	100	197	60	10	100	27.5	120	10	100	17.4
12	10	150	64.8	60	10	150	13.5	120	10	150	9.71
12	10	200	33.2	60	10	200	8.63	120	10	200	6.66

2.3.2 Total flux error

Required precision

Observation errors As we have mentioned earlier, the accuracy needs for the modelled flux are determined by the error of the observed flux in Eq. (1.4). The error in the measured flux can be as small as 3% and as high as 30%. From Tab. 2.4 we can guess the lower boundary for temperature error should be about one or two Kelvins. In the view of the error analysis in the previous sections of this chapter, this requirement is rather strict. On the other hand, temperature is not the only source of error in the modelled flux.

Non-Lambertian surface Typical asteroid surface is rough and, unlike on Lambertian surfaces, several important effects arise. Due to porosity it is necessary to take into account multiple scattering, shadows, mutual heating. Unfortunately, these effect are not negligible (Lagerros, 1998). The TPM algorithm introduces surface roughness by means of craters. The implemented model is rather crude and therefore introduces inaccuracy into the total flux. The magnitude of the inaccuracy is difficult to estimate, however, we tried this in one of the tests presented later. This uncertainty makes the accuracy requirement for the temperature mentioned in the previous paragraph less strict.

Other factors The error in the total flux due to the surface temperature inaccuracy may be amplified by the magnitude of TPM solver parameters (λ, β, thermal inertia, etc.). We conducted several tests to uncover this relation and the results are presented later in the section.

The effect of temperature errors

In this part we examine the effect of a temperature error on the error of total flux.

Testing methodology For all tests in this section we use the TPM solver with implementation described in section 1.3. Accordingly, we had to use a real asteroid for which there are all the necessary data available. We chose asteroid 306 Unitas. We obtained

the input parameters from the DAMIT database[11] and infrared observations obtained by the Infrared Astronomical Satellite (IRAS). We let the solver enter the first Levenberg-Marquardt (L-M) iteration. When TPM calculated the modelled flux from Eq. (1.4), we stopped the code and saved the calculated flux values. Next, we introduced temperature error and reran the first L-M iteration. We introduced the error by increasing the temperature of each facet by 1%, 5% and 10%. We also considered other methods of introducing artificial error (e.g. using a distribution function) but we concluded that with any other method we would loose the control over the temperature error to some degree. The selected method has the advantage that it gives an upper limit of the flux error. We then calculated the percentage change in flux for a given percentage increase in temperature.

Test results We present the test results in Tab. 2.5. First, we note very good resemblance with errors determined for a single facet in Tab. 2.4. Second, because the temperature on the surface of the Unitas asteroid ranges approximately between 80 K and 220 K, 1% error in the temperature corresponds to Kelvin values between ~ 1 K and ~ 2 K. This has a profound impact on the necessary accuracy of the surface temperature determined by TPM.

If our data are quite inaccurate, we can do with 5% temperature error (between ~ 5 K and ~ 10 K). However, if our observation precision is around 10%, the temperature errors should be at most 2%. If we are fortunate and have all the measurements in longer wavelengths, we can allow ourselves larger errors in the temperature. On the other hand, if the asteroid's temperatures are lower, we can expect (based on the single facet flux error) more strict upper boundary on the surface temperature error.

Table 2.5: Total flux error in per cent (ΔF) as a function of temperature error (ΔT). For each wavelength we show the average error from all time instants when the modelled flux was calculated. However, the flux error rounded to the tenths of percents was identical in all those time instants and thus we did not loose any essential information by the averaging process.

$\lambda\,[\mu\mathrm{m}]$	$\Delta F\vert_{\Delta T=1\%}$	$\Delta F\vert_{\Delta T=5\%}$	$\Delta F\vert_{\Delta T=10\%}$
11,1	8	44	101
12,0	7	37	82
22,6	5	25	53
25,0	4	21	44
60,0	2	13	26
100,0	2	10	20

Effect of input parameters on total flux error

The results presented in the previous section were calculated with a given input parameters of the model. To clarify whether and how the change in those parameters affects the error in total flux, we conducted a series of further numerical tests.

Testing methodology We used similar approach as in the previous subsection on the effect of temperature errors. We ran the solver without temperature errors, then with

[11] This database is available at http://astro.troja.mff.cuni.cz/projects/asteroids3D/web.php.

temperature errors (1% and 5%)[12]. Next we changed an input parameter and repeated the procedure. We then calculated the percentage change in flux for a given percentage increase in temperature for a given set of parameters. The input parameters that we tested were: λ, thermal inertia, asteroid size, period and surface roughness parameters (see Tab. 1.1).

Test results

Thermal inertia The results of the effect of thermal inertia on the propagation of the temperature errors are summarized in Tab. 2.6. We can conclude that the thermal inertia's effect on the error propagation is negligible. This is especially true with respect to the profound effect on different wavelengths.

Table 2.6: Effect of thermal inertia on the propagation of temperature errors into the total flux. λ is the wavelength of the observed flux in μm, Γ is the thermal inertia in $\mathrm{J \cdot m^{-2} \cdot K^{-1} \cdot s^{-1/2}}$ and ΔT is the introduced temperature error. The values of total flux error are in per cent and are averaged over all observed time instants.

$\downarrow \lambda \Big\vert \underrightarrow{I}$	$\Delta T = 1\%$				$\Delta T = 5\%$			
	10	40	100	200	10	40	100	200
11.1	7.6	7.9	8.2	8.5	42.4	43.9	46.3	48.4
12.0	6.6	6.8	7.0	7.1	36.1	37.0	38.2	39.2
22.6	4.6	4.8	4.9	5.0	24.2	25.0	26.0	26.5
25.0	4.1	4.1	4.1	4.1	21.1	21.2	21.4	21.5
60.0	2.5	2.5	2.5	2.5	12.8	12.6	12.6	12.7
100.0	2.0	2.0	2.0	2.0	10.2	10.1	10.1	10.1

Rotational period The results of the effect of period in the propagation of the temperature errors are summarized in Tab. 2.7. We can conclude that the effect of different period on the error propagation is also negligible. This is especially true with respect to the profound effect on different wavelengths.

Table 2.7: Effect of period on the propagation of temperature errors into the total flux. λ is the wavelength of the observed flux in μm, P is the rotational period in hours and ΔT is the introduced temperature error. The values of total flux error are in per cent and are averaged over all observed time instants.

$\downarrow \lambda \Big\vert \underrightarrow{P}$	$\Delta T = 1\%$				$\Delta T = 5\%$			
	6	9,4	12	15	6	9,4	12	15
11.1	7.9	7.9	7.8	7.7	44.4	43.9	43.7	43.4
12.0	6.8	6.8	6.7	6.7	37.3	37.0	36.9	36.7
22.6	4.8	4.8	4.7	4.7	25.2	25.0	24.9	24.8
25.0	4.1	4.1	4.1	4.0	21.3	21.2	21.2	21.1
60.0	2.5	2.5	2.5	2.4	12.6	12.6	12.6	12.6
100.0	2.0	2.0	2.0	1.9	10.0	10.1	10.0	10.0

[12]Based on the results in Tab. 2.5, we did not introduce the 10% temperature error as such an error results in too big total flux errors.

Surface roughness The results of the effect of surface roughness in the propagation of the temperature errors are summarized in Tabs. 2.8 and 2.9. The first table summarizes the effect of the parameter that controls the density of craters (which model the roughness of the surface) on the surface, we denote it CC as in Cratering Coverage. Unlike the above parameters, cratering coverage effect in error propagation is not negligible, unless very small temperature errors are preserved (2 K at most). The effect of the parameter that controls the size of the craters is summarized in Tab. 2.9. We denote this parameter CA as in Crater Aperture. We can see that this parameter, has negligible effect in temperature error propagation.

Table 2.8: Effect of cratering coverage on the propagation of temperature errors into the total flux. λ is the wavelength of the observed flux in μm, CC is the crater coverage parameter and ΔT is the introduced temperature error. The values of total flux error are in per cent are averaged over all observed time instants.

$\downarrow \lambda \Big\vert \underrightarrow{CC}$	$\Delta T = 1\%$				$\Delta T = 5\%$			
	0	0,1	0,4	0,8	0	0,1	0,4	0,8
11.1	6.1	6.2	6.7	7.9	33.0	33.7	36.4	43.9
12.0	5.1	5.2	5.6	6.8	26.8	27.4	29.9	37.0
22.6	3.2	3.3	3.7	4.8	16.4	16.9	19.0	25.0
25.0	2.7	2.8	3.1	4.1	13.7	14.1	15.9	21.2
60.0	1.6	1.7	1.9	2.5	8.1	8.3	9.3	12.6
100.0	1.4	1.4	1.5	2.0	6.7	6.9	7.6	10.1

Table 2.9: Effect of cratering aperture on the propagation of temperature errors into the total flux. λ is the wavelength of the observed flux in μm, CA is the crater aperture parameter in degrees and ΔT is the introduced temperature error. The values of total flux error are in per cent are averaged over all observed time instants.

$\downarrow \lambda \Big\vert \underrightarrow{CA}$	$\Delta T = 1\%$				$\Delta T = 5\%$			
	5	30	60	90	5	30	60	90
11,1	7,9	7,9	7,9	7,8	43,9	43,9	43,9	43,3
12,0	6,8	6,8	6,8	6,7	37,0	37,0	37,0	36,6
22,6	4,8	4,8	4,7	4,7	25,1	25,1	25,0	24,7
25,0	4,1	4,1	4,1	4,0	21,2	21,2	21,2	21,0
60,0	2,5	2,5	2,5	2,5	12,6	12,6	12,6	12,5
100,0	2,0	2,0	2,0	2,0	10,1	10,1	10,1	10,0

Other parameters Other parameters (λ, β, asteroid size) have either negligible or no effect on the temperature error propagation.

2.3.3 Conclusion

The main purpose of this section was to determine the goal accuracy of the HCE solver implemented in TPM. The needed surface temperature precision is determined by the IR observation data; we need the modelled flux to have a comparable error with the observations. In the first part we showed that analytically determined flux error from a

single facet can be a good guideline of how precise we need the solution to be (given the error of observations), especially if we know the range of temperatures on the asteroid. In the second part, we determined the error of total flux provided a certain temperature error had been introduced. We have seen that the error is strongly determined by the observed wavelength.

For wavelengths ranging from 11 μm to about 100 μm observed on a regolith asteroid (such as Unitas), we can conclude that in order to keep the errors of the modelled flux similar to "typical" observational errors of the IRAS (i.e. between 10%–30%), we need to keep the temperature errors well below 5 K, preferably even below 2 K. Furthermore, if we want to use data from Wide-field Infrared Survey Explorer (WISE) which attains errors of $\sim 1\%$, we have to achieve the temperature errors of the order of tenths of Kelvin at most.

In the last part of the section, we showed that only cratering parameters can amplify the propagation of temperature errors into the total flux. This is especially true when the temperature errors are larger than ~ 2 K. Therefore, when dealing with cratering parameter greater than ~ 0.5, it is necessary to keep the temperature errors low (i.e. in the above mentioned configuration — ~ 1 K).

2.4 Recommendations and Conclusion

We started this chapter by describing the current implementation of the Heat Conduction Equation (HCE) solver in the TPM. We followed by a general error analysis of a one dimensional numerical solution of HCE. We identified several areas that contribute to the total error of the numerical solution. In the third section, we focused on the propagation of error of the surface temperature to the total infrared (IR) flux which is the ultimate quantity used in the Levenberg-Marquardt (L-M) loop. The goal of this section is to synthesize the information presented in this chapter. We will go through the areas mentioned in the second section, discuss them in the context of current implementation in TPM and provide recommendations for further code improvement with respect to the necessary accuracy of the modelled flux as well as to the computational efficiency.

2.4.1 Temperature relaxation

Current implementation TPM addresses the relaxation problem by integrating a lot of rotational periods. In the case of asteroid Unitas, TPM is supplied with ephemeris data that lead to integration of about 150 rotational periods. However, the system is never integrated over several orbital periods to achieve full relaxation. Although this approach may achieve relaxation for some orbital configurations (e.g. n1-s1, n1-s2 — see Fig. 2.4), it is not sufficient for others (e.g. n3-s2 — see Figs. 2.5g and 2.5h) if we want to achieve the target total flux error of about 10%.

Recommendation In order to achieve maximum accuracy, it is necessary to integrate at least one full orbital period to be able to describe the seasonal component of temperature profile within the asteroid. However, this approach is very demanding on computational resources because such integration would have to be done for every facet of the asteroid and in every L-M loop. In view of this we suggest the following integration schemes.

1. We start integration with a coarse time step and integrate the problem for two orbital periods, preferably in such a way that during the second orbital period we

integrate at time instants that are between time instants from the first period — see Fig. 2.7a.

2. We stop the "coarse" integration after two orbital periods, about ten rotational periods before the time when we need to have the system relaxed.

3. From this time we start integration with a fine time step.

The size of the coarse step is strongly dependent on the orbital configuration and the configuration should be taken into account. Therefore, we suggest different coarse steps based on the angle between the asteroid's axis and the orbital plane. The cases with axis almost perpendicular to the plane will be given the coarsest time step of the order $\sim 10^{-4}$ of the orbital period. The cases close to the configuration s3 will be given time step of the order $\sim 10^{-5}$ the orbital period.

The coarse integration will provide the seasonal temperature profile which the current implementation misses. The computational efficiency may even improve too as we have over one order of magnitude less fine integrations.We also propose a more sophisticated version of the above:

1. We start with the coarse time step as above (Δt_{C}).

2. After each coarse time step, we integrate one or two rotational periods with finer time step (Δt_{F}) — this will be thus several integration steps.

3. Once we complete one rotation, we do another coarse time step and so on.

4. We stop this after one or two orbital periods about 10 rotational periods before the time when we need to have the system relaxed.

5. From this time we start integration with a fine time step $\mathrm{d}t$[13]. The process is illustrated Fig. 2.7b

In this case, the coarse time step can be approximately order of magnitude smaller than in the first approach. On the other hand the finer time step Δt_{F} should be about one percent of the rotational period. This approach will be more accurate, on the other hand, it will be slower than the first approach.

2.4.2 Initial temperature

Current implementation TPM assigns specified temperature (usually 100 K) throughout the whole asteroid as the initial condition (IC). In Figs. 2.5a – 2.5j we have noticed that given this initial condition, the system takes very long to relax even in the simple orbital configuration n1-s1. In section 2.2.2 we focused solely on this initial condition; we concluded that the "wrong" choice of initial condition leads to rather large temperature errors. Even though the solution should eventually converge to the correct one regardless of the initial temperature, it is undesirable to wait so long.

Recommendation A good choice for IC is the equilibrium temperature determined from the average insolation.

One way to calculate such a temperature is to determine an average insolation incident on each facet and then calculate the temperature from $T_{\mathrm{eq}} = \sqrt[4]{\langle \varepsilon_{\mathrm{S}} \rangle \frac{1-\mathrm{A}}{\eta\sigma}}$, where $\langle \varepsilon_{\mathrm{S}} \rangle$ is

[13]Note that $\Delta t_{\mathrm{C}} > \Delta t_{\mathrm{C}} > \mathrm{d}t$.

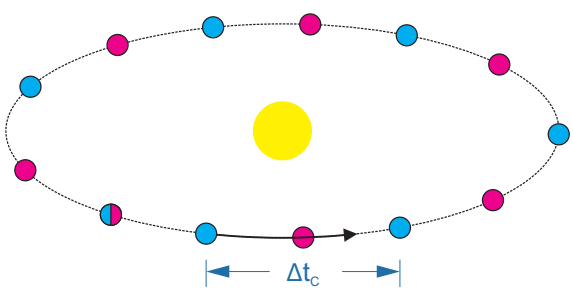

(a) Relaxation method with only coarse time step Δt_C. Steps in the first and second periods are printed with different colour.

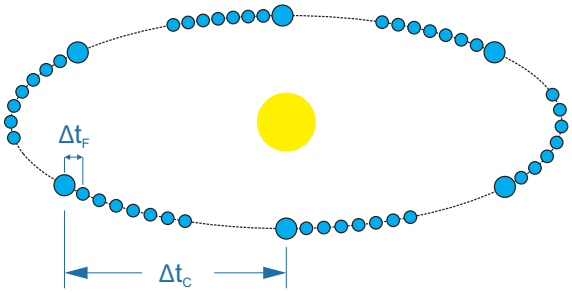

(b) Combined relaxation method with coarse and fine time steps (Δt_C and Δt_F). Only first orbital period shown.

Figure 2.7: Illustration of suggested steps necessary for proper temperature relaxation. Blue dots suggest steps during the first period, red dots suggest steps in the second period, Δt_C and Δt_F are the coarse and fine time steps respectively.

the average insolation incident on the slab during one orbit. This has two drawbacks — each facet will have a different equilibrium temperature; also, the facets with normals perpendicular to the direction to the sun will have equilibrium temperature zero. On the other hand, as we only consider radial heat transfer, there is no heat exchange between the slabs and thus no mechanism to equalize the temperature, thus this is a natural consequence of our one dimensional simplification.

Yet, another method that could be used is to calculate the total flux received by the asteroid during one orbit and use this quantity to determine the equilibrium temperature. In this case, this temperature would be the same for all slabs. However, there would be only few slabs for which this temperature would be a characteristic one. For most slabs this would result in an incorrect characteristic temperature — the situation analogous to the current implementation. On the other hand, this solution improves the one dimensional approximation by including an effect typical for the 3D problem.

We suggest using the former method in which each slab has a different equilibrium temperature mostly because this method has been extensively tested. However, implementation of the latter is an interesting topic for future work. This improvement will, slow down the computation process. But, compared with solving the matrix problem Eq. (2.16) in each time step during the relaxation and the computation itself, this is a negligible delay.

2.4.3 Integration depth

Current implementation TPM uses dimensionless space coordinate units introduced in Eq. (2.12)–(2.15). One advantage of such solution is that the maximum depth can be specified as a multiple of the skin depth which automatically adjusted based on the asteroid material.

However, there are two major problems with such implementation. First the whole concept of skin depth is derived from the simplified 1D steady state analytical solution of an asteroid in orbital configuration n1-s1 with only rotational motion. As we illustrated in section 2.2.3, skin depth determined from this model is useless for our situation (for orbital configuration n2-s2 with rotational period of 10 hours, the real penetration depth is about 200 times larger than the skin depth — see Tab. 2.2 and Fig. 2.5). TPM currently implements maximum integration depth as *eight times the skin depth* based on rotational period. The errors of incorrect integration depth car go as high as 40 K — see Fig. 2.5.

Recommendation In Tab. 2.2 we also illustrated how the skin depth would change if we used orbital period instead of the rotational period. This penetration depth can be used for the orbital configuration n1-s1 if the asteroid undergoes orbital motion without rotation. However, we suggest multiplying this "orbital" skin depth by a sufficiently large factor (e.g. 10) and use this number as a maximum integration depth. This solution, however, does not guarantee sufficient integration depth. This system would also tend to integrate unnecessarily deep for certain slabs, making the process less efficient.

Another solution would be to select maximum integration depth based on thermal inertia value, surface normal and orbital period. This would require precomputed penetration depths.

We recommend employing the former solution as it is the easiest to implement. If this was accompanied by implementation of non-equidistant space grid (see later), the inefficiency might be somewhat mitigated.

2.4.4 Internal boundary condition

Current implementation TPM currently uses Neumann internal boundary condition. As we have illustrated in the previous discussion, this condition gives slightly larger errors if insufficient integration depth is selected.

Recommendation Despite the fact that Neumann's boundary condition is used most often for 1D numerical solution of HCE in asteroids, we prefer the Dirichlet condition based on equilibrium temperature determined from average insolation incident during one orbital period on each facet (see discussion in section 2.4.2).

2.4.5 Grid spacing

Current implementation TPM currently employs equidistant space grid equal to one fourth of skin depth (i.e. $\Delta\chi = 0.25 l_\mathrm{s}$, where l_s is the skin depth based on rotational period) and it employs non-equidistant time step that automatically scales down the time step if the surface temperature gradient becomes too large.

Recommendation

Time grid As we have seen in section 2.2.5, too large time steps (i.e. too small time grid density) result in very large errors up to ten Kelvins. These errors are strongly dependent of the material of the asteroid. These properties make the current implementation of non-equidistant grid rather problematic. The time step size should be determined by the rotational period and material properties rather than by the size of subsurface temperature gradient.

Therefore, we see as necessary to implement equidistant time grid with time step determined from the rotational period.

Moreover, we suggest $\Delta t = f(P, \Gamma) = a \cdot P + g(\Gamma)$, i.e. the time step should be linearly proportional to the rotational period P and also directly proportional to the thermal inertia Γ. The determination of the relation $g(\Gamma)$ and whether it is even feasible to find such a relation is up to further numerical experiments. We suggest the following procedure to determine the relation:

1. Produce a large number of error data (i.e. the difference between surface temperature with fine time step and coarse time step, probably with ratio of two orders of magnitude) for various thermal inertia values.

2. Fit the data.

3. If the fit is successful, go to first step and use different coarse step (probably one order of magnitude ratio with respect to the fine step) and determine whether the functional relationship works to a reasonable degree.

Space grid As we have shown in sections 2.2.3 and 2.2.5, skin depth based on orbital period is the only reasonable measure on which we can base the integration depth; at the same time, skin depth based on rotational period is a reasonable measure on which we should base our space grid spacing. However, implementing both of these measures results in a rather large space grid.

From the tests that we have performed, it is quite clear that the temperature changes less sharply the deeper we descend inside the asteroid. Consequently, the grid deep inside the asteroid is unnecessarily dense. Therefore, we recommend implementing non-equidistant space grid. Based on the results of the one dimensional analytical solution presented in App. C, where the temperature changes from a certain equilibrium temperature die out exponentially, we suggest exponential scaling of the space grid, i.e. $\Delta x_i = \Delta x_0 \mathrm{e}^{a(i,J)i}$, where i is the current grid point and $a(i, J)$ is a function of the total number of the space grid points (J) such that $x_{\max} = \sum_{i=0}^{J} \Delta x_0 \mathrm{e}^{a(i,J)i}$ or a power law scaling. In any case, such space grid must be dense beneath the surface and more sparse toward the "center" of the asteroid. Such grid would make it possible for a less dense grid on average while preserving a similar accuracy. It would also obviate the need for non-equidistant time grid to describe the gradients beneath the surface.

2.5 Conclusion

Our aim in this chapter was to provide the necessary information about accuracy and feasibility of a one dimensional Heat Conduction Equation (HCE) solver for its implementation in the TPM inversion solver. In the first part of the chapter, we described its current implementation in the TPM. Next, we analyzed its accuracy and described how the error was spread into the infrared flux from the asteroid. In the last section we provided recommendations for further implementation in the solver, in order to address the accuracy issues. We admit that the errors of infrared flux presented in the Sec. 2.3 (both the error from a single facet as well as the error determined from the TPM) provide only a rough approximation and determine the maximum flux error based on some maximum temperature error.

Observations From the tests that we have performed, we conclude:

1. The magnitude of temperature error is strongly correlated with both the orbital configuration and the facet for which we determine the temperature (i.e. the surface normal).

2. The numerical solution that is not relaxed, generates errors as high as 30%.

3. The relaxation is faster for regolith materials.

4. Improper setting of initial condition results in a very slow relaxation and errors in the unrelaxed stage can surpass 30%.

5. The errors due to insufficient integration depth can surpass 40%.

6. Roughest space and time grids that we tested cause errors of the order $\sim 8\%$, usually less.

7. Basaltic materials usually have larger errors in the numerical solution.

8. The total flux error is strongly dependent on the observed wavelength, the lower the wavelength, the more pronounced a fixed temperature error is in the total flux.

9. For typical errors in infrared observations obtained by the IRAS satellite ($\sim 10\%$), we need the temperature precision of about 1%.

These issues should be addressed in order to obtain sufficiently quality thermal model for use in the TPM inversion solver. We have provided several suggestions regarding the implementation.

Because the numerical tests revealed that certain surface facets (in a given orbital configuration) are associated with larger temperature errors, we propose the following hypothesis: the contribution to the total flux from the facets with large associated temperature errors is small compared with the facets with small temperature errors; this, in effect, reduces the error of the total flux caused by the error in the temperature.

To test this, we used the temperature obtained from the relaxation tests and from the integration depth test. We calculated the flux at wavelength $\lambda = 12\,\mu$m from the facet associated with each orbital configuration (see Fig. 2.4) using the Planck law in the Jansky unit (Eq. (1.3)) and projected it to the direction of the observer (i.e. multiplied the flux by the cosine of the angle between the observer and the surface normal). For simplicity, we assumed that the observer is in the same direction as the Sun. Then, we computed absolute value of the difference between a reference flux (determined from the most accurate surface temperature, e.g. from the temperature in the relaxed state, with sufficient integration depth and sufficiently dense grids) and flux determined from the temperature which we considered incorrect, e.g. determined in an unrelaxed state. We present the results in Figs. 2.8 and 2.9.

The first series in Fig. 2.8 depicts the projected single facet flux error caused by the temperature relaxation error between the first and third orbital periods illustrated (the plot "OP3-OP1") in Fig. 2.4. Fig. 2.9 presents projected single facet flux error caused by insufficient integration depth illustrated in Fig. 2.5. In order to estimate the significance of the error, Tab. presents maximum flux values in the reference configuration

We note several features. First, the relaxation error in the initial stages of integration results in huge flux errors (note that we broke the graph apart at 10 Jy and continued at 350 Jy). However, the magnitude decreases quickly due to diurnal component relaxation, the seasonal component relaxation takes longer but as the time progresses the error reaches zero (if we plotted the error in the second orbital period as well we could see errors in all orbital configuration to converge to zero). On the other hand, the error due to insufficient integration depth is omnipresent.

We can also observe strong oscillations in the flux error in certain orbital configurations. They are caused partly by the temperature error oscillation as seen in Fig. 2.4. These oscillation in temperature are visible in configurations where the seasonal component of temperature is small compared to the diurnal component. The amplitude of these oscillations is then augmented by the projection of the flux.

From the presented figures, we can for example conclude that in the case of configuration n2-s2 where the errors for insufficient integration depth are quite pronounced, the error in the flux is negligible. We can see from the Fig. 2.4 that angle between the normal n2 and the direction to the Sun is almost all the time very close to $\pi/2$ and thus the projection of the flux is ~ 0. On the other hand, we also see that in the case of facet

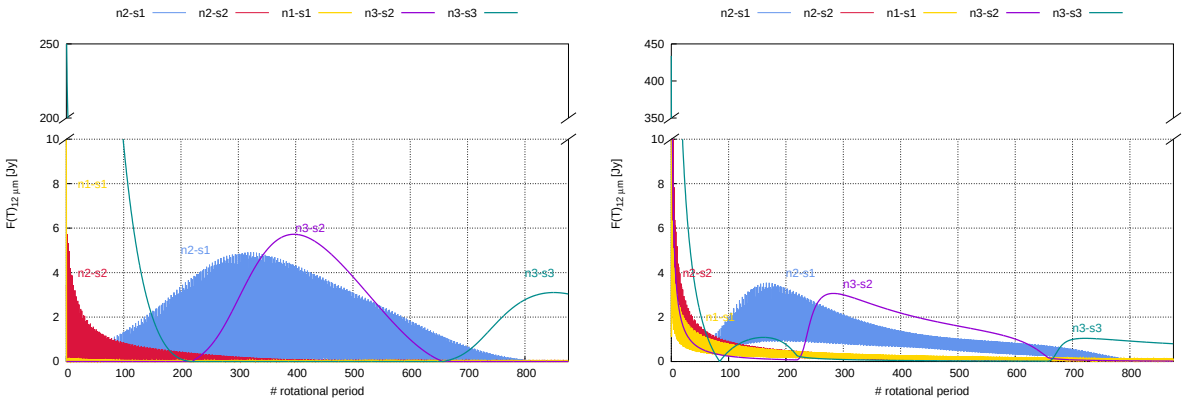

(a) Basalt (b) Regolith

Figure 2.8: Projected single facet flux error caused by temperature relaxation error between the first and third orbital periods for basalt and regolith materials (see Tab. 2.1). The order of the reference flux is $\sim$ 200-$\sim$ 500 Jy.

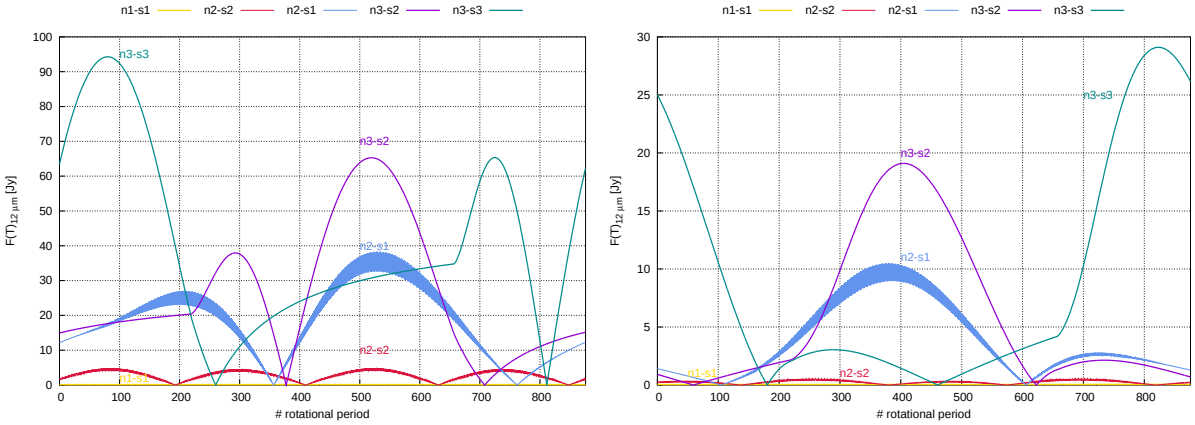

(a) Basalt, error for integration depth 1.5 m (b) Basalt, error for integration depth 5.0 m

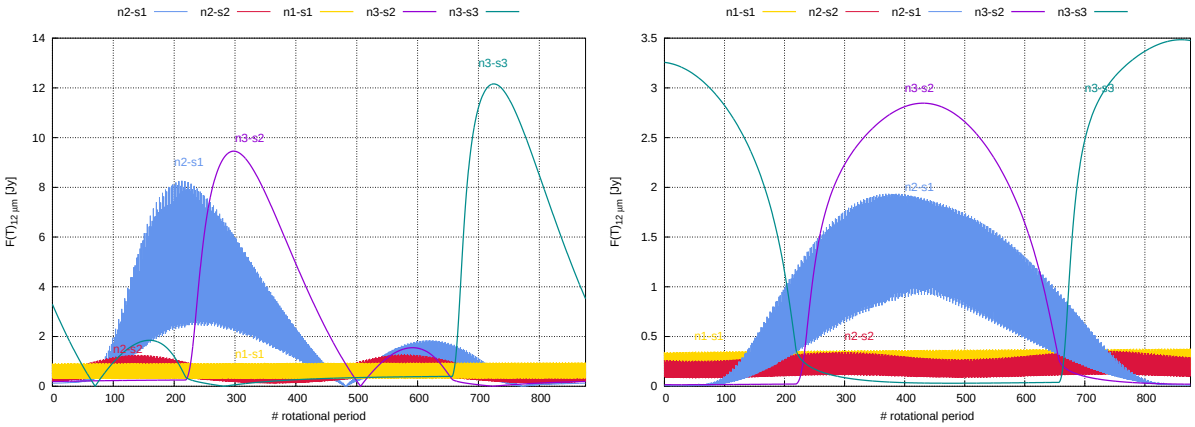

(c) Regolith, error for integration depth 0.5 m (d) Regolith, error for integration depth 1.0 m

Figure 2.9: Projected single facet flux error caused by integration depth error for basalt and regolith materials (see Tab. 2.1). The order of the reference flux is $\sim$ 200-$\sim$ 500 Jy.

n3 in orbital configuration s2, the large temperature error is propagated into the flux. Therefore, we cannot confirm the hypothesis that the facets with large temperature error do not contribute significantly to the total flux.

Chapter 3

Uniqueness, stability, and convergence of the extended inversion method

Traditionally a well-posed problem is characterized with three conditions: *existence*, *stability* and *uniqueness* of the solution. We approach the problem from experimental side and summarize results of the numerical tests we conducted.

3.1 Introduction

Existence As we can find a good model of an asteroid that describes the observed (in the next chapter we present models of several asteroids) data, we immediately confirm the existence of the solution.

Uniqueness In general, the problem of light curve inversion is not unique as shown in Kaasalainen et al. (1992), however, under certain assumptions, the solution to the light curve inversion is unique. These assumptions require that we have sufficiently good data — the light curve observations have to be extensive (i.e. have to cover sufficiently long periods and observation angles) and should not be encumbered with large errors. We also have to assume convex shapes. Furthermore, for uniqueness, precise knowledge of geometry (rotation period, orientation of the asteroid's axis with respect to the ecliptic), scattering law and its parameters have to be known.

Second, Kaasalainen and Torppa (2001); Kaasalainen et al. (2001) showed that once we start adding additional parameters to the parameter space such as period, axis orientation etc., the uniqueness is lost. Yet, we still have local uniqueness in the sense that there are several local minima of the function χ^2 defined by Eq. (1.1) and in the case of TPM by Eq. (1.4). Which local minimum we reach, however, depends on the initial choice of the parameters. Consequently, as our extended inversion method adds additional parameters to the parameter space, we conclude that there is no global minimum that would guarantee the uniqueness. Yet, we can still have local minima and if we start in the correct "valley", we will eventually reach the model that best explains the observations.

Non-uniqueness Next, the fact whether the model describes the actual asteroid is a different question, i.e. even if we were guaranteed a unique solution that exists, there is no guarantee that it describes the actual asteroid. The reason for this is the fact that the observation data are plagued with errors and random noise. Therefore,

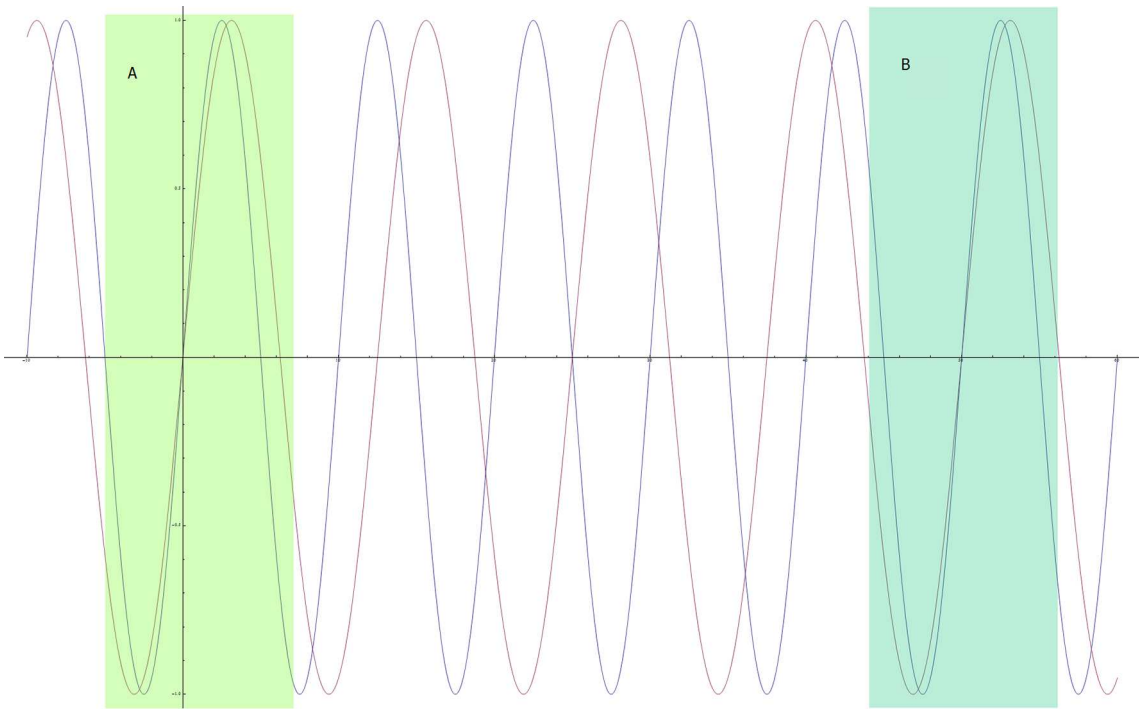

Figure 3.1: Illustration of how maxima may almost re-synchronize after some time T. Consequently, there if we have the two periods that explain the observed data. This is for illustration purposes, in reality, there would be a lot of periods between the ranges A and B.

the better the observation data, the higher chance that our model describes an actual asteroid. Having said that, it is necessary to mention that the quality of the observation data (their accuracy) have important effect on our model. It determines the accuracy of determined parameters; in the language of the minimization method, inaccurate data make the valley, where we search for local minimum, shallow.

Local uniqueness The choice of the "correct" valley is essential. The usual method is to go walk across many neighbouring valleys and compare their depths, i.e. χ^2 reached in each of them. The efficiency on this journey is determined primarily by the width of the valleys. From this angle, the initial guess of the period is especially important. Kaasalainen et al. (2001) showed that if P is the guessed period, than the smallest separation of the local minima of χ^2 are ΔP apart such that:

$$\frac{\Delta P}{P} \approx \frac{1}{2}\frac{P}{T}, \tag{3.1}$$

where $T = \max(|t - t_0|)$ is the longest observation range for light curves. To understand, we have to realize that it is not unusual to have light curves measured long time T apart at t_0 and then at $t = t_0 + T$. We then fit the measure data with a curve and this determines the period. However, if we change the period P by a particular amount ΔP, we will see that the period $P + \Delta P$ fits the data at t_0 and t too. This is illustrated in Fig. 3.1. We have light curve measurements in the green range A and, some time later, measurements in the cyan range B. In between, we have no measurement data. We can see that if P is changed by a particular ΔP, the sine functions in A and B are very similar. And because we fit discrete data with errors, both periods P and $P + \Delta P$ may describe well enough the observed light curves.

As far as the rotational axis orientation is concerned, it is usually sufficient to choose a few orientations in each octant. We then apply the inverse problem to each choice and the one with the smallest χ^2 sum is the one that best explains the observation data Kaasalainen et al. (2001).

Stability We can consider the stability from two angles. First, the stability with respect to observation data. In this regard we consider the method stable if small perturbations in observation data result only in small change in the final parameters of the asteroid (shape, size, axis orientation, period, thermal inertia). This stability, especially with respect to the resulting shape, has been studied by Kaasalainen and Torppa (2001).

We can also consider stability as such property, that if we change some input parameters (e.g. the scattering Hapke parameters) by a small amount, we get a similar physical model of the asteroid characterized by both the physical properties and its shape.

3.2 Testing the TPM

In order to determine the overall feasibility of the extended inversion method, we conducted several test. We start with the assumption that we already know some value of the period in the correct valley. We also know some values of ecliptic longitude and latitude also in their respective correct valleys. These parameters can be determined by the standard light curve inversion method.

In order to evaluate the extended version, we should aim our tests at the thermal inertia parameter which is not part of the standard problem. However, as the flux from the asteroid surface is modified by surface roughness (parameters cratering coverage and crater aperture in Tab. 1.1), we also have to take in to account the relation between the thermal inertia and surface roughness.

3.2.1 Fitting thermal inertia

Our task now is to determine thermal inertia from observation data, we aim to find a best fit and determine accuracy of the found value. We propose the following test to check whether the TPM is stable with respect to the thermal inertia Γ. We fix Hapke parameters which we get from the standard light curve inversion. Then we solve the inverse problem for a given surface roughness for several values of thermal inertia. We then plot the thermal inertia against the χ^2 returned by the TPM solver for each of the surface roughnesses. We expect to see that for each surface roughness the χ^2 reaches minimum at slightly different values of thermal inertia, however, the minima should be close apart. This then gives a possible range of thermal inertias. The plot will also yield information about the most probable parameters that specify the surface roughness (Delbo' and Tanga, 2009).

Testing methodology We use TPM with the current implementation, i.e. without the changes proposed in the previous chapter. We use observation data for asteroids 21 Lutetia, 32 Pomona and 306 Unitas, the only parameters in the parameter space (i.e. those that we allow to be optimized) are ecliptic longitude and latitude (λ, β), period and shape. The values of input parameters are in Tab. 3.1. We use parameters crater coverage (CC) and crater aperture (CA) to specify the surface roughness. For each pair of these parameters, we run the TPM solver with several thermal inertia values.

Table 3.1: Fixed parameters for thermal inertia testing. See Tab. 1.1 for their interpretation. Angles are in degrees and period in hours.

Asteroid	λ	β	period	ω	h	S_0	g	$\bar{\theta}$	η
21 Lutetia	52	−6	8.168270	0.2	0.02	0.4	−0.3	−30	0.9
32 Pomona	267	58	9.44767	0.1	0.06	0.4	−0.3	−20	0.9
306 Unitas	79	−35	8.73875	0.324	0.06	0.866	−0.183	−20	0.9

Test results We present the plots of thermal inertia Γ against χ^2 in Fig. 3.1. We can see a significant difference from our expectations. For most of the surface roughness configurations, the χ^2 approaches the smallest value as $\Gamma \to 0$. The reason behind this unfortunate behaviour is, yet, unknown, nevertheless we offer the following explanation. The cratering (surface roughness) implemented in the TPM solver modifies infrared flux from each facet that is calculated from the Planck law (see Eq. (1.2)). In effect the higher the surface roughness, the more skewed the original flux is. This in effect may hide various errors in the surface temperature as described in the previous chapter. On the other hand, as we decrease the roughness, the temperature errors may be more visible in the total flux. Specifically, the insufficient integration depth together with Neumann boundary condition cause similar temperature behaviour as if the thermal inertia was very small. This can also be seen from the simplified 1D analytical solution in App. C.

In the case of the asteroid 306 Unitas in Fig. 3.2c, we observe that a very good fit of data is provided when the cratering coverage $CC = 80\%$ and aperture $CA = 70°$. This results in a thermal inertia $\Gamma \sim 100\,\mathrm{J \cdot m^{-2} \cdot K^{-1} \cdot s^{-1/2}}$ which is comparable with the results obtained by Marco Delbo using a different approach (Delbo' and Tanga, 2009). For all asteroids we observed a very good fit of the light curve data. In the case of asteroids 306 Unitas and 32 Pomona, we also obtained in all test a very good fit of the IR data. For asteroid 21 Lutetia we observed that the fit of IR data was worse.

Another way to interpret the obtained data for the asteroids is that the "valley" where we look for the minimum is too shallow. In other words, the observed data can be equally well interpreted by several models:

1. Models with low to medium surface roughness can have thermal inertia from almost zero to $\approx 100\,\mathrm{J \cdot m^{-2} \cdot K^{-1} \cdot s^{-1/2}}$.

2. Model with high surface roughness; then thermal inertia can be anything between $\approx 1\,\mathrm{J \cdot m^{-2} \cdot K^{-1} \cdot s^{-1/2}}$ and $\approx 1000\,\mathrm{J \cdot m^{-2} \cdot K^{-1} \cdot s^{-1/2}}$.

This interpretation suggests that either, the HCE is solved with insufficient accuracy or that the application of surface roughness generates noise that prevents us from reasonably limiting possible values of thermal inertia.

3.2.2 Thermal inertia convergence

In the next test, we let the TPM solver freely adjust the thermal inertia. Based on the results in the previous paragraph, we expected that thermal inertia should converge to very low values for small to medium surface roughness and keep above $\approx 50\,\mathrm{J \cdot m^{-2} \cdot K^{-1} \cdot s^{-1/2}}$ for high surface roughness.

Testing methodology we varied the cratering parameters and watched the thermal inertia adjust. Other parameters but those mentioned in previous test were kept fixed.

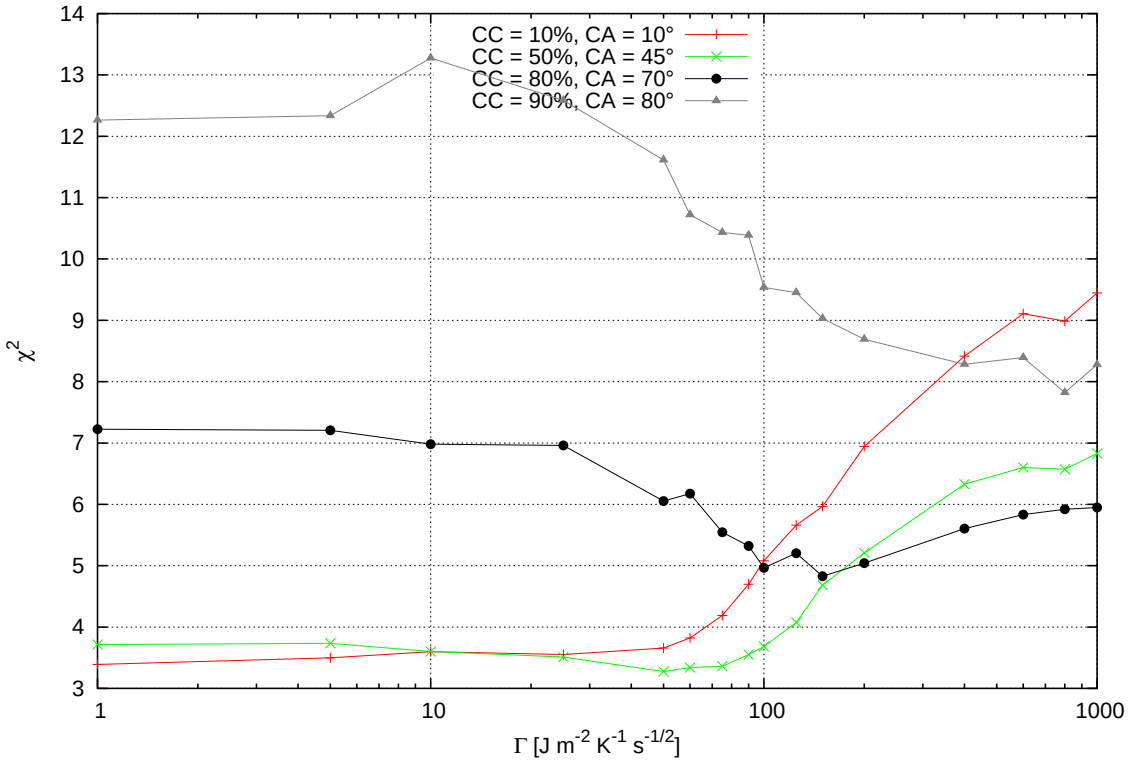

(a) 21 Lutetia

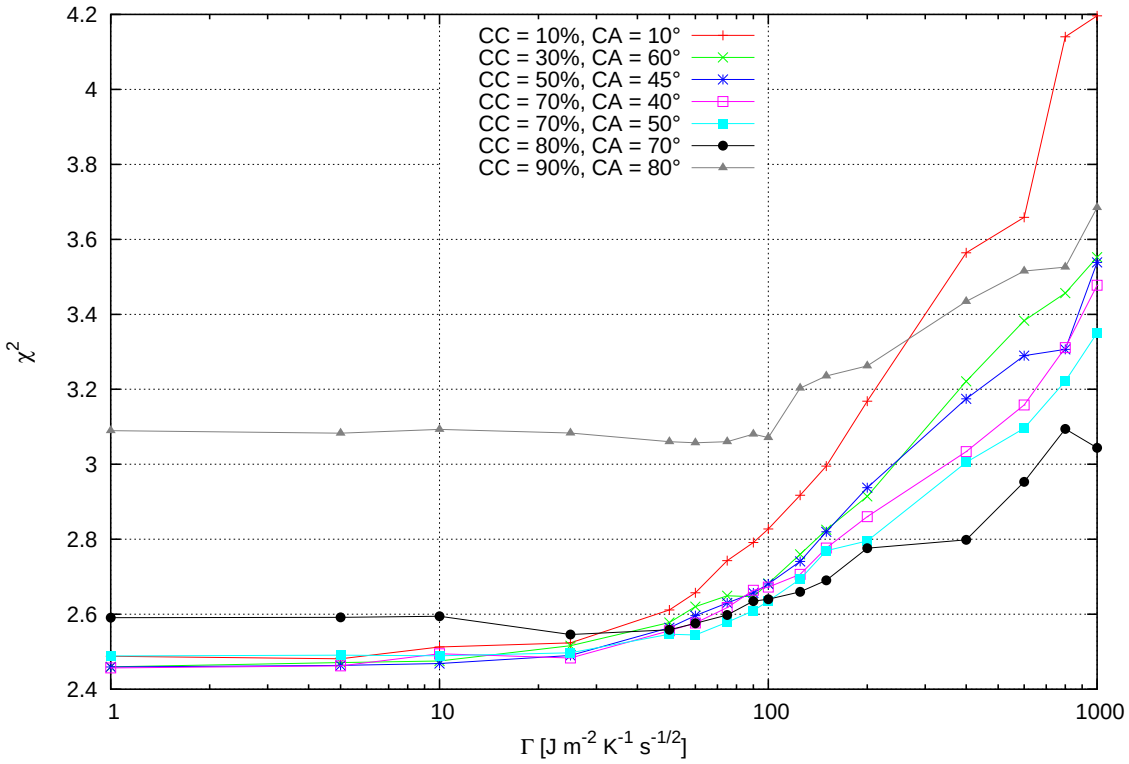

(b) 32 Pomona

Figure 3.2: χ^2 for various thermal inertia values (Γ) and surface roughnesses. (CC specifies crater coverage in per cent, CA the crater aperture in degrees).

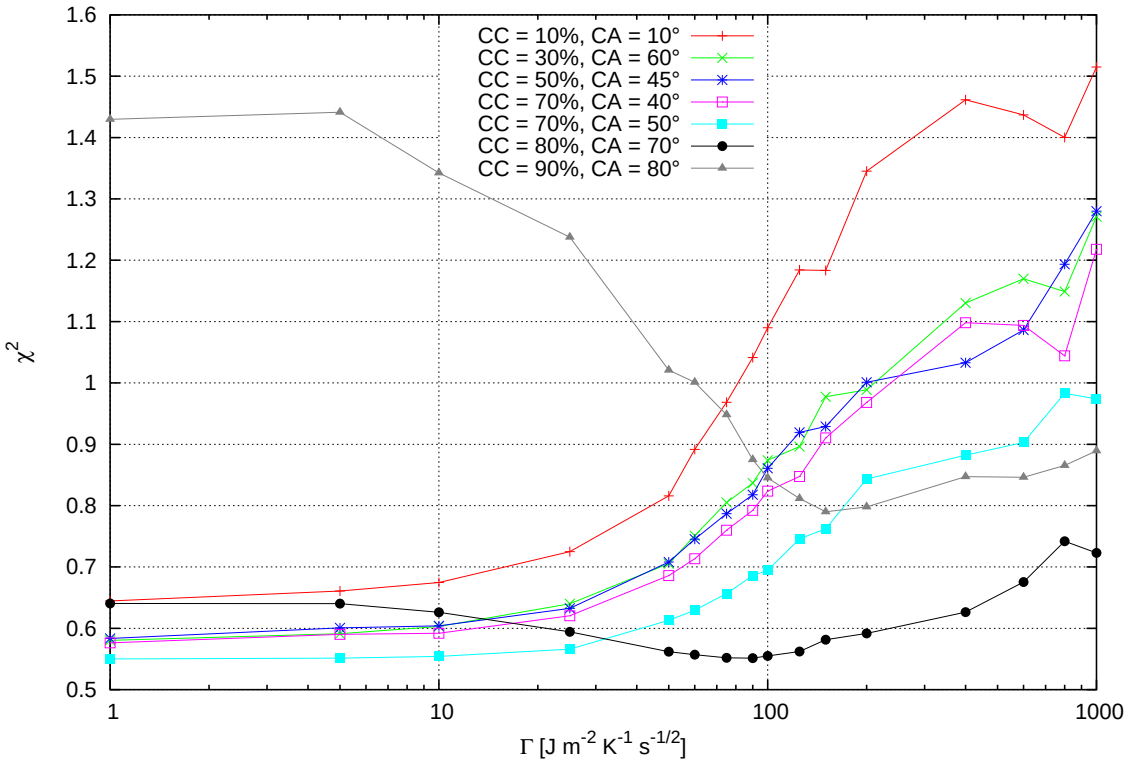

(c) 306 Unitas

Figure 3.1: χ^2 for various thermal inertia values (Γ) and surface roughnesses. (CC specifies crater coverage in per cent, CA the crater aperture in degrees).

We tested 4 initial settings of thermal inertial: 10, 50, 100 and 200 $\mathrm{J \cdot m^{-2} \cdot K^{-1} \cdot s^{-1/2}}$. We conducted the tests only with the data for the asteroid 306 Unitas.

Test results We display the results of the test in Fig. 3.2. The first panel shows the converged values of thermal inertia for various surface roughness parameters and initial settings of the inertia (depicted with the same colour). The second panel shows the converged values compared to the values of χ^2 obtained in the previous test. We notice that, as the thermal inertia parameter is freed, it converges to the lowest value of χ^2, determined in the previous test for the appropriate roughness, regardless of its initial settings. This shows the convergence of the model.

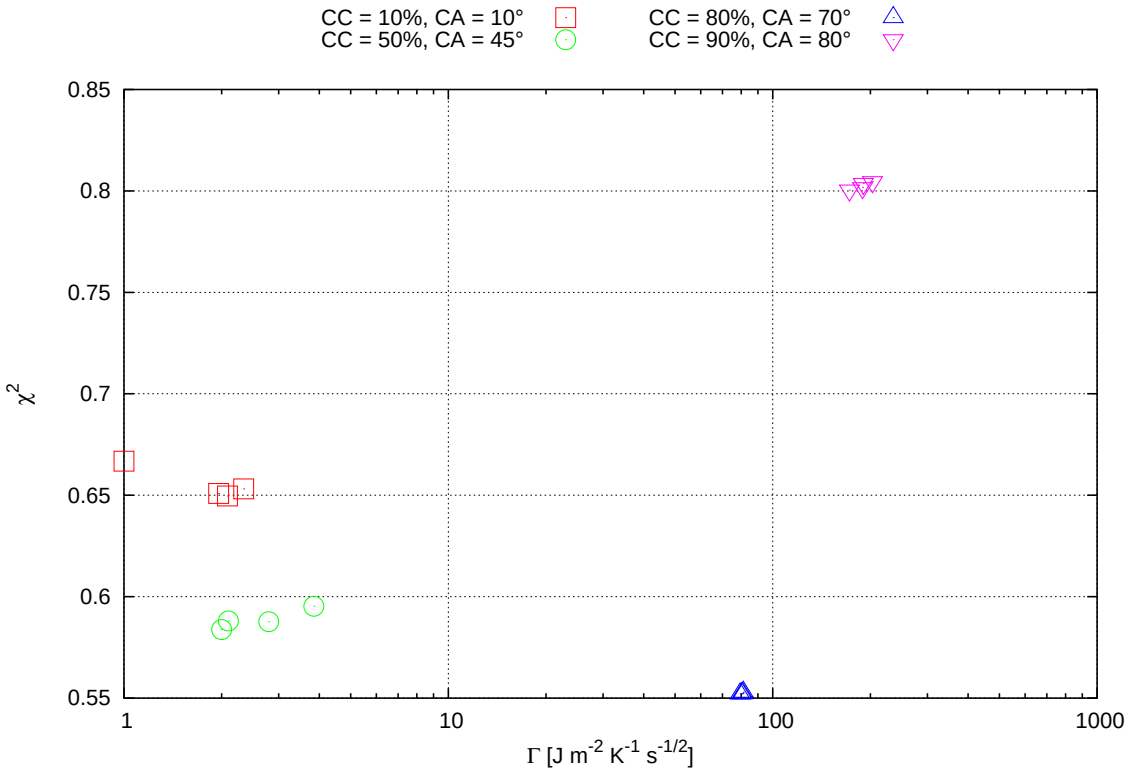

(a) Converged values of thermal inertia Γ.

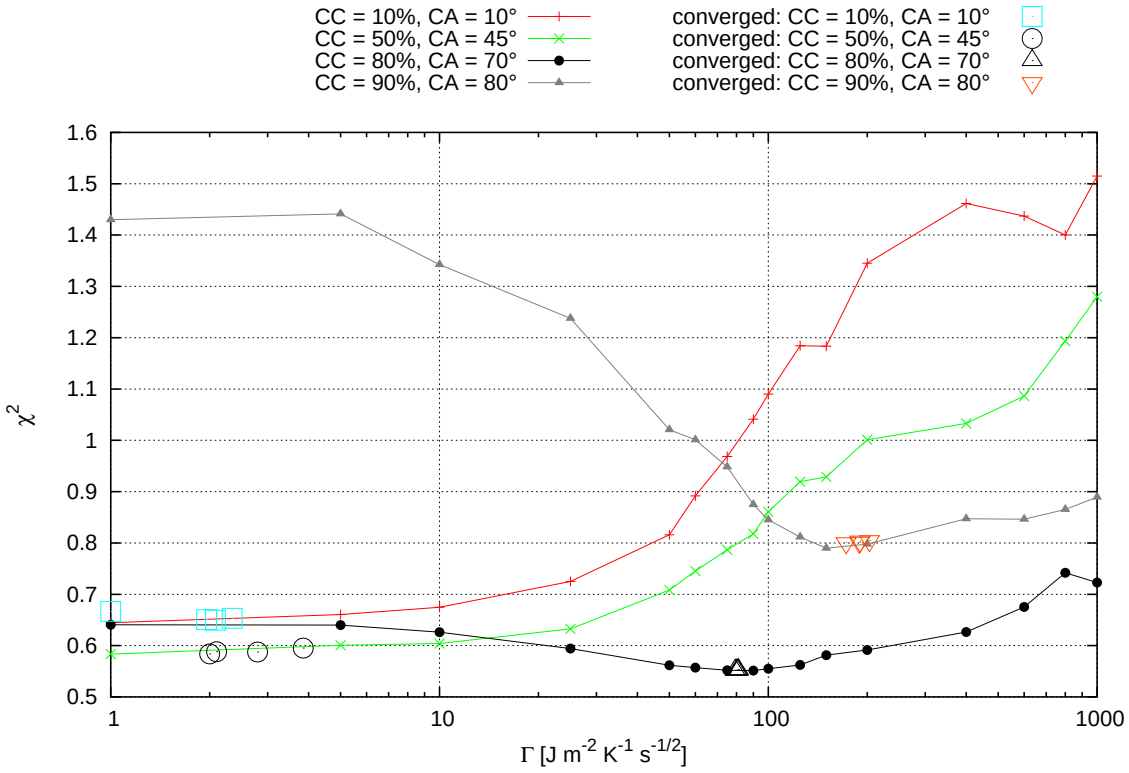

(b) Converged values of thermal inertia and compared to the χ^2 values when inertia was fixed.

Figure 3.2: χ^2 and optimized thermal inertia values (Γ) for various types of surface roughness of the asteroid 306 Unitas. (CC specifies crater coverage in per cent, CA the crater aperture in degrees).

Chapter 4

Models of selected asteroids

In this chapter we employ the full process of asteroid modelling. We solve the extended inverse problem. From the data, we reconstruct the shape (solve the Minkowski problem) and finally use visualisation package Meshlab to display the asteroid's shape. We then compare the shapes derived for various values of surface roughness. This chapter is divided into three sections, each devoted to one asteroid.

4.1 306 Unitas

Shape generation methodology We used the input parameters in Tab. 4.1 to generate the shape of Unitas. We generated shapes for three different surface roughness configurations. The parameters that TPM optimized were the orientation of the rotation axis, period and thermal inertia. Remaining parameters were fixed.

Resulting shapes and parameters

Parameters Tab. 4.2 summarizes the modeled physical properties of the asteroid for various surface roughness configurations and the associated χ^2 of the fit. We also show parameters reduced χ^2_{IR} which describes how well the IR data were fitted (the smaller the value, the better the fit; also the fit is good if $\chi^2_{\mathrm{IR}} < 1$) and the parameter which we designate Δ_{LC} which describes the quality of the light curve fit (the smaller, th better).

We have discussed the relation between thermal inertia and the value of χ^2 in the previous chapter. Here, we make further observations.

The optimization method does not change period significantly, however, as we discussed at the beginning of Chap. 3, period is the parameter that we have to know very precisely unless we want to end in a different local minimum of the χ^2.

Another feature that we came across in all other tests and that is apparent in Tab. 4.2 is that the changes in ecliptic latitude β are more pronounced compared to the longitude λ.

Last, we observe that the resulting diameter of the asteroid is quite independent of the cratering parameter.

Shapes We present the shapes that result from the TPM solver in Fig. 4.1 where each row represents one shape as viewed from three orthogonal directions. The gray and magenta shapes, although different, share similar features. On the other hand, the dark-cyan shape is noticeably different, especially in the first two left viewpoints.

Table 4.1: Parameters used to generate the shape of 306 Unitas. The parameters denoted with * were optimized by the TPM solver and the values represent their initial guess. See Tab. 1.1 for their interpretation. D is the initial guess for diameter that a sphere with the same surface as the initial shape. The units of the parameters are in SI, except for the period which is in hours and diameter in kilometres.

λ^*	β^*	period*	D^*	Γ^*	ω	h	S_0	g	$\bar{\theta}$	η
79°	−35°	8.73875 hr	50 km	100	0.324	0.06	0.866	−0.183	−20	0.9

Table 4.2: Physical properties associated with various models of surface roughness for the asteroid 306 Unitas. See Tab. 1.1 for their interpretation, CC represents the cratering coverage parameter and CA represents the crater aperture parameter.

CC	CA	λ	β	period	D	Γ	χ^2	χ^2_{IR}	Δ_{LC}
10%	10°	80.6°	−38.8°	8.738743	48 km	2	0.651	0.832	0.0231
80%	70°	81.5°	−37.2°	8.738743	50 km	81	0.553	0.560	0.0218
90%	80°	84.1°	−43.2°	8.738738	52 km	190	0.804	0.703	0.0265

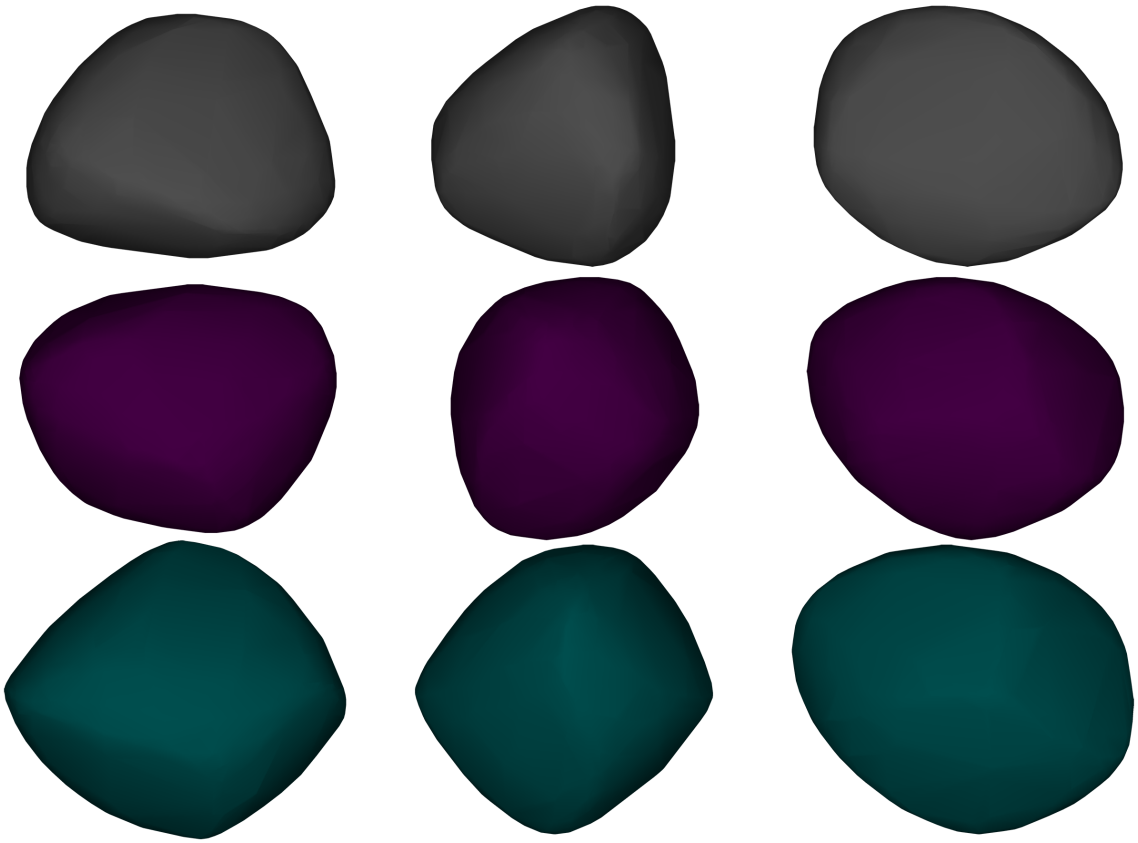

Figure 4.1: Three models of the asteroid 306 Unitas obtained by various surface roughness parameters: grey model is obtained from data with $CC = 10\%$, $CA = 10°$, magenta model is obtained from data with $CC = 80\%$, $CA = 70°$ and cyan from $CC = 90\%$, $CA = 80°$ (CC specifies crater coverage in per cent, CA the crater aperture in degrees). The columns represent views from three perpendicular directions. The spin axis of the asteroid is oriented: North-South in the left view, East-West in the middle view and to the page in the right view.

4.2 21 Lutetia

Shape generation methodology The shapes were generated in the very same manner as in the case of 306 Unitas. The model parameters and initial guesses can be found in Tab. 4.3.

Resulting shapes and parameters

Parameters Physical properties of 21 Lutetia are summarized in Tab. 4.4 for various surface roughness configurations. We confirm the observation made when we were discussing 306 Unitas; the ecliptic latitude β occupies larger range of values as we change the surface roughness and thermal inertia compared to the ecliptic longitude λ. Unlike in the case of Unitas, the thermal data fit is rather poor. However, light curve fit is very good. We also observe huge thermal inertia in the configuration with $CC = 90\%$. But we should not be concerned with this as the thermal data fit is too bad.

We also notice that the spherical equivalent diameter does not fit with the data obtained from the Rosetta space probe: the spherical equivalent diameter of 21 Lutetia based on data from the probe is (98 ± 3) km (Pätzold et al., 2011).

Shapes We present the shapes that result from the TPM solver in Fig. 4.2 where each row represents one shape as viewed from three orthogonal directions. We can clearly see that the magenta and dark-cyan shapes differ only in size, otherwise the are similar. The gray shape based on data from model with low surface roughness ($CC = 10\%$, $CA = 10°$) is visibly elongated in the first view.

Table 4.3: Parameters used to generate the shape of 21 Lutetia. The parameters denoted with * were optimized by the TPM solver and the values represent their initial guess. See Tab. 1.1 for their interpretation. D is the initial guess for diameter that a sphere with the same surface as the initial shape. The units of the parameters are in SI, except for the period which is in hours and diameter in kilometres.

λ^*	β^*	period*	D^*	Γ^*	ω	h	S_0	g	$\bar{\theta}$	η
52°	−6°	8.168270 hr	100 km	100	0.2	0.02	0.4	−0.3	−30	0.9

Table 4.4: Physical properties associated with various models of surface roughness for the asteroid 21 Lutetia. See Tab. 1.1 for their interpretation, CC represents the cratering coverage parameter and CA represents the crater aperture parameter.

CC	CA	λ	β	period	D	Γ	χ^2	χ^2_{IR}	Δ_{LC}
10%	10°	58.4°	−9.0°	8.168267	115.7 km	22.5	3.551	2.46	0.0260
80%	70°	55.8°	−16.0°	8.168268	115.6 km	181.0	5.285	7.51	0.028
90%	80°	57.3°	−26.6°	8.168268	120.0 km	1167.0	8.331	16.7	0.031

4.3 32 Pomona

Shape generation methodology The shapes were generated in the way as for the previous asteroids. The initial parameters are summarized in Tab. 4.5.

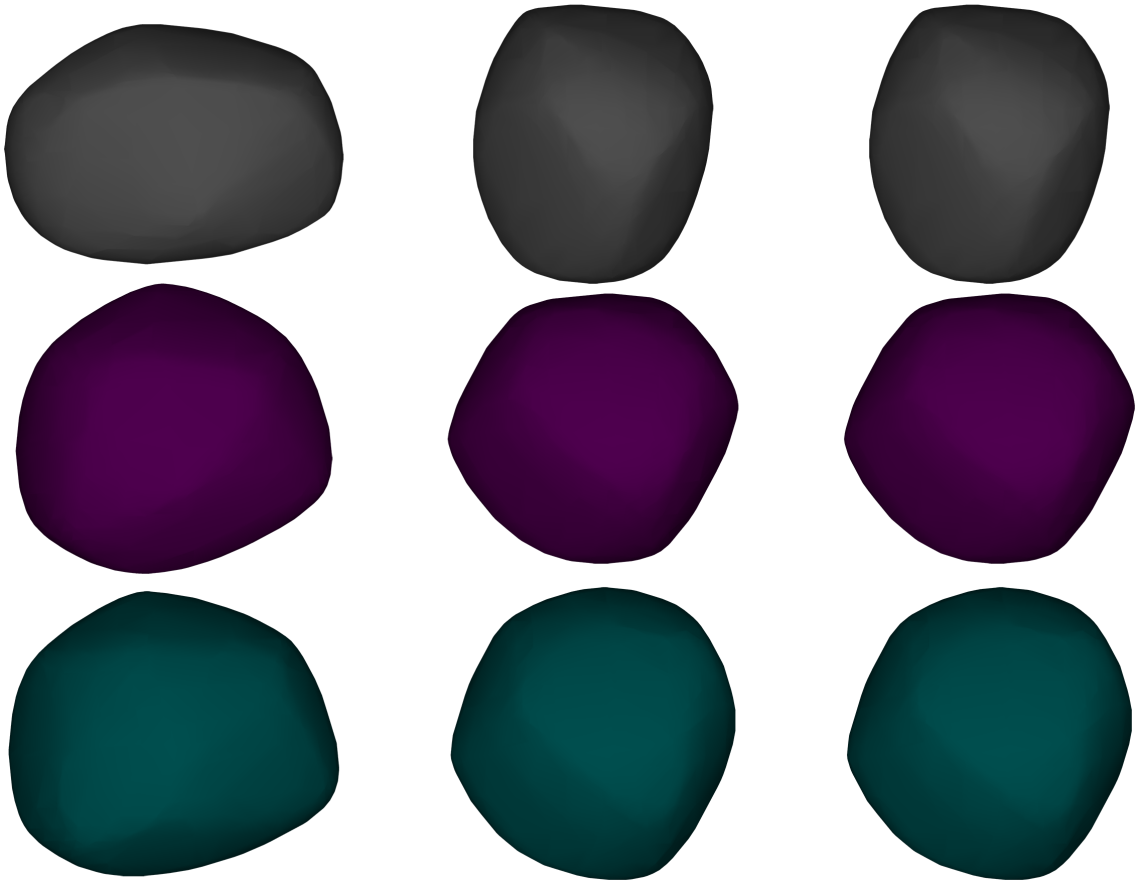

Figure 4.2: Three models of asteroid 21 Lutetia obtained by various surface roughness parameters: grey model is obtained from data with $CC = 10\%$, $CA = 10°$, magenta model is obtained from data with $CC = 80\%$, $CA = 70°$ and cyan from $CC = 90\%$, $CA = 80°$ (CC specifies crater coverage in per cent, CA the crater aperture in degrees). The columns represent views from three perpendicular directions. The spin axis of the asteroid is oriented: North-South in the left view, East-West in the middle view and to the page in the right view.

Resulting shapes and parameters

Parameters In Tab. 4.6 we see similar results as for 306 Unitas — both LC and IR data are very well fitted by all models. We also notice that for the low roughness configuration, the spherically equivalent diameter of the asteroid is noticeably different from the configuration with $CC = 80\%$ while at the same time the χ^2 is similar.

Shapes We present the shape of 32 Pomona in Fig. 4.3. Shapes for all three configurations are very similar. The configuration with $CC = 90\%$ (dark-cyan) results in shape somewhat more elongated in the middle viewpoint, otherwise, we do not notice any substantial differences other than the size.

Table 4.5: Parameters used to generate the shape of 32 Pomona. The parameters denoted with * were optimized by the TPM solver and the values represent their initial guess. See Tab. 1.1 for their interpretation. D is the initial guess for diameter that a sphere with the same surface as the initial shape. The units of the parameters are in SI, except for the period which is in hours and diameter in kilometres.

λ^*	β^*	period*	D^*	Γ^*	ω	h	S_0	g	$\bar{\theta}$	η
267°	58°	9.44767 hr	80 km	100	0.1	0.06	0.4	−0.3	−20	0.9

Table 4.6: Physical properties associated with various models of surface roughness for the asteroid 32 Pomona. See Tab. 1.1 for their interpretation, CC represents the cratering coverage parameter and CA represents the crater aperture parameter.

CC	CA	λ	β	period	D	Γ	χ^2	χ^2_{IR}	Δ_{LC}
10%	10°	273.0°	59.4°	9.447666	89.3 km	3.98	2.476	0.457	0.0365
80%	70°	273.9°	55.2°	9.447662	82.1 km	40.9	2.561	0.334	0.0372
90%	80°	274.7°	52.5°	9.447662	79.9 km	62.0	3.065	0.502	0.0407

4.4 Conclusion

We have generated shapes of selected asteroids and determined their physical parameters. While, the results from this and previous chapters show that parameters λ, β, period, spherical equivalent diameter are stable with respect to changes in thermal inertia and surface roughness, we have noticed that shapes of the asteroids are visibly different. Although the visual measure of difference is subjective, we had expected more similar shapes given the stability of other parameters.

We leave the question whether the thermal inertia is stable with respect to other parameters open. The main reason is the large uncertainty in its values determined by the TPM solver along with the zero-convergence behaviour. Once the accuracy issues from Chap. 2 will have been addressed, this issue should be revisited.

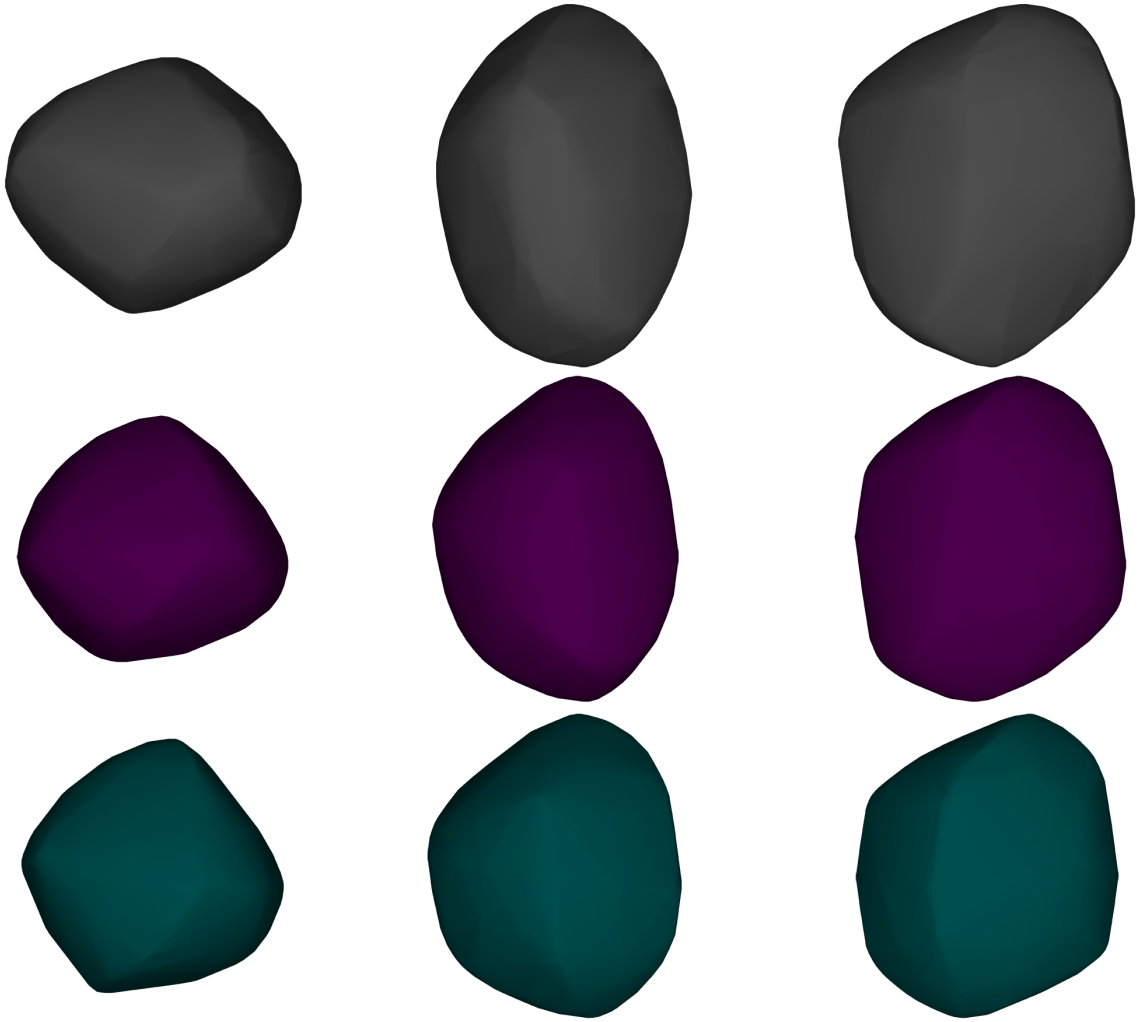

Figure 4.3: Three models of asteroid 32 Pomona obtained by various surface roughness parameters: grey model is obtained from data with $CC = 10\%$, $CA = 10°$, magenta model is obtained from data with $CC = 80\%$, $CA = 70°$ and cyan from $CC = 90\%$, $CA = 80°$ (CC specifies crater coverage in per cent, CA the crater aperture in degrees). The columns represent views from three perpendicular directions. The spin axis of the asteroid is oriented: North-South in the left view, East-West in the middle view and to the page in the right view.

Epilogue

Asteroids provide the most accessible information about the early evolution of the Solar System. Compared to the material that made up the planets, they survived almost intact since the planet formation stage and so they carry valuable information about our past. Yet, some basic physical properties of these objects are still unknown.

Thanks to light curve inversion, we have a tool that can not only model the shape of asteroids but also determine basic physical parameters. This standard technique has been extended with observations in the infrared spectrum with the aim of determining further parameters, namely thermal inertia and characteristics of surface roughness.

This extended light curve inversion rests strongly on the ability to accurately determine surface temperature distribution on the asteroid. In this work, we concern ourselves with issues that arise in the numerical solution of the Heat Conduction Equation. After a brief introduction and discussion of the applicability of one dimensional approximation, we provide results of extensive numerical testing. We identified following major sources of error in the determination of the surface temperature by a one dimensional numerical solver: insufficient relaxation of the solution, "incorrect" initial condition, small integration depth and insufficiently dense discrete grid.

Having identified the source of the errors and their magnitude, we estimated the maximum temperature errors allowed in order to achieve certain accuracy in the infrared flux from an asteroid. For observational errors $\sim$ 10%-$\sim$ 30%, which are typical for data from the IRAS satellite, we should aim at $\sim$ 1%-$\sim$ 5% temperature errors. We also provided guidelines in order to address accuracy issues in the current implementation of the numerical solver of the extended light curve method.

In the final chapters of this work, we discussed uniqueness of the solution to the extended problem. We analyzed the behaviour of thermal inertia and its impact on the solution. We also showed that with the current implementation of the extended method, the uncertainty of thermal inertia is very high. We suggest that the question of stability of thermal inertia with respect to other parameters as well as the feasibility of determining its reasonable value be revisited once the numerical solution of the thermal problem is improved.

Bibliography

APL, J. H. U. (1997). Near fast approaching asteroid 253 mathilde.

Bertotti, B., Farinella, P., and Vokrouhlickỳ, D. (2003). *Physics of the Solar System: Dynamics and Evolution, Space Physics, and Spacetime Structure*. Astrophysics and space science library. Kluwer Academic Publishers.

Brož, M. and Šolc, M. (2013). *Fyzika slunecni soustavy*. Matfyzpress, vyd. 1. edition.

Delbo', M. and Tanga, P. (2009). Thermal inertia of main belt asteroids smaller than 100 km from IRAS data. Planet. Space Sci., 57:259–265.

Kaasalainen, M., Lamberg, L., Lumme, K., and Bowell, E. (1992). Interpretation of lightcurves of atmosphereless bodies. I - General theory and new inversion schemes. A&A, 259:318–332.

Kaasalainen, M. and Torppa, J. (2001). Optimization Methods for Asteroid Lightcurve Inversion. I. Shape Determination. Icarus, 153:24–36.

Kaasalainen, M., Torppa, J., and Muinonen, K. (2001). Optimization Methods for Asteroid Lightcurve Inversion. II. The Complete Inverse Problem. Icarus, 153:37–51.

Lagerros, J. S. V. (1998). Thermal physics of asteroids. IV. Thermal infrared beaming. A&A, 332:1123–1132.

Lamberg, L. and Kaasalainen, M. (2001). Numerical solution of the Minkowski problem. *Journal of Computational and Applied Mathematics*, 137:213–227.

Morbidelli, A., Chambers, J., Lunine, J. I., Petit, J. M., Robert, F., Valsecchi, G. B., and Cyr, K. E. (2000). Source regions and time scales for the delivery of water to Earth. *Meteoritics and Planetary Science*, 35:1309–1320.

Pätzold, M., Andert, T. P., Häusler, B., Tellmann, S., Anderson, J. D., Asmar, S. W., Barriot, J.-P., and Bird, M. K. (2011). (21) Lutetia - low mass, high density. In *EPSC-DPS Joint Meeting 2011*, page 1184.

Pohl, L. (2011). Heat diffusion equation in the physics of asteroids and meteoroids. Bachelor thesis, Charles University.

Press, W. H., Teukolsky, S. A., Vetterling, W. T., and Flannery, B. P. (1992). *Numerical Recipes in C (2Nd Ed.): The Art of Scientific Computing*. Cambridge University Press, New York, NY, USA.

Vokrouhlicky, D. (1998a). Diurnal Yarkovsky effect as a source of mobility of meter-sized asteroidal fragments. I. Linear theory. A&A, 335:1093–1100.

Vokrouhlicky, D. (1998b). Diurnal Yarkovsky effect as a source of mobility of meter-sized asteroidal fragments. II. Non-sphericity effects. A&A, 338:353–363.

List of Tables

List of Figures

List of Abbreviations

NASA	The National Aeronautics and Space Administration
JAXA	Japan Aerospace Exploration Agency
ESA	The European Space Agency
LSM	Least Squares Method
TPM	Thermo-Physical Modeling
L-M	Levenberg-Marquardt method
1D	one dimensional
HCE	Heat Conduction Equation
3D	three dimensional
IR	Infrared
LC	Light curve
FDM	Finite Difference Method
YORP	Yarkovsky–O'Keefe–Radzievskii–Paddack effect
C-N	Crank Nicholson implicit scheme
PDE	Partial Differential Equation
LAPACK	Linear Algebra Package
MKL	Math Kernel Library
IC	Initial Condition
BC	Boundary Condition
IC-BC	Initial and Boundary Conditions
IRAS	Infrared Astronomical Satellite
WISE	Wide-field Infrared Survey Explorer
CC	Crater Coverage
CA	Crater Aperture

Appendices

Appendix A

HCE with dimensionless space variable

We start with the standard 1D HCE:

$$\frac{\partial T}{\partial t}(t,x) = \frac{\alpha}{\rho c}\frac{\partial^2}{\partial x^2}T(t,x)\,,$$
$$\varepsilon_{\mathrm{S}}(t)(1-A) = \varepsilon\sigma T^4(t,x)\Big|_{\text{surface}} + \alpha\frac{\partial}{\partial x}T(t,x)\Big|_{\text{surface}}\,.$$

We define $\chi \equiv \frac{x}{l_{\mathrm{s}}}$. This leads to:

$$\rho c\frac{\partial T}{\partial t}(t,l_{\mathrm{s}}\chi) = \alpha\frac{\partial}{\partial x}\left(\frac{\partial}{\partial x}T(t,l_{\mathrm{s}}\chi)\right) = \alpha\frac{\partial}{\partial x}\left(\frac{\partial}{\partial x}\tilde{T}(t,\chi)\right) = \alpha\frac{\partial}{\partial x}\left(\frac{\partial\tilde{T}(t,\chi)}{\partial\chi}\overbrace{\frac{\mathrm{d}\chi}{\mathrm{d}x}}^{\frac{1}{l_{\mathrm{s}}}}\right)$$
$$= \frac{\alpha}{l_{\mathrm{s}}}\cdot\frac{\partial}{\partial x}\frac{\partial\tilde{T}(1,\chi)}{\partial\chi} = \frac{\alpha}{l_{\mathrm{s}}}\cdot\frac{\partial^2\tilde{T}(1,\chi)}{\partial\chi^2}\underbrace{\frac{\mathrm{d}\chi}{\mathrm{d}x}}_{\frac{1}{l_{\mathrm{s}}}} = \frac{\alpha}{l_{\mathrm{s}}^2}\cdot\frac{\partial^2\tilde{T}(t,\chi)}{\partial\chi^2}\,.$$

Similarly:

$$\alpha\frac{\partial}{\partial x}T(t,x)\Big|_{x=0} = \eta\sigma T^4(t,0) - (1-A)\cdot F_{\mathrm{S}}(t)\,,$$
$$\alpha\frac{\partial}{\partial x}T(t,l_{\mathrm{s}}\chi)\Big|_{x=0} = \alpha\frac{\partial}{\partial x}\tilde{T}(t,\chi)\Big|_{x=0\,\Longleftrightarrow\,\chi\equiv 0} = \alpha\left[\frac{\partial}{\partial\chi}\tilde{T}(t,\chi)\frac{\mathrm{d}\chi}{\mathrm{d}x}\right]\Big|_{\chi=0} = \frac{\alpha}{l_{\mathrm{s}}}\cdot\frac{\partial\tilde{T}(t,\chi)}{\partial\chi}\Big|_{\chi=0}\,.$$

Thus we have:

$$\rho c\frac{\partial\tilde{T}(t,\chi)}{\partial t} = \frac{\alpha}{l_{\mathrm{s}}^2}\cdot\frac{\partial^2\tilde{T}(t,\chi)}{\partial\chi^2}\,,$$
$$\frac{\alpha}{l_{\mathrm{s}}}\cdot\frac{\partial\tilde{T}(t,\chi)}{\partial\chi}\Big|_{\chi=0} = \eta\sigma T^4(t,0) - (1-A)\cdot F_{\mathrm{S}}(t)\,,$$

In the simplified one dimensional solution presented in App. C, we introduced the concept of *skin depth*. Therefore, if we represent l_{s} as the skin depth, then introduced dimensionless variable χ simply presents the space coordinate as a fraction of this skin depth. We can then use the following relation:

$$l_{\mathrm{s}} = \sqrt{\frac{\alpha}{\pi f\rho c}} = \sqrt{\frac{2\alpha}{\omega\rho c}}\,,$$

where ω is the angular frequency of rotation. We can substitute the fraction $\frac{\alpha}{l_\mathrm{s}}$:

$$\frac{\alpha}{l_\mathrm{s}} = \sqrt{\omega} \cdot \sqrt{\alpha \rho c} = \sqrt{\omega} \cdot \Gamma \,,$$

where we have identified the thermal inertia Γ and the fraction $\frac{\alpha}{l_\mathrm{s}^2}$ by:

$$\frac{\alpha}{l_\mathrm{s}^2} = \frac{\alpha}{\frac{2\alpha}{\omega \rho c}} = \frac{\omega}{2} \cdot \rho c \,.$$

Putting these into the HCE and the boundary condition and eliminating ρc leads to HCE with dimensionless space variable:

$$\frac{\partial \tilde{T}(t,\chi)}{\partial t} = \frac{\omega}{2} \cdot \frac{\partial^2 \tilde{T}(t,\chi)}{\partial \chi^2} \,,$$
$$\sqrt{\omega} \cdot \Gamma \cdot \left. \frac{\partial \tilde{T}(t,\chi)}{\partial \chi} \right|_{\chi=0} = \eta \sigma T^4(t,0) - (1-A) \cdot F_\mathrm{S}(t) \,.$$

The major advantage of this formulation for the TPM solver is that instead of having to optimize for three thermal parameters ρ, α, c, we now have only one parameter Γ. On the other hand, this reduction makes it impossible to reconstruct the standard parameters ρ, α and c, once we determine Γ. Another disadvantage is that this derivation is based on the one dimensional situation where the asteroid only rotates. This prevents interpreting the skin depth as the characteristic depth of penetration of temperature changes. Consequently, determination of the integration depth is difficult.

Appendix B

Crank-Nicholson with Neumann boundary condition

If we want to add Neumann boundary condition in the form $\frac{\partial T}{\partial x}|_{x=0} = 0$ in the center of the asteroid, we have to be a bit careful. Simple discretization of the gradient $\frac{u_1^n - u_0^n}{\Delta x}$ will introduce error of the order $\mathcal{O}(\Delta x)$ while the C-N method is of the order $\mathcal{O}(\Delta x^2)$. The trick we can do is make another point in the grid u_{-1}^n by linear extrapolation, so that we can use central difference and the boundary condition in the finite differences becomes (we omit the time index n):

$$\frac{u_1 - u_{-1}}{2\Delta x} = 0\,.$$

The central difference is of the order $\mathcal{O}(\Delta x^2)$ as $\Delta x \to 0$. This condition implies: $u_1^n = u_{-1}^n$ and also $u_1^{n+1} = u_{-1}^{n+1}$. The HCE converted to finite differences now looks:

$$\begin{aligned}
-b \cdot u_{-1}^{n+1} + (2+2b) \cdot u_0^{n+1} - b \cdot u_1^{n+1} &= b \cdot u_{-1}^n + (2-2b) \cdot u_0^n + b \cdot u_1^n\,,\\
-b \cdot u_0^{n+1} + (2+2b) \cdot u_1^{n+1} - b \cdot u_2^{n+1} &= b \cdot u_0^n + (2-2b) \cdot u_1^n + b \cdot u_2^n\,,\\
&\vdots\\
-b \cdot u_{J-2}^{n+1} + (2+2b) \cdot u_{J-1}^{n+1} - b \cdot u_J^{n+1} &= b \cdot u_{J-2}^n + (2-2b) \cdot u_{J-1}^n + b \cdot u_J^n\,.
\end{aligned}$$

Note, that this give a system with one more equation compared to the situation with the Dirichlet boundary condition. Employing the $u_1^n = u_{-1}^n$ and $u_1^{n+1} = u_{-1}^{n+1}$ and the fact that we the J grid point is determined by the Dirichlet boundary condition (the surface), we recast the above:

$$\begin{aligned}
(2+2b) \cdot u_0^{n+1} - 2b \cdot u_1^{n+1} &= (2-2b) \cdot u_0^n + 2b \cdot u_1^n\,,\\
-b \cdot u_0^{n+1} + (2+2b) \cdot u_1^{n+1} - b \cdot u_2^{n+1} &= b \cdot u_0^n + (2-2b) \cdot u_1^n + b \cdot u_2^n\,,\\
&\vdots\\
-b \cdot u_{J-2}^{n+1} + (2+2b) \cdot u_{J-1}^{n+1} &= b \cdot u_{J-2}^n + (2-2b) \cdot u_{J-1}^n + 2b \cdot u_J^n\,,
\end{aligned}$$

which can be recast in the matrix form of Eq. (2.16). Note that this matrix is no longer symmetrical compared to the case if we use internal Dirichlet boundary condition.

Appendix C

One dimensional analytical solution of the Heat Conduction Equation

Here we present an simplified analytical solution to the Heat Conduction Equation (HCE) in one dimension. This solution assumes a rotating asteroid without orbital motion, the spin axis of the asteroid perpendicular to the orbital plane and the solution is for a surface element on the equator. For full derivation of this solution see Pohl (2011). We assume isotropic and homogeneous material. Under this assumption, the HCE takes the following form in one dimension:

$$\partial_t T(t,x) - \frac{\alpha}{\rho c}\partial_{xx} T(t,x) = 0\,.$$

The energy conservation on the surface leads to the equation for the surface boundary condition:

$$\varepsilon_{\mathrm{S}}(t)(1-A) = \eta\sigma T^4(t,x)\Big|_{\mathrm{surf}} - \alpha\frac{\partial T}{\partial x}(t,x)\Big|_{\mathrm{surf}}\,.$$

The boundary condition inside the asteroid is assumed Dirichlet:

$$T(t,x)\Big|_{\mathrm{in}} = T_{\mathrm{eq}}\,,$$

and the initial condition is assumed:

$$T(0,x) = T_{\mathrm{eq}}\,,$$

We also assume that the temperature on the surface varies from T_{eq} only by a relatively small amount and that the asteroid in insolated by the following harmonic function:

$$\varepsilon_{\mathrm{S}}(t) = \varepsilon_{\mathrm{S0}} + \varepsilon_{\mathrm{SA}}\mathrm{e}^{\mathrm{i}\delta t}\,,$$

δ being angular frequency. Finally, we assume the resulting temperature distribution to be governed by:

$$T(t,x) = \chi(x)\mathrm{e}^{\mathrm{i}\delta t} + C\,,$$

where C is some constant.

Under these (and a few other minor) assumptions, we conclude that the solution the HCE is:

$$T(t,x) = \frac{\varepsilon_{\mathrm{SA}}(1-A)}{4\eta\sigma T_{\mathrm{eq}}^3}\,\frac{1}{\sqrt{1+2\Theta+2\Theta^2}}\,\exp\left[\mathrm{i}\cdot\left(2\pi f t+\varphi-\sqrt{\frac{\pi f\rho c}{\alpha}}x\right)\right]\cdot\exp\left(-\sqrt{\frac{\pi f\rho c}{\alpha}}x\right)+T_{\mathrm{eq}}\,,$$

$$T(t,0) = \frac{\varepsilon_{\mathrm{SA}}(1-A)}{4\eta\sigma T_{\mathrm{eq}}^3}\,\frac{1}{\sqrt{1+2\Theta+2\Theta^2}}\,\exp\left[\mathrm{i}\cdot(2\pi f t+\varphi)\right]+T_{\mathrm{eq}}\,,$$

$$\Theta = \frac{\sqrt{\pi f\alpha\rho c}}{4\eta\sigma T_{\mathrm{eq}}^3}\,,$$

$$\tan\varphi = -\frac{\Theta}{1+\Theta}\,.$$

The angle φ suggests a phase shift or lag between the temperature function $T(t,x)$ and the insolation function $\varepsilon_{\mathrm{S}}(t)$. We can identify thermal inertia in the Θ parameter, such that $\Theta \sim \sqrt{\omega}\,\Gamma$. And because the angle φ is a negative descending function of Θ ($\Theta \geq 0$) and $\Theta \in [0,\infty)$, we have $\varphi \in (-\frac{\pi}{2}, 0]$, i.e. we get a *bigger phase shift for materials with larger thermal inertia* (we need more heat to increase the temperature, i.e. more time to provide that heat to the asteroid). This is also the reason why for materials with higher thermal inertia, the numerical solution of HCE takes longer to relax.

we can also see that the temperature variations from T_{eq} are exponentially suppressed with depth; $(\frac{\pi f\rho c}{\alpha})^{\frac{1}{2}}$ is then an inverse of characteristic depth at which these variations are suppressed by a factor e^{-1}, i.e. at this depth the variations of temperature from T_{eq} are about a third of the variations on the surface.